STATISTICAL AND TEMPORAL ANALYSIS OF SHOCK-DRIVEN INSTABILITY THROUGH SIMULTANEOUS DENSITY AND VELOCITY MEASUREMENTS

A Dissertation
Presented to
The Academic Faculty

By

John Carter

In Partial Fulfillment
of the Requirements for the Degree
Doctor of Philosophy in the
School of Mechanical Engineering

Georgia Institute of Technology

August 2020

STATISTICAL AND TEMPORAL ANALYSIS OF SHOCK-DRIVEN INSTABILITY THROUGH SIMULTANEOUS DENSITY AND VELOCITY MEASUREMENTS

Approved by:

Professor Devesh Ranjan, Advisor
School of Mechanical Engineering
Georgia Institute of Technology

Professor Peter G Loutzenhiser
School of Mechanical Engineering
Georgia Institute of Technology

Professor Wenting Sun
School of Aerospace Engineering/
School of Mechanical Engineering
Georgia Institute of Technology

Dr. Robert A Gore
Los Alamos National Laboratory

Professor Joseph Oefelein
School of Aerospace Engineering
Georgia Institute of Technology

Professor Ellen Yi Chen Mazumdar
School of Mechanical Engineering
Georgia Institute of Technology

Date Approved: July 2020

”No aphorism can accurately express what I have observed”

-*Unknown*

To God, my friends, and family, without whom this would not have been possible.

ACKNOWLEDGEMENTS

God alone has made me successful. He has given me everything: all my creativity, knowledge, and wisdom, all the support, resources, and advice I have received have come from Him. Only with His strength have I persevered. I thank God for all the people he has given me throughout my graduate career, and I want to thank each one of those people, but words fail to express my gratitude. I would like to thank my committee for their time and support in mentoring me in this process. I can't express enough my thankfulness to my advisor, Professor Devesh Ranjan for accepting me into the lab, supporting, and guiding me along the way. I am thankful to have the opportunity to work on a project which aligned so well with my interests. I am also very grateful that he has let me see "behind the curtain" of academia. He has always pushed us and supported us in doing things that are good for our careers, both at Georgia Tech and in the future. Dr. Rob Gore has also given me much opportunity to see into the world of modeling, advice, and valuable discussion to my research.

I would like to express my deepest gratitude for Dr. Mohammad "Moh" Mohaghar. Working alongside him was incredibly redeeming of our time at Tech, and was one of the things I enjoyed most about our work. I appreciate all the work, and late nights he has put into this project. He deserves so much credit for what we have produced. More than that though, I have enjoyed our conversations and friendship. I am thankful for my ex-wife, who stuck with me for quite a bit of grad school, and was always supportive of this endeavor. There are so many who deserve to be acknowledged, but I will try to be brief. All of my labmates deserve thanks, but most of all Stephen Johnston, for always being willing to lend an ear or a hand (to anyone in the lab really), and most of all for being a great friend. It has been great being friends with Prasoon Oglethorpe Suchandra, one of the most considerate people I know, and with whom I have had many intellectual

conversations about our projects, which are similar. I have enjoyed drinking and making beer with American Sam, who has also been a good friend, and has lent an ear regarding life and research as well. I would like to thank Gokul, for conversations, advice, and his contributions to the high speed efforts. I also want to thank those I roomed with in Los Alamos: Wolfgang, Ben (also for your work on the first paper), and Mark were great to have around and made the experience much better. I value the time we had, our discussions about life and whatnot, hiking, and our friendships. There are so many people... I would like to thank David for teaching me a lot when I first started, and also for being a friend. Dr. Jacob, for designing the shock tube and leaving so much for us to start from. I am thankful for everyone in the lab, to have talked through some troubles, life, bikes, and OKRA (yelling). Everyone in the lab is always willing to discuss issues to help each other, something I appreciated greatly, and this collaborative culture has helped greatly in this work.

I am also thankful for many others for discussions of research of course, but also grad school, and life, who are at Tech or who I have met on internships, etc., and are probably unlikely to read this (and I wouldn't wish it upon them). I can't express enough my thankfulness to my parents for raising me (an understatement already), always being there to talk, and all their support. They deserve a lot of the credit for my success. I would also like to thank my girlfriend for so much support during the process of preparing my thesis and defense. Last, but only for emphasis, I would like to thank my entire family at Midtown Church for being welcoming, and continuing to Love and support me, helping me grow in Christ, and being the best family I can imagine. They have given me so much hope. Some of them know they have had a profound impact on me, but I don't even want to mention individuals, because I know all of our relationships will continue to grow, and I feel close to, and incredibly thankful for everyone there. I know the Love of Christ is in you.

This work was supported by the National Science Foundation Faculty Early Career Development (CAREER) Award (award no. 1451994), and Los Alamos National Lab Subcontract Number 524823.

TABLE OF CONTENTS

LIST OF TABLES

LIST OF FIGURES

SUMMARY

The effects of initial conditions (single- and multi-mode) and nondimensional density ratio (Atwood number, equivalently A or At) on dynamics of mixing in Richtmyer–Meshkov Instability evolution are studied using high resolution results from ensembles of experiments as well as temporally resolved measurements all utilizing simultaneous PLIF and PIV. Campaigns were undertaken at an incident shock Mach number of 1.55 on both single and multi-mode perturbed interfaces between two gas pairs before and after reshock. This was done to hold constant as many parameters as possible between the cases. The perturbations used were a single mode perturbation where the shock tube is inclined to 80°, resulting in a misalignment of 10° with the incident shock and a multi-mode perturbation where shear and bouyancy effecs result in additional features on the interface. The gas pairs used were N_2/CO_2 and N_2/SF_6, where the incident shock travels from light (N_2) to heavy gas. These gas pairs yield Atwood numbers of 0.22 and 0.67. This constitutes the first work where turbulence statistics resulting from ensemble averaging are collected on both of these Atwood numbers, and also the first comparison of Atwood numbers with otherwise parametric consistency where turbulence statistics from ensemble averaging can be compared. Furthermore, the high speed measurements in this flow are the first temporally resolved simultaneous PLIF and PIV measurements collected for RMI flows. This allows calculation of time-resolved quantities and time-correlated analysis of features from robust measurements.

RMI is studied through many quantities to analyze multiple facets of the resulting flow, and the effect of Atwood number and initial conditions on this flow are considered. The development of the flow and mixing are examined from several metrics. A qualitative analysis of flow development is presented from sequences of PLIF images to show the entire development of the instability. The growth of the mixing region is analyzed

via calculation of mixing width and mixing layer thickness. The proportion of entrained material which has mixed up to any time in the flow evolution is analyzed through mixedness. After nondimensionalization, the amplitude of the mixing region was observed to collapse, especially after reshock. However, these calculations still show a dependence on initial conditions which is modulated by the Atwood number, such that in the high Atwood number case before reshock, high interface growth rate yields a more stretched interface, less expression of features on the multi-mode interface, and less mixedness for both initial conditions. After reshock, a primary difference is demonstrated in higher prevalence of local inhomogeneities for the multi-mode high Atwood number case.

Through some of the largest ensembles of data collected, the turbulent state of the flow is analyzed via true turbulence statistics, and values are calculated such as the Density Self Correlation, including the field values of DSC only possible from ensemble averaging, turbulent mass flux velocity (a density velocity cross-statistic), and analysis of Reynolds stress and anisotropy. A morphological dependence is observed in statistics before reshock due to the bubble-spike asymmetry, and more active mixing is observed in the bubble region of the multimode case after reshock as demonstrated by the density self correlation, which shows higher values for the high Atwood number case at all times. The Boussinesq approximation is less valid for this descriptor of the mixing. The mass flux and Reynolds stress are higher in the high Atwood number case. While the Boussinesq approximation is more valid for the Reynolds stress, the selection of velocity fluctuations to density fluctuations is observed and connected to the small increase in the discrepancy between the Favre-averaged Reynolds stress and its first-term approximation. A high degree of anisotropy is observed in the high Atwood number case, correspnoding to delayed isotropization of the high momentum material. Despite the applicability of a scaling law based on self-similarity to the mixing width amplitude, these differences in flow physics are observed even at the same scaled, nondimensional times. This has

implications that other scaling laws for both temporal and spacial scales should be investigated, perhaps through large-ensemble high speed campaigns. The phenomena of transition and the role of Atwood number in transition are studied in relation to this flow via analysis of Reynolds number and energy spectra, along with evaluation of transition criteria. Transition is observed, and a broad range of scales are developed in both cases with $k^{-1.8}$ scaling.

Therefore, because the flow is unsteady, transitions to turbulence during the evolution, and the consequent role of fluctuating features and dynamics in the flow, it is desirable to understand the temporal development of the density and velocity fields in a time-correlated series from a single run. Thus, in addition to the high resolution evolution sequence of the interface from multiple runs and ensembles of runs at the same experimental times, a complementary study using high-speed PLIF and PIV provides the desired time-correlated results. In the high-speed study, the time-resolved evolution of relevant scales and mixing is captured, and shows very good comparison with high resolution PLIF results in this work, a result which is not realizable via high speed schlieren or Mie scattering diagnostics due to the volume-averaging and discrete, particle density-dependent nature of those diagnostics. Rather than snapshots of various features which are present at certain times in the evolution, and then snapshots of what they might become later (time-uncorrelated results) which prompts a statistical approach to their analysis, these experiments follow the evolution of the same specific interfacial features throughout the development of the RMI using advanced planar diagnostics.

Further, the deposition of vorticity by reshock and its subsequent evolution is analyzed. The vorticity deposited by reshock at each point along the interface is compared with the models of Samtaney, Ray, and Zabusky (SRZ98, [1]) and Weber, Cook, and Bonazza (WCB2013, [2]). Very good agreement is demonstrated with both models, with slightly better agreement for WCB2013. This is the first comparison of vorticity at each

point along the interface, while previous comparisons (which also achieved good agreement) have only compared with overall circulation.

This close agreement with experimental observations verifies these models for this flow. A dramatic result of modeling the distribution of vorticity, rather than the overall circulation is that it validates them in use for modeling vorticity deposition rather than computationally expensive shock-capturing methods. Subsequently, current simple time-stepping schemes can be used to model the evolution of vorticity from the post-shock state predicted by the models. Further, in cases where the Boussinesq approximation is valid, time integration can simply determine resulting concentration fields from initial conditions as well.

The current work captured mode-merging of two roll up features through observation of these features in both the concentration and vorticity fields. This result demonstrates utility in tracking features throughout their development as opposed to only considering the interface statistically. This further shows the dynamical interdependence of features in the species and velocity fields. The implementation of simultaneous PLIF and PIV and the subsequent analysis of this work are some of the first of this kind for high-speed turbulent mixing applications, and highlight the exciting possibilities that the recent advances in diagnostics enable.

CHAPTER 1

INTRODUCTION AND BACKGROUND

1.1 Overview

Mixing in general occurs in a diverse variety of processes and phenomena throughout the universe. Thus, to understand the universe, and affect change within it, mixing is an important phenomenon to understand. In some cases, mixing is induced by instabilities in the systems involved, and sometimes this mixing leads to a transition to turbulence, which enhances mixing further. Understanding this process from onset of instability, to early mixing, and possibly to a well-mixed turbulent state has been the subject of much research.

Specifically, a situation in which a shock drives this instability is known as Richtmyer-Meshkov Instability (RMI). This instability produces flows consisting of a wide range of scales, both temporal and spatial, and with a wide range of energy content as well. RMI flows occur in very large systems such as interstellar phenomena [3, 4, 5], to smaller supersonic combustion systems [6, 7, 8], to even smaller scales such as Inertial Confinement Fusion (ICF) implosions. The large range of scales and multiple physics involved in each instance make these phenomena difficult to simulate, prompting experimental work on the fundamental hydrodynamic problem of RMI.

In the aforementioned cases, understanding of the underlying hydrodynamics aids in understanding of how material is scattered from a supernova, improving design of Supersonic Combustion Ramjet (SCRAMjet) engines to enhance mixing of fuel and oxidizer using shock waves, and to improve the energy yield of ICF reactions. For instance, ICF reactions are degraded when a shock generated by ablating an outer shell directly or indi-

rectly using lasers passes through layers of varying density causing mixing of cooler shell material with inner material in a target pellet of hydrogen isotopes. Thus understanding the shock driven instability, or RMI, is important to understand and design mixing in a variety of applications.

The Richtmyer–Meshkov Instability (RMI) [9] occurs when a shock interacts with an interface between fluids of different density (pressure gradient interacting with a density gradient), and causes perturbations on the interface to grow according to the misalignment between the shock and the interface. Early study of RMI was performed by Richtmyer who extended the linear theory of Rayleigh–Taylor instability (RTI) [10, 11], which occurs when fluids of different density are oriented unstably (opposite sign of density and pressure gradients) in an acceleration field. However, RMI develops regardless of the orientation of the fluids relative to the direction of shock travel. Because Richtmyer modeled the gravitational term as an impulse, RMI is often considered to be the impulsive limit of RTI. The development of the interface in both instabilities is described by the vorticity equation for compressible flow,

$$\frac{D\boldsymbol{\omega}}{Dt} = (\boldsymbol{\omega} \cdot \boldsymbol{\nabla})\boldsymbol{u} - \boldsymbol{\omega}(\boldsymbol{\nabla} \cdot \boldsymbol{u}) + \boldsymbol{\nabla} \times (\frac{1}{\rho}\boldsymbol{\nabla} \cdot \boldsymbol{\tau}) + \frac{1}{\rho^2}(\boldsymbol{\nabla}\rho \times \boldsymbol{\nabla}P). \tag{1.1}$$

The left side of the equation, $\frac{D\boldsymbol{\omega}}{Dt}$, is the material derivative of vorticity. The first term, $(\boldsymbol{\omega}\cdot\boldsymbol{\nabla})\boldsymbol{u}$, is the vortex stretching term, and the second term, $\boldsymbol{\omega}(\boldsymbol{\nabla}\cdot\boldsymbol{u})$, is the vortex dilation term. These first two terms are negligible upon incident shock, considering the interface is stationary. The next term, containing τ, is negligible upon incident shock as well as throughout most of the flow due to high Reynolds number of the flow, which indicates that viscous effects are less dominant. Therefore an approximation for the vorticity equation is

$$\frac{D\boldsymbol{\omega}}{Dt} = \frac{1}{\rho^2}(\boldsymbol{\nabla}\rho \times \boldsymbol{\nabla}P). \tag{1.2}$$

Equation 1.2 highlights the mechanism by which vorticity is deposited along the interface by the shock, known as baroclinic torque, which is the last term of Equation 1.1. Thus the important factors which determine the vorticity deposited are the fluid densities ($\boldsymbol{\nabla}\rho$), shock strength ($\boldsymbol{\nabla}P$), and the perturbation or misalignment (seen in the cross product). This deposited vorticity is responsible for the development of the interface according to Equation 1.1.

Early in the development, while the amplitude of the perturbation is very small compared to its wavelength, the growth of the perturbation is said to be linear, and linear theory is typically applied. Coincidentally, the growth of the interface also follows a linear trend in this regime. However, when the amplitude becomes comparable to the wavelength of the perturbation, the growth becomes nonlinear, and follows a power law trend, the power of which is still under investigation, due to complex secondary instabilities and increased chaotic motion [12, 13, 14, 15, 16].

Furthermore, if the initial energy input is great enough the flow will undergo a transition to turbulence, where intense fluctuations drive rapid mixing over a large range of length and time scales. Due to the rapid mixing which ensues, this transition, and the parameters which are factors in the likelihood of transition, its onset, and the statistical characteristics of the resulting flow are desirable to understand. Work to define the mixing transition in multicomponent flows has been undertaken by Dimotakis [17], who has provided criteria to define this transition. However, in unsteady/temporally evolving flows the mixing transition, and the resulting flow is still being investigated [18].

Recent work on transition to turbulence has suggested that there may be flows which retain some memory of initial conditions through transition, and that this is pronounced in instability-driven flows such as RMI [19, 20, 21, 22]. Therefore, in addition to understanding the onset of transition, much recent work in the field of RMI research has had a goal of understanding what characteristics of the flow after transition retain memory of

the initial conditions.

Typically, the conditions varied, consistent with the insights from Equation 1.2, have been the initial energy input from the shock, by varying the shock Mach number (M) which corresponds to $\boldsymbol{\nabla} P$, or the misalignment of the shock with the interface, by controlling the shape of the interface perturbations, which are characterized by α= η/λ, the ratio of their amplitude, η, to their wavelength, λ. There has also been work to investigate the effect of the strength of the density gradient, by varying the gases used. The density contrast is represented nondimensionally by the Atwood number, $A = (\rho_2 - \rho_1)/(\rho_2 + \rho_1)$, where the subscript 2 refers to heavy fluid while subscript 1 refers to light fluid.

1.2 Previous Relevant Studies

While the density contrast depends on the gas pair, various methods have been used to create the pressure gradient and vary the interface shape. To create a near-impulsive pressure gradient, Jacobs and Sheeley [23], and later Niederhaus and Jacobs [24] placed a test bed on a sled and accelerated the apparatus toward a spring near the end of the track. Then Chapman and Jacobs [25] extended this to a three-dimensional interface perturbation, while Kane et al. [26] studied a rippled shock wave in laser-driven experiments.

To create the interface, many early experiments used a thin membrane supported by a wire grid to separate the heavy and light gases. Using this technique, early experiments by Meshkov validated the initial analytical work of Richtmyer [27, 28]. Much of the early work was aimed at determining the behavior of the overall amplitude of the interface, and employed schlieren imaging as a primary diagnostic. This interface creation technique has been used frequently [29, 30], even recently in the work of Vetter and Sturtevant [31], which has been a benchmark for much computational work, which generally found agreement with the experiments, especially after reshock [32, 33, 34]. In addition to works focused on the growth of the interface, velocity statistics became of

interest to understand the turbulent mixing layer better. In the late 1990s, the first statistical analysis of the velocity variance was performed using Laser Doppler Anemometry (LDA) before and after reshock on a Heavy-over-light configuration interface produced using the membrane method with a shock of about $M \sim 1.45$, however in the sulfur hexafluoride [35]. Because of the difference in averaging technique and differences due to the essentially negative Atwood number, these experimenst elude direct comparison with the current work. However these experiments represent a milestone for statistical turbulence analysis and inspired the types of experimental technology in use today.

Although membranes are still successfully employed, the membrane breaks into fragments upon shock which can be detrimental to visualization and even affect flow development. Therefore, membrane-less techniques of interface creation have become desirable. The problem of membrane-less techniques lies in creating a perturbation on the interface without the aid of a solid membrane. This problem has been solved in many ways. One way of creating a perturbation was by separating the gases with a soap film, which imparts less of the undesirable effects of the solid membranes.

Membrane-less methods have produced much information about RMI development because of the myriad of geometries that can be generated. The interaction of a bubble of different density with a shock was studied extensively experimentally [36, 37], and computationally [38], and thoroughly reviewed by Ranjan [39] providing a framework to understand the shock-focusing and -diverging effects upon interaction with curvature in the perturbed interface as well as shear and vortical development [40]. Furthermore, using this soap film method, various other geometries have been studied to provide a library of information on the morphology of RMI development from inhomogeneities and various single interfaces [41, 42, 43].

Another technique used also involves an inhomogeneity as the subject, rather than a single interface; cylinders of gas have been flown through the test section creating a two-

dimensional inhomogeneity. Although the subject is still an inhomogeneity, these experiments provide benefits beyond the membraned experiments because the continuous flow of gas allows a slightly diffuse interface to be created without any membrane. A single cylinder has been used [44] as well as arrays of cylinders [45]. Early experiments provided initial insight into the mixing rate of the inhomogeneity with the surrounding gas, the morphology of the flow, and, in the latter case partial velocity fields. With time, pivotal conclusions have been gleaned from these experiments. Vastly different flow fields resulted from gas-curtain experiments initialized using three different configurations of nozzles, which showed how the initial vorticity deposition profile could be stable, or unstable and result in vortical advection over greater distances, evidenced even after reshock [46].

While much has been learned from studying the interaction of a shock with various inhomogeneities, the second interface of the inhomogeneity introduces additional complication to the flow. Single interfaces, however, which is type used in the current work, have been created using a membrane-less approach as well. Gases are typically flown from either end of the test section, and meet at a stagnation plane where they exit through slots. Perturbations have been created on the resulting interface using various techniques. For instance, in the validation of a scaling law, pistons were used to create a near-sinusoidal standing wave on the interface [47] following Jones and Jacobs [48], Collins and Jacobs [49], Jacobs and Krivets [50], who oscillated the entire tube to produce a near-sinusoidal perturbation.

In addition to these near-single-mode interfaces, there has been interest in understanding how more complex interfaces, where a broader range of scales is present, behave under similar forcing. Further studies have shown that the modal content of the interface is a key factor in mixing and possible transition and several works have imposed random-mode initial conditions on an interface to study how the scales present in the initial con-

dition interact. One method creates Faraday waves on an otherwise flat interface, which is achieved by vertically oscillating the column of gases [14]. Other groups have utilized a shearing Kelvin–Helmholtz (KH) type instability at the interface to impose a complex, multi-mode perturbation between the gases. This method allows for the creation of a specific range of initial amplitudes and wavelengths to study the effect of initial conditions on instability evolution and the eventual transition to turbulence [51]. Weber et al. [51] achieved a turbulent mixing transition before reshock for an initial condition consisting of structures with small separation of length scales. While these multi-mode interfaces have furthered the understanding of the impact of initial interface perturbations, their stochastic nature requires large ensembles to be collected to produce reliable statistics, or otherwise, continuous imaging of the interface to truly correlate experimental times.

As in experimental work, computational studies have concentrated on modeling the instability evolution originating from different initial conditions, with most work focusing on understanding the evolution from well-defined, two-dimensional, harmonic initial conditions. Furthermore, just as advances in simulations have bolstered RMI experiments, the improvement of experimental diagnostic capabilities have improved the fidelity and breadth of information available for validating and improving simulations. Schilling et al. [52] performed simulations of single-mode RMI before and after reshock and the results were compared to the planar laser induced fluorescence (PLIF) experimental work by Collins & Jacobs [49]. Latini et al. [53] compared dissipation effects using weighted essentially non-oscillatory (WENO) methods of different orders.

A computational study of RMI development from an inclined interface covering multiple incident shock strengths, initial interface inclinations, and Atwood numbers using the ARES code was performed by McFarland et al. [54]. The research covered experiments performed on the same shock tube as that on which the present work was completed. ARES code was also used to investigate late-time development of RMI in shock tubes by

Morgan et al. [55], and was later compared with a compressible version of the Miranda code [56, 57].

The mixing layer evolving from different three-dimensional, multi-mode, small-scale initial perturbations was investigated numerically by Thornber et al. [58, 59] using implicit large-eddy simulation (ILES) with systematic grid refinement. The mixing layer in this study was shown to transition to a turbulent state.

An interface perturbation consisting of a long-wavelength inclined mode and another consisting of a short-wavelength multi-mode perturbation superimposed on the inclined interface (modeled after experiments in consideration at the time for the current facility) were initially investigated using ARES simulations by McFarland et al. [60]. Thus the conditions (Mach number, gases used, interface inclination angle) in the McFarland study are similar to those of the current study. The study includes an extension to 3-D and other improvements upon the work in [54] as early simulations had some differences in the qualitative results. These simulations included a large range of parametric variations including the perturbation, resolution, and boundary conditions. As the flow approached a turbulent state post-reshock, it only retained some memory of the initial conditions for high-amplitude large-wavelength perturbations. However, both large and small scales exhibited a distinct memory of the initial condition before reshock. A computational study of RMI at various Atwood numbers was also executed using large-eddy simulation with an explicit subgrid model by Lombardini et al. [61].

The results and conclusions of the parametric computational work by McFarland et al. and Lombardini et al. have a large influence on the first objective of this thesis. While there have been several computational Atwood number studies, and experimental works have been performed at various Atwood numbers, there are no experimental works known to the current author which have provided a comprehensive analysis of turbulence statistics at multiple Atwood numbers with the same incident Mach number and initial

conditions. Therefore, in light of the recent work performed by Mohaghar et al. which focused on the effects of initial perturbation and and Mach number [62, 63, 64], one of the biggest open questions in the study of RMI is the effect of Atwood number.

While early measurements of RMI in shock tubes used schlieren photography to primarily investigate the growth of the overall mixing layer [27], this is a volume-averaged method and planar techniques such as mie scattering, Planar Laser Induced Fluorescence (PLIF), and Particle Image Velocimetry (PIV) have since become increasingly common, and provide more robust descriptions of the flow (such as mixed mass and turbulent spectra). Conventional research efforts on these fronts have used simultaneous measurements of velocity and density using large ensembles of uncorrelated (and independent) experimental runs with identical initial conditions.

Recently a qualitative description of the morphological evolution of the interface and analysis of the growth rate of the mixing region have been provided in high-speed mie scattering and schlieren movies [65, 14, 41, 66]. While these results do provide qualitative information about instability growth and mixing phenomena, their direct utility in providing benchmark validation data is limited. To this end, much pioneering work in the area of simultaneous PLIF and PIV has been performed [45, 67, 68], albeit using large ensembles of snapshots from repeated experiments. Simultaneous diagnostics are of interest to understanding the correlation between density and velocity fields, with considerable interest in the correlation between their fluctuations, and thus the turbulent mass-flux velocity that is critical to closing RANS models such as the BHR model [69], which are desirable for use in multiphysics simulations.

The challenges in experimentally studying and modeling such flows come primarily from the high-spatial-resolution requirements inherently imposed by the typical mixing scales [$\sim O(1 - 10\,\mu m)$ in laboratory experiments], coupled with their extremely short temporal scales [$\sim O(0.5 - 10\,\mu s)$]. These, together with the large scale flow evolu-

tion [$\sim\ O(10\,cm, 10\,ms)$] lead to large desired dynamic ranges from the diagnostics. These requirements have conventionally limited the spatio-temporal detail with which these phenomena could be investigated. These illustrative 'scale separations' are for typical laboratory experiments, and the actual application could involve $2-10$ orders larger separation than those seen in the laboratory.

Recent advances in high-speed imaging and laser sources are paving the way for overcoming these limitations by employing non-intrusive optical measurements in complex reacting and non-reacting flow environments. For example, burst-mode lasers and gate-intensified CCD cameras are used to examine the velocity flow-field of supersonic flows by employing very high speed PIV at up to a MHz-repetition rate in compressible jet flows [70], albeit at low resolutions and at considerable noise owing to the nature of the intensified imaging system. At conventional high-speed resolutions, Wernet [71] and Beresh et al. [72] have made PIV measurements over hot and cold jets, supersonic jet in cross-flow and transonic flow over a cavity at acquistion rates $\sim O(10\,kHz)$. Similarly, Wagner [73] have implemented PIV in the wake of a cylinder in a shock-tube to study the harmonics of the transient wake growth.

Besides PIV, the application of pulse-burst systems have been demonstrated for high-speed reactive- and passive-tracer PLIF (for example, qualitatively by Michael et al. [74]), thermometry [75], etc. Additionally, akin to the current work, Miller et al. [76] have demonstrated the ability for simultaneous velocity and qualitative-PLIF measurements at $10\,kHz$ using pulse burst systems. Numerous other application-specific implementations of high-speed diagnostics have been presented in the thorough review of Thurow et al. [77]. The current work extends this spatial and temporal dynamic range [$\approx O(100\,\mu m - 100\,mm)$ and $\approx O(10\,\mu s - 10\,ms)$] simultaneously in velocity and concentration/density fields to enable studies of shock-driven mixing-related physics that were previously not possible due to insufficient dynamic range.

In addition to understanding the effect of Atwood number, the evolution of vorticity is of specific importance to the evolution of RMI (similar to its importance in many instabilities). The initial vorticity deposited by a shock on an interface has been modeled from linear theory and the Samtaney-Zabusky Model [78], which achieved an accurate comparison to experiments. Furthermore, Balakumar et al. [79] showed that the vortex configuration resulting from the initial shock advects material and neighboring vorticies, which strongly affect the extent of the mixing region and the state of the field that interacts with the reshock wave, highlighting the importance of vorticity throughout the development of RMI. However, as secondary instabilities develop, the flow departs further from linear theory, and thus it is difficult to model complex interactions which follow this regime into the transition and to turbulent mixing. These secondary instabilities have been discussed by Schilling, Latini, and Don [52] who showed the production of vorticity even after shock passage to be significant using numerical simulations of a M=1.21 accelerated interface between air and SF6, however there is currently no experimental work describing the temporal evolution of vorticity in RMI, much less in conjunction with density field evolution, to study the vortex interactions and induced mixing.

1.3 Objectives and Outline of Present Work

The present experimental study aims to address the following objectives:

1. **Investigation of the influence of Atwood number on RMI**

   The effect of Atwood number ($< A <$) on RMI is studied via experiments performed at A =0.23 and A =0.67. The work will study growth of the perturbation and mixing rate and probe the existence of self-similar scaling laws in shock-driven flows. Transition of the flow to a turbulent state will be examined along with the critical Reynolds number necessary for transition in these flows. The same shock strength (M$\sim$1.55) and light gas will be used for both Atwood numbers to ensure

consistency in as many parameters as possible between the cases. The effect of Atwood number on development and turbulent mixing transition after reshock for a perturbed, multi-mode, inclined interface with an amplitude to wavelength ratio of 0.088 (tube inclination of 80°) at the same non-dimensional times (based on amplitude growth scaling) between cases will be examined through ensemble-averaged turbulence statistics from simultaneous planar laser induced fluorescence (PLIF) and particle image velocimetry (PIV) measurements. Qualitative analysis of density and velocity fields will be performed as well as analysis of integral quantities such as mixing width (amplitude), mixedness, the density-specific-volume correlation (DSC), turbulent mass flux, Reynolds stress including anisotropy and Boussinesq considerations, as well as spectral and Reynolds number analysis.

A summary of the experimental study in this thesis is presented in Table 1.1. For all cases, the complete evolution of density fields are included. The experimental times for turbulence statistics in the table are the ones which were chosen to extract turbulence statistics through several realizations (more than 30 realizations at each time). For instance, 97 runs were used for the latest post reshock case.

2. **Temporally resolved measurements to study simultaneous density and velocity field evolution in RMI and understand the role of vorticity dynamics on mixing in shock driven instability flow**

   PLIF and PIV are performed simultaneously to yield density and velocity fields respectively at high temporal resolution at A$\sim$0.22, and A$\sim$0.67 with a primary focus on analysis of results from the former. The development after reshock will compose the bulk of the study, as it provides a nearly stationary evolving interface in a single window, where a longer development can be captured. Due to additional difficulties involved with the high speed diagnostics and time limitations on equipment usage, a large ensemble of data is not feasible at this time, and thus certain statisti-

Table 1.1: Overview of the experimental study: In addition to the entire development series for each of the cases below, specific experimental times were chosen to analyze turbulence statistics where between 30 and 100 runs were collected depending on convergence criteria

Case no.	**1**	**2**	**3**	**4**
Gas pair	(N_2-acetone)/ CO_2	(N_2-acetone)/ CO_2	(N_2-acetone)/ SF_6	(N_2-acetone)/ SF_6
Initial Condition	Single-mode	Multi-mode	Single-mode	Multi-mode
Mach number	1.55	1.55	1.55	1.55
Initial Atwood number	0.22	0.22	0.67	0.67
Experimental times for turbulence statistics	2 pre-reshock 2 post-reshock	2 pre-reshock 2 post-reshock	2 post-reshock	1 pre-reshock 2 post-reshock
Inclination angle of tube (Degrees)	80	80	80	80

cal quantities will not be calculated. Recommendations for a future large-ensemble high speed campaign are made. However the temporally-resolved evolution of instantaneous quantities with time is calculated for the first time in RMI flow. These results will be compared with high resolution results to demonstrate agreement and detail captured. The distribution of kinetic energy in the flow will be analyzed over time, and Integral circulation over time will be discussed. Vorticity will be analyzed in detail, due to its importance in RMI development [79]. Specifically the vorticity deposited by reshock will be analyzed and the models of Samtaney, Ray, and Zabusky (SRZ98,[1]) and Weber, Cook, and Bonazza (WCB2013, [2]) will be compared with the current work at each point along the interface. The importance of temporally resolved measurements will be demonstrated by capturing evolution of short time-scale events which can vary run-to-run due to the nature of the RMI.

The organization of this dissertation is as follows. In chapter 2, the experimental facility and conditions are detailed. Chapter 3 describes the PLIF image processing and PIV

processing to obtain density and velocity data respectively, as well as the processing of the high speed results, and uncertainty and error analysis in PLIF/PIV results are quantified. Chapter 4 first gives a qualitative analysis of the density fields from the processed PLIF images showing the temporal evolution for each of the cases for Atwood number comparison. Then, a complete quantitative analysis of the flow field using PLIF and PIV data is given, and finally an analysis of the transition of the flow towards turbulence is provided. Chapter 6 provides the conclusions for this study, overarching contributions to the field, and suggestions for future work.

CHAPTER 2

EXPERIMENTAL SETUP AND DIAGNOSTICS

2.1 The Shock Tube Facility

To achieve these goals, the Georgia Tech shock tube pictured in Figure 2.1 at the Shock Tube and Advanced Mixing Laboratory (STAMLab), widely known as the Georgia Tech Shock Tube and Advanced Mixing Laboratory Inclined Shock Tube Facility (GTSTAMLISTF) was used to perform the current experiments. Shock tubes in general have been used for a variety of purposes from materials research to medicinal delivery devices, and can be a variety of sizes. The shocks are produced by quickly releasing high pressure gas by breaking a diaphragm or opening fast-acting valves, or generated using higher energy methods such as laser ablation. The Georgia Tech shock tube has been described elsewhere, but the salient details are reproduced here for completeness. A thorough description of the tube's design is presented in the work of Jacob McFarland [80].

The total length of the Georgia Tech shock tube is 9 m and the internal cross section is a square measuring 11.43 cm by 11.43 cm. The tube is designed to withstand incident shock strengths of $M < 3$ in air. The entire tube is mounted on an I-beam, such that sections can be shifted and exchanged, making the entire tube modular. Furthermore, the unique inclined design of the tube allows a stable interface to be formed parallel to the ground while the angle of the whole tube can be changed from horizontal to 90°.

The components of the shock tube are shown in Figure 2.2. The Georgia Tech shock tube uses the diaphragm method to produce the shock. The diaphragm is located between the driver, which is initially at high pressure, and the driven section, which is initially at lower pressure. It is held in place using a high pressure hydraulic clamping mecha-

Figure 2.1: Photograph of the shock tube shown as configured for the current experiments.

nism. A sudden inflow of high pressure gas into the driver bulges the diaphragm against an x-shaped blade as shown in Figure 2.3. A diaphragm of material and thickness is selected which produces the desired shock strength in the current gases. Figure 2.4 shows a metal diaphragm which has been broken; clear polycarbonate was used for the current experiments, but aluminum is more visible in photographs.

When the diaphragm bursts, the high pressure gas expands into the driven section (the long yellow section in Figure 2.2) suddenly creating a pressure disturbance that travels faster than the speed of sound. The dynamic break of the diaphragm provides a more repeatable strength shock. The driven section primarily serves to ensure that the shock has fully coalesced and is completely planar when it reaches the interface creation location in the test section. The diagnostic system is triggered by a pair of pressure transducers

just above the interface creation location. These transducers are located 10 cm apart to allow shock velocity to be calculated each run.

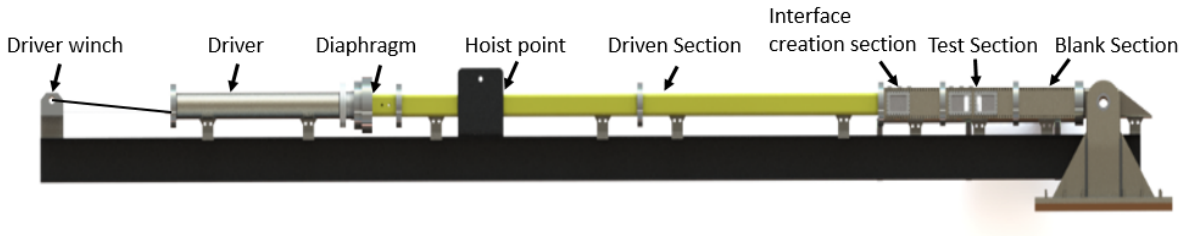

Figure 2.2: Model of shock tube shown configured horizontally with components labeled.

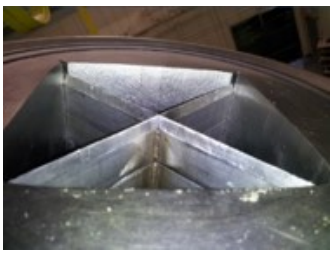

Figure 2.3: Photograph of the x-shaped blade upon which the diaphragm bulges when under pressure, causing a sudden break of the diaphragm

Figure 2.4: Example broken diaphragm (aluminum shown for visibility, whereas polycarbonate is used for the current experiments).

The test section is where observations of the interface are made through windows which can be configured to suit the current experiments as shown in Figure 2.5. The side walls can also be replaced with full-length acrylic windows. The modular construction allows the interface to be created at various distances from the end wall, changing the

development time before reshock, which is when the reflected shock from the end wall hits the interface. The method of interface creation involves flowing light gas from the top of the tube in the driven section, and heavy gasses from the bottom of the test section. The gasses meet at a stable stagnation plane in the interface creation section and exit on either side of the tube through outflow slots connected to a vacuum pump. A window at interface creation allows the interface to be imaged perpendicular to the illuminated interrogation plane.

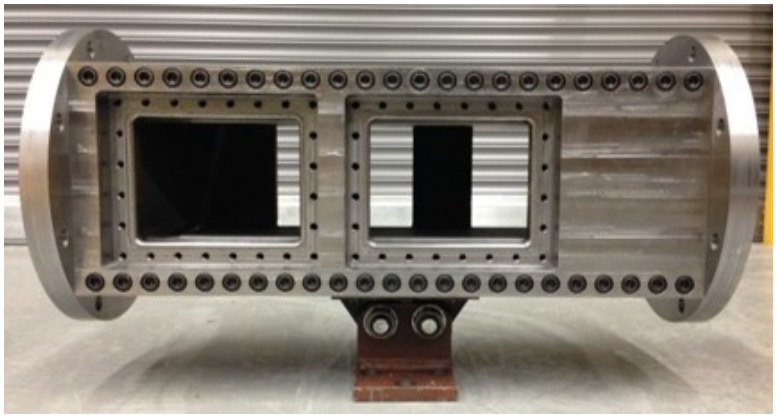

Figure 2.5: Module of test section showing staggered windows, modularity by section, and ability to change configuration of each module.

2.2 Present Experimental Configuration and Parameters

Various configurations of the Georgia Tech inclined shock tube have been described by Reilly [81], so the details of the current configuration are described here. In the current experiments, the shock tube is configured to 80° from the horizontal, which creates a 10° misalignment between the shock and the inclined interface. The entire shock tube was originally located at Texas A&M University. It was moved to Georgia Tech in July 2014, at the same time as when I joined STAMLab. I was able to be an integral part of the setup process in the new location at Georgia Tech, learning many new things along the way. A part of this process, where the whole tube was just reassembled, and its mounting was

being verified is shown in Figure 2.6 along with previous Master's student David Reilly.

Figure 2.6: Georgia Tech shock tube just after first assembly, being hoisted to test structural integrity. Previous Master's student David Reilly (6'4") shown for scale.

Furthermore, due to spatial constraints of the support structure, the support for the tube could not be placed as close to the axis of rotation as would be necessary to acheive an 80° inclination angle as desired for the current experiments. Therefore, a support extension was required to interface with the I-beam upon which the tube is mounted. This extension was designed and fabricated to interface with the shock tube such that force was transferred to the existing structure in the way it was designed and such that no modification of the existing support structure was needed, and to alleviate concerns about the off-design use of the support. In the resulting design, only two small bolt holes were necessary in a nonstructural part of the existing support structure and using material effectively.

The specific parameter of interest in this study is the Atwood number (A), which represents the nondimensional density contrast. Therefore, consideration was made to select the Gas pairs for these experiments to produce a low Atwood number for the first set and a high one for the second. The gas pair for the first set of experiments is Nitrogen (seeded with acetone) over Carbon Dioxide which results in an Atwood number $A = 0.22$.

Table 2.1: The properties of gases for the two different Atwood number cases. i is after incident shock, r indicates after reshock and t is an indicator of transmitted shock. 1 and 2 indicate light and heavy gases respectively.

A	0.22	0.67
A^i	0.236	0.73
A^r	0.253	0.76
M_i	1.55	1.55
M_t	1.61	1.83
M_r	1.525	1.77
W_i (m/s)	548	548
W_t (m/s)	492	266
V_0 (m/s)	257	257
Acetone(% Vol.)	8.3	8.3
ρ_1 (kg/m^3)	1.166	1.166
ρ_2 (kg/m^3)	1.84	6.15
ρ_1^i (kg/m^3)	2.451	2.921
ρ_2^i (kg/m^3)	3.97	18.67
ρ_1^r (kg/m^3)	4.391	4.922
ρ_2^r (kg/m^3)	7.368	35.47
T_1^i (K)	403	424
T_2^i (K)	386	340
T_1^r (K)	510	518
T_2^r (K)	471	369

The diaphragm material is 0.03 in thick polycarbonate, which produces a $M = 1.55$ shock in the Nitrogen. Results from this set of experiments were published, and some of the information is repeated here for completeness [62]. The heavy gas used in the second set of experiments is Sulfur Hexafluoride, resulting in $A = 0.67$. The Mach number is the same between the campaigns. Table 2.1 contains relavent properties for the two campaigns.

It is of interest to know where approximately the interface and the various waves generated will be as the experiment progresses. The driver used is 2 m long (a 1.5 m driver can also be used), and the interface is created at 5.5 m from the diaphragm, or 1.5 m from the end wall of the tube. The progression of these contact surfaces, as well as the pressure contours is visualized using an x-t diagram generated from 1-d gas dynamics

pressure information calculated using a code developed at the University of Wisconsin. These plots are used to aid in timing of the diagnostic equipment.

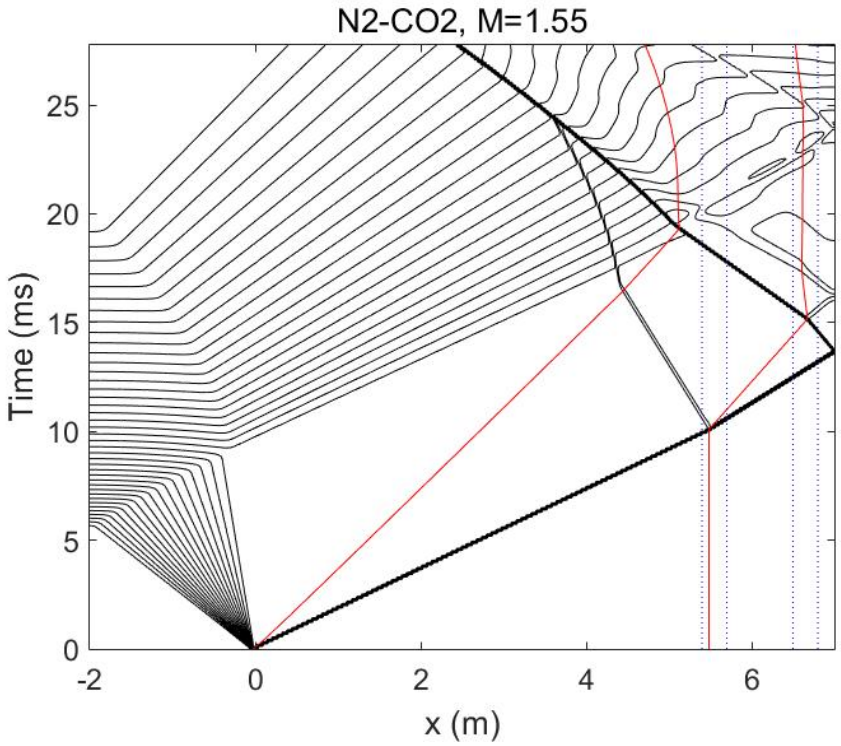

Figure 2.7: Plot of pressure contours for the low Atwood number experiments to show the time locations of pressure waves throughout the experiment along with the interface in red and window locations in blue.

2.3 Interface Creation and Characterization

The particular method of interface creation is important to characterizing the problem current experiments. The base case, the inclined interface, is formed by flowing light and heavy gasses from the top and bottom of the tube respectively. The outflow location is where the interface between the gases forms. By replenishing the gases at the interface a small diffusion thickness is maintained, and by not flowing the gasses too fast, instabilities are avoided to produce a flat interface. Figure 2.9a shows the method of creation of the inclined interface which is referred to as the single-mode interface in this work, and Figure

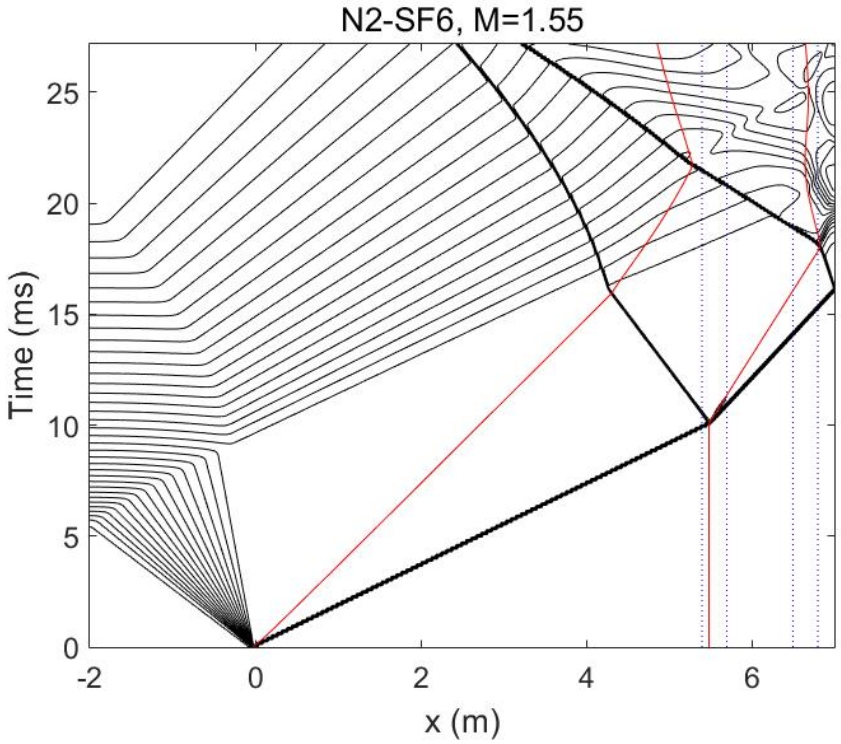

Figure 2.8: Plot of pressure contours for the high Atwood number experiments to show the time locations of pressure waves throughout the experiment along with the interface in red and window locations in blue.

2.9b shows the concentration field of the interface produced using this technique.

Although the interface is half a triangular wave, it is often convenient to approximate it as sinusoidal. Mikaelian notes that the first term of the Fourier expansion for the triangular wave contains 81% of the information. This coefficient describes how well a singular sinusoidal wave approximates the inclined interface. Thus, considering the inclined interface as single-mode, either as a triangular wave or as a sinusoidal wave, is justified. This stable inclined interface is the motivation behind the inclined design of the tube, which allows the angle to be adjusted to anywhere between 0 and 90°, controlling the misalignment between the shock and the interface in a repeatable, well-defined way. This thereby controls the cross product in the baroclinic torque term from equation 1.2.

In addition to a well-defined single mode interface, it was desirable to understand how

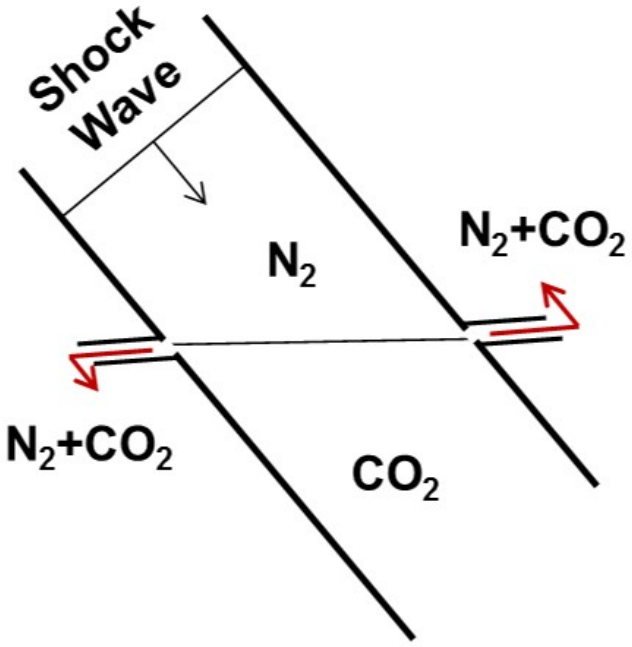

(a) Flow Schematic for single mode IC creation

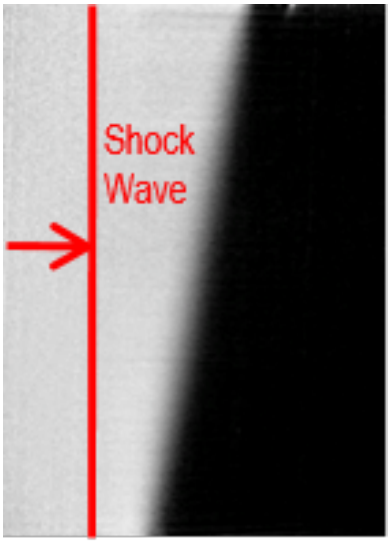

(b) Single Mode IC

Figure 2.9: Single mode interface creation: (a) Schematic showing the method of creating the interface utilizing a stable configuration and outflowing at the sides of the tube through slots connected to a vacuum pump. SF_6 is used instead of CO_2 in the high At experiments. (b) Concentration field image for the single mode initial condition, where intensity corresponds to mole fraction of N_2

additional modes would evolve, interact, and affect the resulting flow throughout transition to turbulence. The resulting interface is called the multi-mode interface in the current work. The multi-mode interface is naturally the subject of a portion of this study in relation to its efficacy at different Atwood numbers, but is not the main focus of this work, so it will be briefly described here for completeness. The study of this interface on this shock tube was initiated by Reilly [82], and a complete study including statistical investigation of its effects through the transition to turbulence was performed by Mohaghar et al. [62]. An investigation of its effects at different Mach numbers was also performed by Mohaghar et al. [63, 64].

To generate the multimode interface, a counterflow configuration of jets are added to the inclined interface such that the heavy gas is injected just above the interface, and the light gas is injected just below the interface as shown in Figure 2.10a, creating features along the interface due to shear and buoyancy effects, which can be observed in the sample concentration field image shown in 2.10b. The flowrates of the inflow gases were carefully calibrated to achieve consistent and desirable interface characteristics. It was desired to maintain the dominance of the large wavelength inclined interface, and simply superpose additional modes upon the inclined mode. Thus the amplitude of the additional modes was maintained around 1 cm, similar to the diffusion thickness. Also, the perturbations were kept near the center of the tube by maintaining a balance of momentum influx.

It was also desired to characterize the multimode interface. Since it is comprised of more complex characteristics, it can be helpful to consider a few different ways of describing it. The first way of describing the multi-mode interface is simply to consider a sample concentration field. This is what the interface looks like in general when a shock interacts with it, and this sample interface can be used to initialize 2-dimensional simulations. A sample interface is shown in Figure 2.11a.

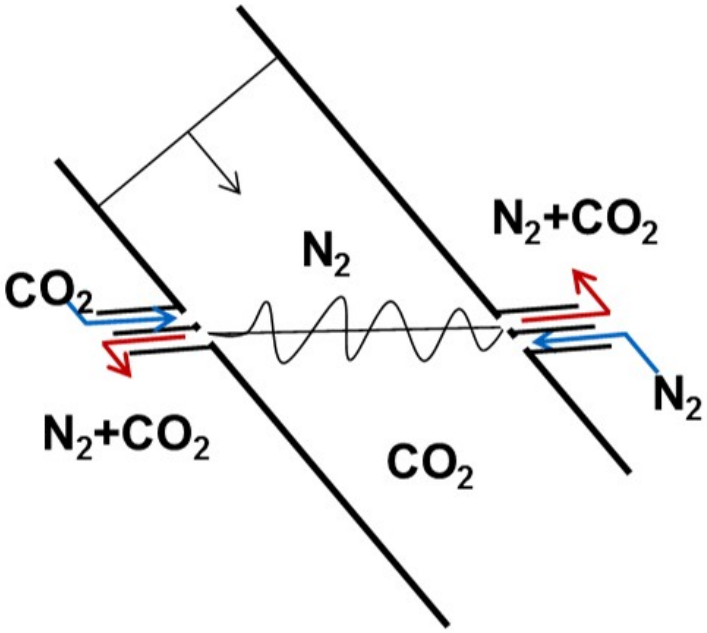

(a) Flow Schematic for multi-mode IC creation

(b) Multi-Mode IC

Figure 2.10: (a) Schematic showing the method of creating the multi-mode interface utilizing a stable configuration and outflowing at the sides of the tube through slots connected to a vacuum pump, while also counterflowing the light and heavy gases below and above the interface as shown. SF_6 is used instead of CO_2 in the high At experiments. (b) Concentration field image for the multi-mode initial condition, where intensity corresponds to mole fraction of N_2

To better understand the statistical results in this work, it is useful to analyze the initial interface condition statistically as well. Figure 2.11b shows the mean initial condition of the interface from 200 concentration fields. Figure 2.11c shows the standard deviation of the IC from the same 200 fields. The standard deviation values are about 1% of the max of the concentration field.

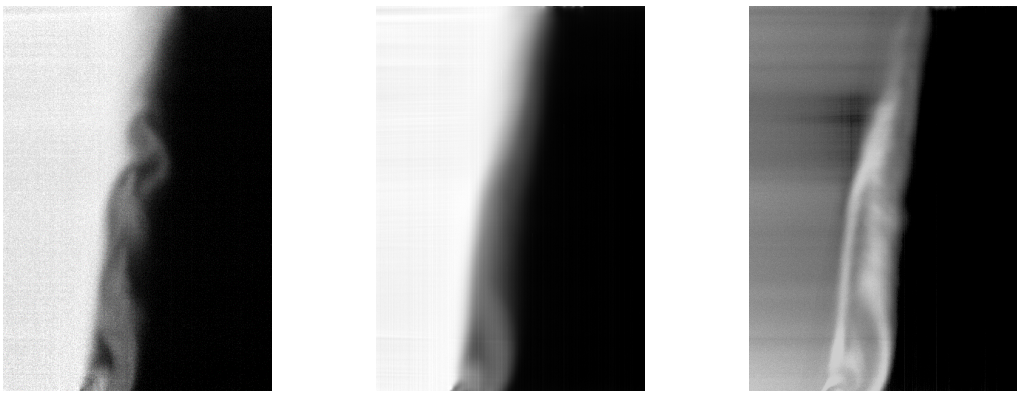

(a) Sample multi-mode IC *(b)* Ensemble Average IC *(c)* Standard deviation of IC

Figure 2.11: Statistical IC Characterization:(a) A sample initial condition concentration field for the multi-mode initial condition, where intensity corresponds to mole fraction of nitrogen. (b) Ensemble average of concentration from 200 multi-mode IC images. (c) Standard deviation from the 200 IC images.

To further understanding of the scales of the density contours upon which the shock impinges it is helpful to consider the spectral content of the interface. This analysis is also performed in [62]. Figure 2.12 shows this analysis.

To understand the shapes of these scales, and their degree of commonality, it is desirable to perform Proper Orthogonal Decomposition. This analysis is also performed in [62]. Figure 2.13 shows this analysis.

2.4 High Spatial-Resolution Diagnostics

To capture the density and velocity fields of the evolving flow simultaneously, the experimental instrumentation is configured to perform planar laser induced fluorescence (PLIF) and particle image velocimetry (PIV). Images are either captured at up to two times per

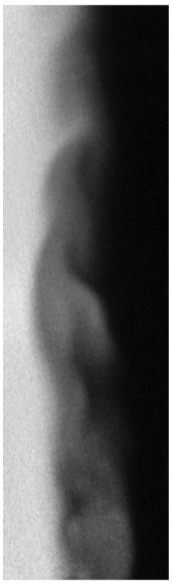

(a) Rotated IC

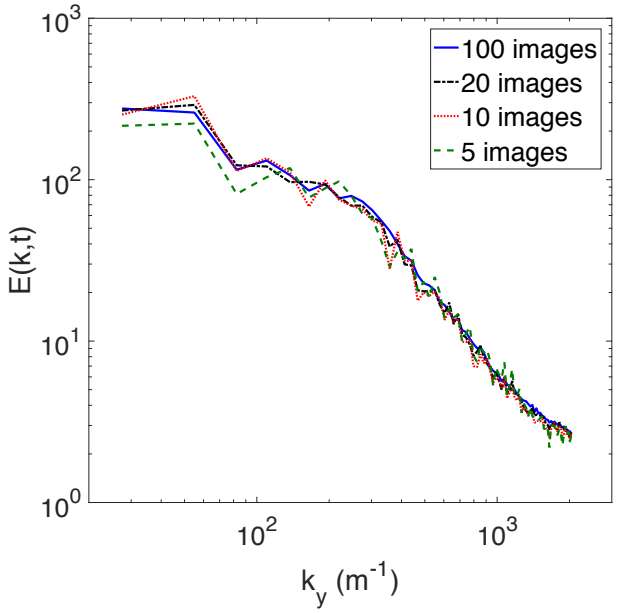

(b) Spectra of rotated ICs

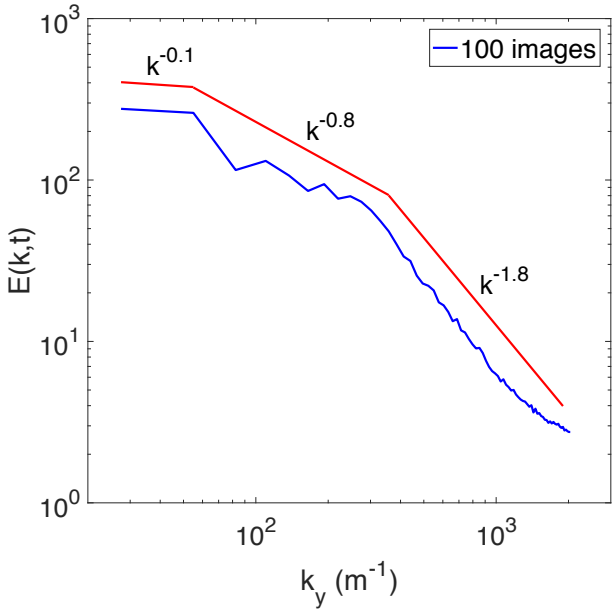

(c) Average spectra with fiducials

Figure 2.12: IC Spectral Characterization:(a) Multi-mode IC rotated 10°. (b) Averages of the spectra of various sample sizes of the rotated multi-mode IC (c) Average of spectra form 100 IC images with fiducial lines showing the slopes in several spectral ranges.

experiment with high spatial resolution or captured throughout the experiment at high frame rates. There are similarities in the methodology of the high resolution and high speed studies. First, the methodology for the high spatial-resolution experiments is de-

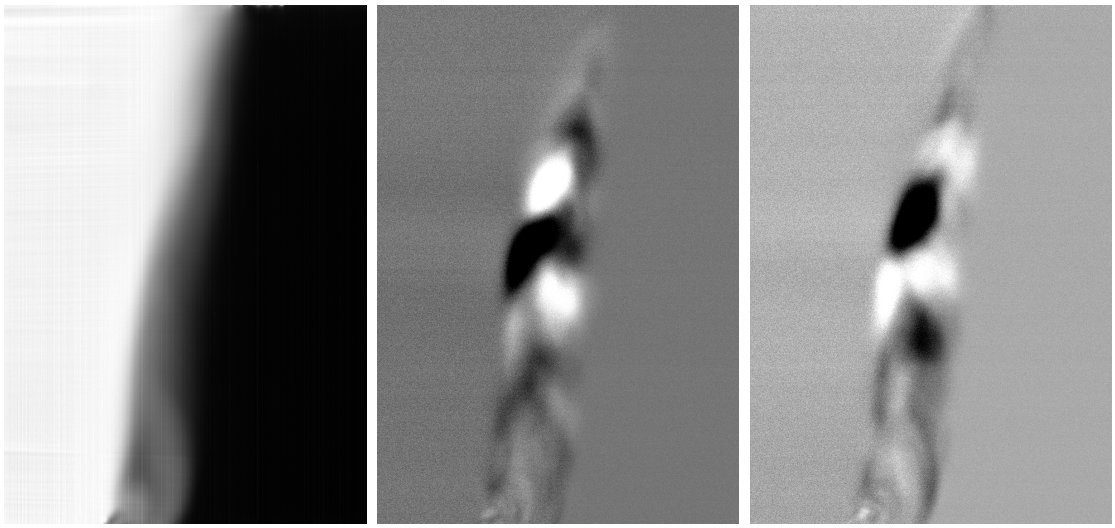

(a) Mode 0 *(b)* Mode 1 *(c)* Mode 2

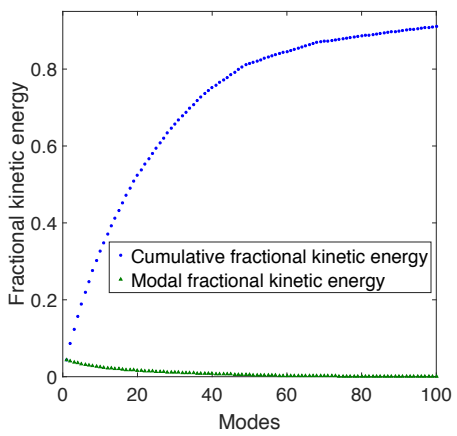

(d) Cumulative and Modal Energy

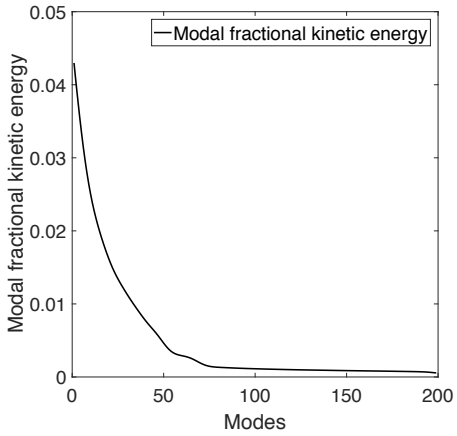

(e) Modal Fractional Energy

Figure 2.13: IC Spectral Characterization:a) Mode 0 (Ensemble average) b) Mode 1 (4.4% of total concentration field), c) Mode 2 (4.1% of total concentration field), d) The modal and cumulative fraction of concentration field e) Modal fraction of concentration field for all 200 modes.

scribed.

2.4.1 PLIF

To perform PLIF, a tracer which fluoresces upon excitation by a laser is added to one of the gases in order to measure the concentration of that gas. In these experiments, the tracer used was acetone, which was added to the light gas. The acetone vapor is

produced by bubbling the light gas through liquid such that the acetone vapor is saturated in the nitrogen gas. The acetone concentration at saturation is maintained by keeping the acetone at a constant temperature. Then additional pure nitrogen is added to achieve the desired final concentration, and avoid any condensation due to lower temperatures.

For the high-resolution experiments, the laser used to excite the acetone vapor was a Litron laser capable of producing a 266 nm pulse with each of two heads at 120 mJ per pulse. The light sheet is formed by diverging a beam to fill the test section. Converging and diverging lenses are also used to achieve a beam waist located at the imaging location. The beam waist was measured to be 0.65 ± 0.05 mm. A quartz window at the bottom of the tube allows the sheet to enter the test section. This is illustrated in Figure 2.14.

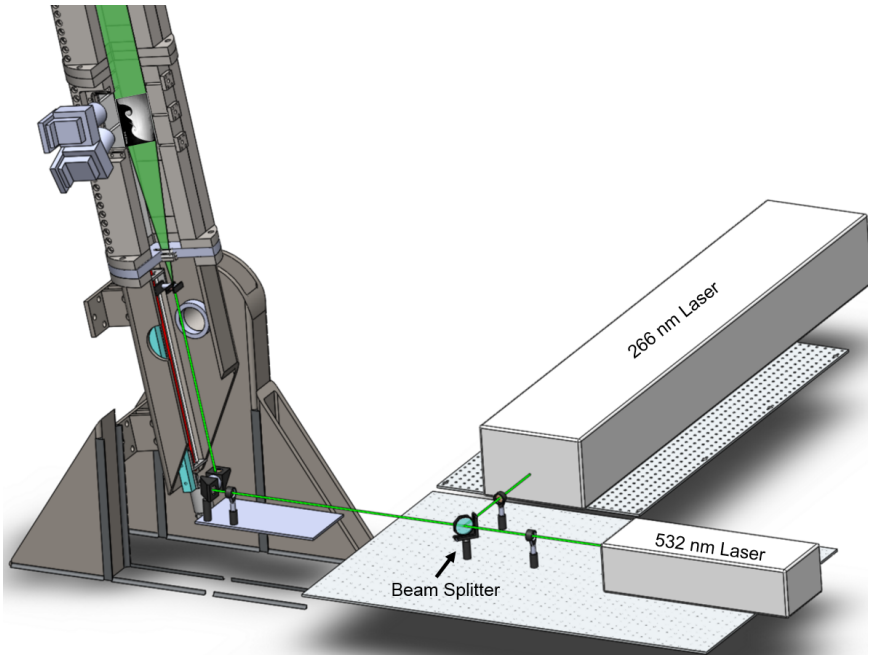

Figure 2.14: Schematic showing configuration of lasers, featuring combinaton, entry, and divergence. An example image is shown within the cutaway of the test section for reference.

An un-intensified TSI PowerView 29 MP CCD camera equipped with a 50 mm f/1.2 Nikon lens with an additional 2+ close-up lens is used to capture the fluorescence signal. To remove 532 nm wavelength light due to the PIV signal, a notch filter is also used. To

improve the signal-to-noise ratio, 2×2 binning is used. This results in a final resolution of $99\mu m/pix$ for high Atwood number and $72\mu m/pix$ for low Atwood number experiments. Due to space constraints, and to image approximately the same region, the PLIF camera is angled to 15° from perpendicular to the laser sheet. Using a traditional lens mount, the plane of focus is usually parallel to the camera sensor, therefore to adjust the plane of focus to align with the laser sheet a scheimpflug mount is used for the lens on the PLIF camera as shown in Figure 2.15.

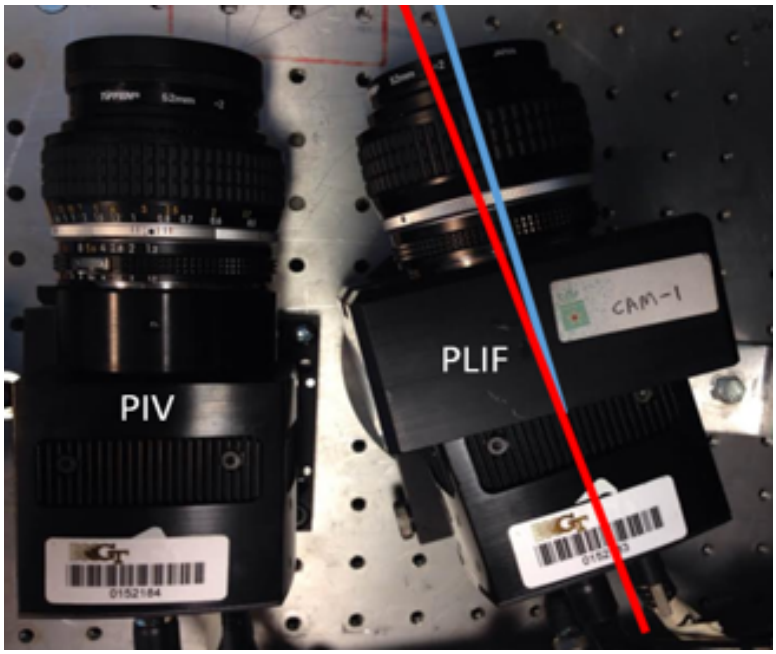

Figure 2.15: Schematic showing camera setup which adjusts the angle of the plane of focus by utilizing a schiempflug mount to angle the camera sensor relative to the lens.

2.4.2 PIV

To perform Particle Image Velocimetry (PIV), the flow is seeded with particles which are illuminated. Two intensity images are taken in close succession, allowing displacement of groups of particles to be estimated, yielding a velocity estimate when divided by the time between frames.

The particles used to seed both the heavy and light gases in these experiments were

titanium dioxide. The average diameter is between 0.3-1 microns. It is important to consider how well the particles will follow the flow, and thus represent the actual velocity field, when choosing particles to use for PIV. The relaxation time upon acceleration of the flow should be sufficiently low. For this flow, the highest acceleration is when the shock passes through the gasses; however accurately capturing this event is not of interest for studying the evolving flow which results. Nevertheless, the particles are estimated to lag no more than 1% of a pixel, which is smaller than the 10% subpixel resolution of the PIV technique itself. Therefore, particle lag is not a concern for error estimates. A laser sheet of 532 nm wavelength light from a dual-cavity New Wave Research Gemini PIV laser at 200 mJ is created in a similar manner to the PLIF laser sheet. The lasers are combined using a harmonic beamsplitter, and the beam waist is relocated for each imaging location. The thickness at the waist was measured to be $\sim 0.65 \pm 0.05$ mm using a knife-edging technique. PowerView 29-MP CCD cameras are used for both the PLIF and PIV imaging. A 532 nm bandpass filter and a 2+ close up lense are used on the PIV camera to filter other wavelengths of light than that of the PIV laser and to adjust the plane of focus, respectively. It is desired to maintain the laser sheet thickness small to minimize volume-averaging of the PIV technique [83]. Furthermore, minimizing laser sheet thickness reduces illumination of foreground or background particles outside of the depth of field which are out of focus. The depth of field is given by [84].

$$\delta z \simeq \pm 2.4 \left(\frac{1 - Mag}{Mag} \right)^2 \left(\frac{f}{2\sigma} \right)^2 \lambda. \tag{2.1}$$

In these experiments, $f/2\sigma$, or $f\text{-}number = 4$, $Mag \backsim 0.2$, and $\lambda = 532nm$, which results in a depth of field of $\delta z \simeq \pm 0.33$, which is approximately the same as the thickness of the laser sheet thus minimizing particles which are out-of-focus.

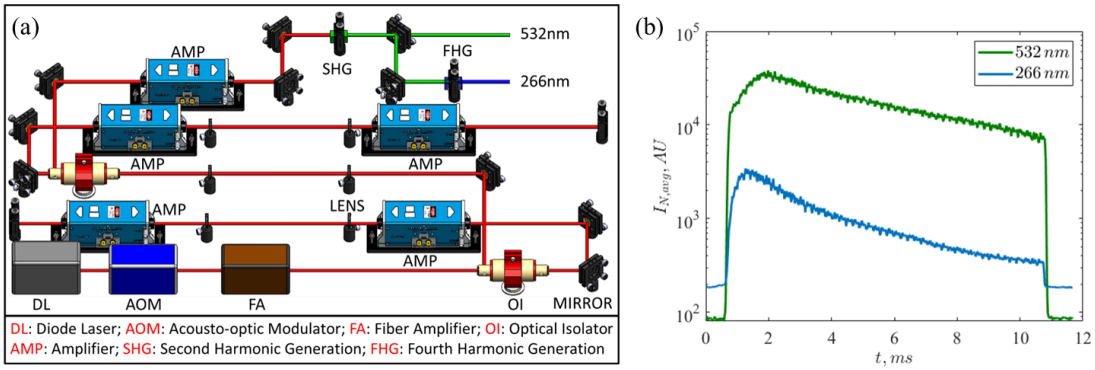

Figure 2.16: (a) Architecture of the burst-mode laser system, with the various components, and (b) laser power changes in $532\,nm$ and $266\,nm$ outputs as measured by mean intensity of PIV and PLIF images.

2.5 High Temporal-Resolution Diagnostics

High-speed diagnostics were tailored to study velocity and density fields simultaneously in shock-driven mixing flows for the first time, providing a blueprint to the scientific community for: laser configuration and architecture, imaging techniques, and overcoming some challenges associated with the diagnostic. The underlying principles of PLIF and PIV are the same; however, there are a few technical differences in the diagnostic equipment and execution of the measurement that result in different analyses that are made possible to provide a more complete description of the flow.

2.5.1 Laser Architecture

A specially-configured burst-mode laser is used as the light source for both PIV (at $532\,nm$) and PLIF (at $266\,nm$). The general architecture of the burst-mode laser has been described in detail in other works[85, 86, 87], so a brief overview will be given here, noting specific modifications for simultaneous diagnostics. The specific configuration used for the current experiments is shown in figure 2.16a. A flexible master oscillator is used which can produce tunable pulse widths by slicing the output from a $30\,mW$, $1064\,nm$ continuous-wave, narrow-band diode laser. A $10\,GHz$-bandwidth, Acousto-Optic Mod-

ulator (AOM) with an extinction ratio $> 50\,dB$ is used to perform the pulse splicing. The AOM is modulated by a pulse generator which can be controlled using the laser software. The sliced 1064-nm pulse train is amplified in stages, and final laser output can reach laser energies $\approx 1\,J/pulse$ at $1064\,nm$ at a repetition rate of $10\,kHz$ and a burst duration of $10\,ms$. At $100\,kHz$ repetition rate, the average laser pulse energy reduces to $\sim 100\,mJ/pulse$. The $1064\,nm$-laser is frequency doubled using a second harmonic crystal to produce $532\,nm$ light for PIV, and then doubled again to produce the fourth harmonic $266\,nm$ light for PLIF. For the current experimental conditions, a short burst of $532\,nm$ and $266\,nm$ pulses at $60\,kHz$ provided for about $10\,ms$ is sufficient to study the development of the interface, although the laser could be configured to operate at up to $1\,MHz$. The peak laser pulse energies respectively were $60\,mJ$ and $25\,mJ$, respectively.

The laser beam from the output is directed into the the shock-tube via a series of dual-wavelength mirrors and then through the same beam-shaping optics as the high resolution experiments to provide a sheet with a beam waist of $\approx 500\,\mu m$, which is slightly smaller due to a slightly smaller initial diameter. The focal-length and location of the cylindrical lens that generates the sheet were adjusted depending on the measurement location (windows, W1, W2 or W3) so as to optimize the amount of laser energy available for PIV and PLIF in the field of view and minimize sheet thickness.

2.5.2 Imaging and Challenges

Two Phantom SA-Z CMOS cameras were mounted next to each other in a similar configuration to the high resolution imaging setup. The cameras were mounted on a rail that enables moving the cameras along the shock tube depending on the interface location to be imaged. While the PIV camera was mounted perpendicular to the light sheet, the PLIF camera was mounted with a tilt ($\approx 15^{\circ}$) to enable imaging of the same field of view as that of the PIV camera. A scheimpflug mount was used to angle the plane-of-focus so that

the laser sheet was completely within the depth of field and in focus in a similar manner to the high resolution setup. Images of a calibration target were taken with both cameras at each imaging window to enable spatial calibrations and registration between the two fields. The CMOS cameras are capable of imaging at up to $20\,kHz$ at a full resolution of 1 megapixel. To temporally resolve the flow in current experiments, the cameras were run at a reduced resolution of $0.3\,MP$ but sampled at $60\,kHz$. Both cameras were fitted with Nikon $50\,mm$ lens, with a maximum aperture of $f/1.2$. The depth of focus of the imaging optics was around $5\,mm$ (at $266\,nm$) which is much larger than the laser sheet thickness.

To enable simultaneous measurements of velocity and density, both the gasses in the shock tube were seeded with $0.3 - 1\,\mu m$ TiO_2 particles for PIV, while the light gas (N_2) was additionally seeded with Acetone vapors. While the particles scatter the incident $532\,nm$ light, the acetone vapors absorb the $266\,nm$ light and fluoresce in the visible UV range (scattered $266\,nm$ light from particles is weak and is blocked by the acrylic windows that only allows visible light). Additionally, to enable simultaneous imaging of the mie-scattered $532\,nm$ light from the seeded particles and fluoresced light from the seeded acetone, the PIV camera was fitted with an Omega model 532BP10 $532\,nm$ band-pass filter (OD$\geq$3) transmitting only scattered light, and the PLIF camera images through an Edmund Optics TECHSPEC $532\,nm$ notch-filter (OD$\geq$4) that blocks the scattered light.

CHAPTER 3

DATA PROCESSING AND UNCERTAINTY ANALYSIS

The raw data collected during experiments undergoes several processes depending on the diagnostic technique and the quantities desired for extraction. As with all measurements, physical phenomena in the diagnostic systems are systematically accounted for to yield the final measurement. When this is all complete the measurement is a close estimate of the actual field values. Finally, considering the diagnostic system and statistics of the results, an estimate of error in the measurements can be made.

3.1 Quantitative Simultaneous PLIF and PIV Processing

The raw intensity images captured using PLIF are translated into concentration fields via a series of systematic corrections based on understood effects of the diagnostic and setup. This method was pioneered by Collins and Jacobs, and has also been used and outlined in other works [49, 51, 15, 62, 63, 64]. Pertinent details are given here for completeness. Due to the perspective effect of angling the camera, a de-warping algorithm in Insight 4G^{TM} is used. Because this process uses gridded calibration plate images, it also corrects distortion in the image from lens effects. To straighten the light rays in the image, the original image is resized by a factor of $\frac{1}{1-(\Delta x_L+\Delta x_R)}$, where Δx_L and Δx_R are the proportion of the image that each corner needs to shift from left and right side of the top row of the original image. This preserves resolution by upsampling the image instead of shrinking the image and losing information. Then the image is transformed according to the values Δx_L and Δx_R. Next, the decrease in intensity of the laser sheet as it diverges

radially from the plano-concave lens is accounted for geometrically via

$$I_{trans} = I\frac{y_{int} - 1}{y_{int} - y} \tag{3.1}$$

where I_{trans} is the intensity of the straightened image, I is the intensity of de-warped image, y is the vertical location of each row of the image from the top of the image, and y_{int} is the vertical location of the plano-concave lens relative to the top of image ($y = 1$ is the top row of the image).

The intensity measured is given by

$$I = gC_0\zeta J, \tag{3.2}$$

where g is the collection efficiency of the camera setup, C_0 is the pure light gas concentration, $\zeta = C/C_0$ is the actual normalized concentration (0-1), and J is the local laser intensity.

Attenuation of laser irradiation as the sheet travels through the light gas is another cause of spatial variation in laser intensity. Beer-Lambert law or Beer's Law describes this physical phenomenon and is thus used to correct for its effect. The attenuation depends on concentration and properties of the attenuating species, in this case acetone vapor, described by

$$\frac{dJ}{ds} = -\varepsilon C_0\zeta I, \tag{3.3}$$

where ε is the attenuation coefficient. Substituting Equation 3.2 into Equation 3.3 and then integrating yields

$$\frac{I_2}{gC_0\zeta_2} - \frac{I_1}{gC_0\zeta_1} = -\varepsilon/g\int_1^2 Ids, \tag{3.4}$$

where 1 is a reference chosen in the region of pure light gas where $C = C_0$ ($\zeta = 1$), and state 2 is each other point in the field. Then, Equation 3.6 is rewritten to calculate concentration at each point in the field as

$$\zeta = \frac{I(x,y)}{I_0(x) - \varepsilon C_0 \int_1^y I(x,y)dy} \tag{3.5}$$

where $I_0(x)$ is the intensity in the reference region of pure gas given by averaging over y and correcting for attenuation, with the condition of pure gas

$$I_0(x) = (\overline{I(x,y)e^{-\varepsilon/C_0 y}})_y. \tag{3.6}$$

The result of which is shown in Figure 3.1d.

Striations appear in the image due to the index of refraction mismatch between the gases which allows for very slight lensing of the laser light by perturbations on the interface. These striations are removed by notch filtering in Fourier space. This process is described in detail by Weber [88]. The image is made periodic by padding with a Hanning window and mirroring in each direction to create a 3×3 array. In Fourier space, the striations appear as a narrow band near $k = 0$ in the streamwise direction because they are long but narrow. The spectrum is replaced in this region using a method similar to [88] which was shown to preserve spectral content. The inverse Fourier transform is taken then the mirrored images and Hanning window are removed to produce the final image shown in Figure 3.1e.

In order to accurately register the PLIF and PIV images, the same calibration target (Figure 3.1b) is imaged with both cameras. The same dewarping algorithm as was used in the PLIF images is used to correct the particle fields prior to velocimetric analysis. This dewarping and the PIV calculation are performed using Insight 4G^{TM}. At experimental times before reshock, a rectangular grid is used with a 20 pixel offset to accurately capture

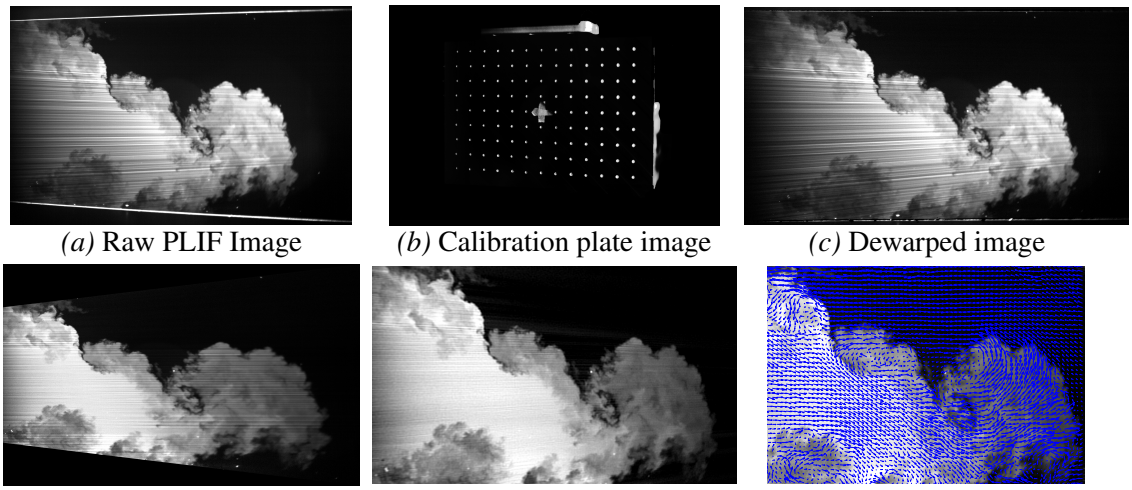

(a) Raw PLIF Image *(b)* Calibration plate image *(c)* Dewarped image

(d) Divergence and Beer–Lambert corrected image *(e)* Final processed image *(f)* Registered velocity and concentration fields

Figure 3.1: PLIF/PIV Processing:(a) A sample PLIF image as collected. (b) Image of the two-plane calibration plate which is used to correct for lens and perspective effects and to align the PLIF image to the PIV vector field. (c) PLIF image after dewarping is performed to correct lens and perspective effects. (d) PLIF image after correction for decrease in intensity at radial locations farther from the cylindrical lens due to divergence and for Beer–Lambert attenuation due to absorption. The image has been transformed in a way that does not decrease resolution in order to make rays parallel so that streaks appear as high frequency content in only one direction and low frequency content in the other (e) Final processed PLIF image after filtering of high frequency streaks due to index of refraction mismatch across the interface and reversing the aforementioned transformation. (f) An example showing 25% of vectors registered to the final PLIF image.

the fast-moving bulk flow. After reshock, because the bulk velocity is low, a recursive Nyquist grid is used. Smoothing and interpolation used produce more reliable estimates after inital passes, that yield more accurate final passes. Secondary peak replacement was used for vectors that surpass a universal median test based on a 3×3 neighborhood. A final spot size of 16×16 was used with a 50% overlap resulting in a vector spacing of 0.40 mm. A 5×5 Gaussian filter with standard deviation 0.8 was used to reduce spurious noise, and showed to have a small impact on small scale statistics. To have sufficient particle movement to resolve the velocity, a delay of 2.2 μs and 2.5 μs before and after reshock respectively.

Finally, the velocity vector fields are registered to the corrected concentration fields

so that simultaneous density-velocity calculations can be made. In order to not overstate the resolution, the resolution of the velocity fields are taken for joint calculations as this is the limiting resolution. Accurate registration of fields is important, and thus the same dewarping process that is used for the PLIF and PIV raw images is used for the calibration plate images. Then the same transformations that are applied to each of the two raw images are applied to the calibration images. Then the transformation (shift and and stretch because rotation was zero in both cameras) between the calibration images (to align the grids) is measured and applied to the results. The registration is demonstrated in Figure 3.1f where the connection between the concentration and velocity fields in this flow becomes obvious.

3.2 High Speed Processing

The PIV particle images were processed using Davis 8.4 software, using recursive grid refinement to a final interrogation window size of $24 \times 24\,px$ (50% overlap). This, given the magnification of the imaging, gives a spatial resolution of $4\,mm/vec.$ A $3 \times 3 \times 3$ spatio-temporal median filter was used for outlier detection along with vector replacement and Gaussian smoothing (to remove high frequency noise) in the PIV vector fields. The PLIF images presented in the current work are qualitative in nature and have a spatial resolution of $250\,\mu m$. The mean variation in laser intensity is corrected for using a median normalization given by,

$$I_c = \frac{I - I_{min}}{I_{med} - I_{min}} \tag{3.7}$$

$$I_N = \frac{I_c}{I_{c,avg}} \tag{3.8}$$

where I_N and I_c are normalized and median-corrected images, I is the raw image,

I_{min} and I_{med} are the minimum and median intensities of the image, and $I_{c,avg}$ is the average intensity of I_c. This median-based normalization results in accurate corrections for laser intensity, and is immune to outliers in individual images.

3.3 Error Analysis

Deviations of the measurements from the actual values can not be determined directly in most cases. However, an estimate of the possible deviation can usually be made by considering the possible sources of error in the experiments. Error in the density fields can result from low level noise in the raw images, reductions in bit depth, and inaccuracies in correction methods. Error in the calculation of velocity from PIV is more complex and depends on how well the particles follow the flow, how well the imaging system captures this motion, and how well the captured motion is resolved.

In the density fields, low-level noise from the CCD chip is about 2% of the range of intensities. This is of interest when the bit depth, or range of intensities, is reduced. The extinction coefficient can vary if acetone concentration is not uniform in the light gas. To prevent this, or essentially make this effect negligible, the acetone bubbler is maintained at a constant temperature to ensure consistent saturation concentration, the flow rates are maintained constant between the seeded and pure streams, and the streams are thoroughly mixed in a large mixing box prior to entering the shock tube. Index of refraction effects along the interface result in dark and light streaks which are corrected. However the dim streaks constitute a reduction in bit depth, meaning that the noise is a greater percentage of the range of intensities. Therefore, the error in the concentration fields is estimated to be 10% or less.

The error in PIV calculations is minimized by all means possible beyond the inherent error in the technique. The particles chosen follow the flow with negligible lag and the number density of particles is chosen to allow for good correlations between frames.

The out of plane motion and image quality can further affect the correlation between frames. With several factors affecting the uncertainty of PIV, one way of estimating the uncertainty is based on the ratio of the primary peak to the secondary peak and is called the Peak-to-Peak Ratio method (PPR) which yields an estimate of the error to be about 2% [89, 90].

The uncertainty in an estimator can also be estimated from the statistics of the results via the variance and number of realizations of the variable available based on the central limit theorem [91]. Thus the standard deviation for the estimator is given by

$$\sqrt{var(\hat{\phi}(x))} = \sigma_{\hat{\phi}} = \sqrt{\frac{\sigma_{\phi}^2}{N_i}} \tag{3.9}$$

where $\hat{\phi}(x)$ is an estimator for a statistic of random variable x and N_i is the number of independent samples. Therefore, some of the largest ensembles to date in this field were collected to more accurately capture turbulence statistics from the fluctuations which occur among runs which are independent in nature. For comparison with other experimental and computational research, the fields are averaged in the spanwise direction to produce profiles, which also demonstrate the variation of each variable throughout the mixing region. These spanwise averages contain a number of independent samples dependent on the integral lengthscale which is around 1 cm, and thus 10 independent samples are considered in the spanwise direction, multiplying the denominator, N_i, in Equation 3.9 by a factor of ten. Additional analysis and sample calculations are described in [62] for reference.

CHAPTER 4

RESULTS AND DISCUSSION OF HIGH-SPATIAL-RESOLUTION MEASUREMENTS

Analysis of density and velocity fields calculated from large ensembles of high resolution measurements enables various insights into the development of the shock-driven instability. Analysis of the density fields leads to insights into the mixing, the velocity fields describe the dynamics of the flow, and the combination of simultaneous results demonstrates the coupled dynamics of mixing and yields important cross-statistics and insights into the turbulent state of the flow.

4.1 Flow Field Evolution and Mixing Analysis

The development of RMI can first be analyzed through flow visualization techniques to provide a good description of the morphology. Furthermore, analysis of scales such as the mixing width shed light on the progress of the overall instability growth, while other mixing quantities can describe how far mixing has progressed or how active the mixing is. Structures in the flow provide further description of the state of the flow and regional mixing characteristics.

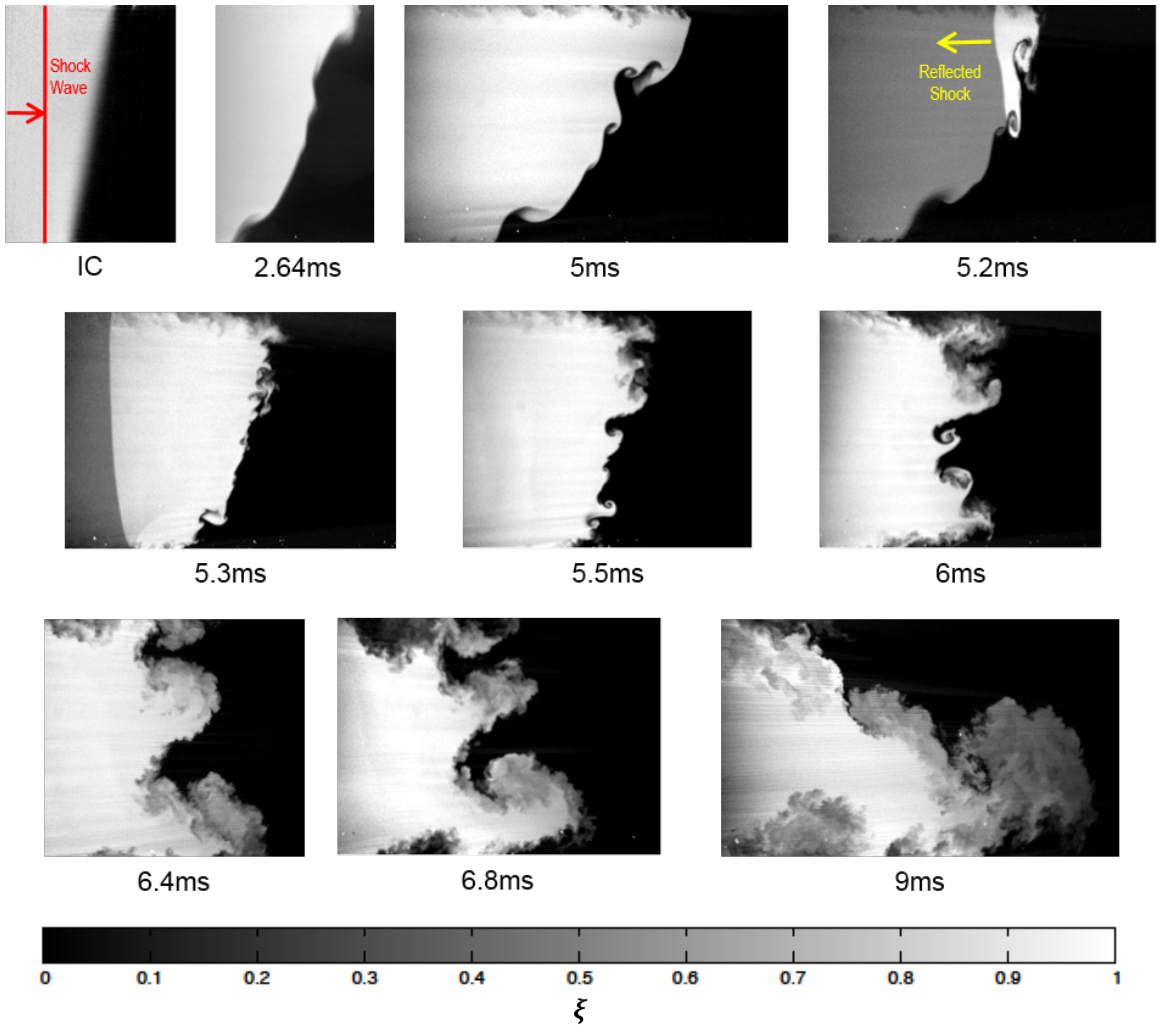

Figure 4.1: Concentration field evolution of $At = 0.22$ interface from the single mode initial condition. The experimental times are shown.

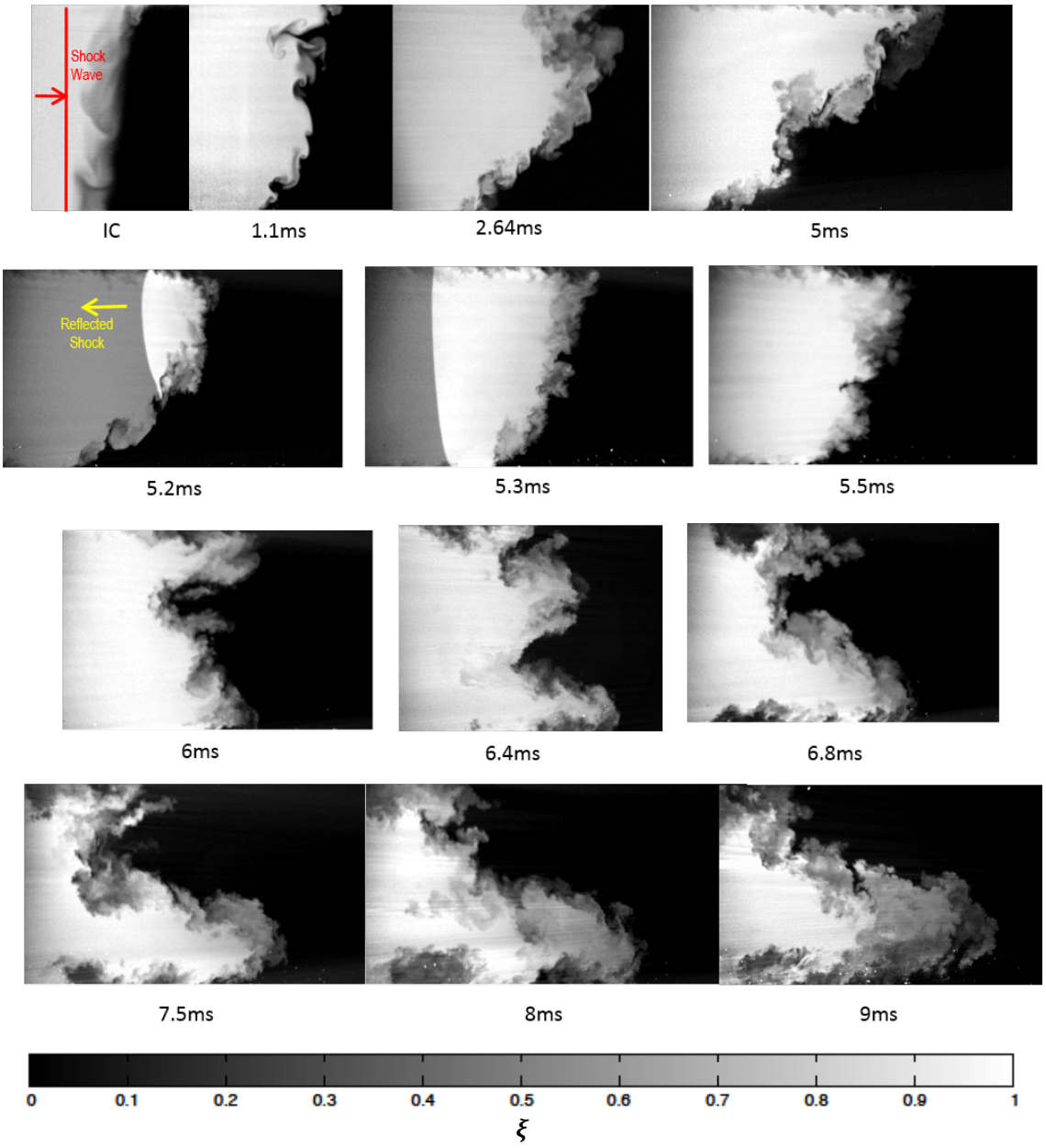

Figure 4.2: Concentration field evolution of $At = 0.22$ interface from the multi-mode initial condition. The experimental times are shown.

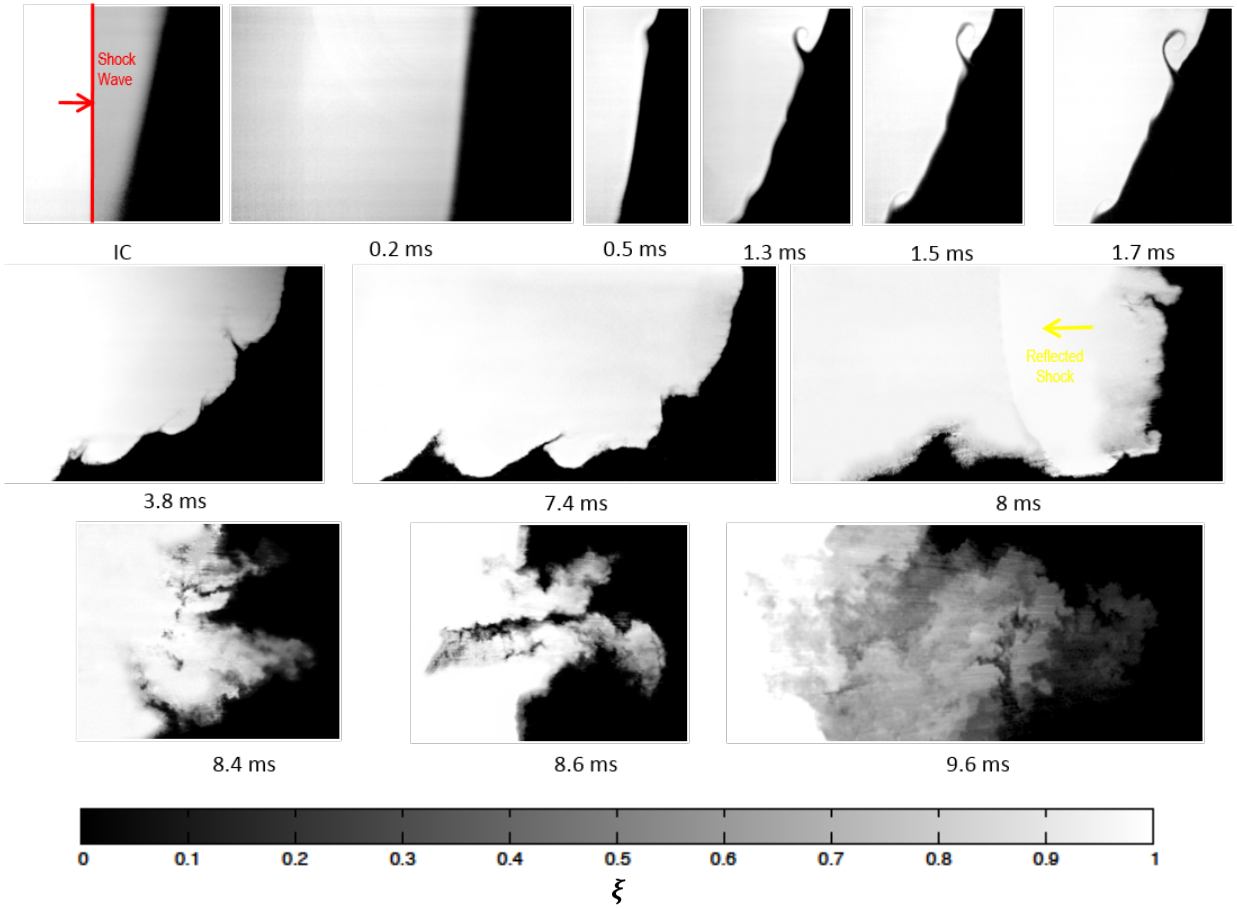

Figure 4.3: Concentration field evolution of $At = 0.67$ interface from the single mode initial condition. The experimental times are shown.

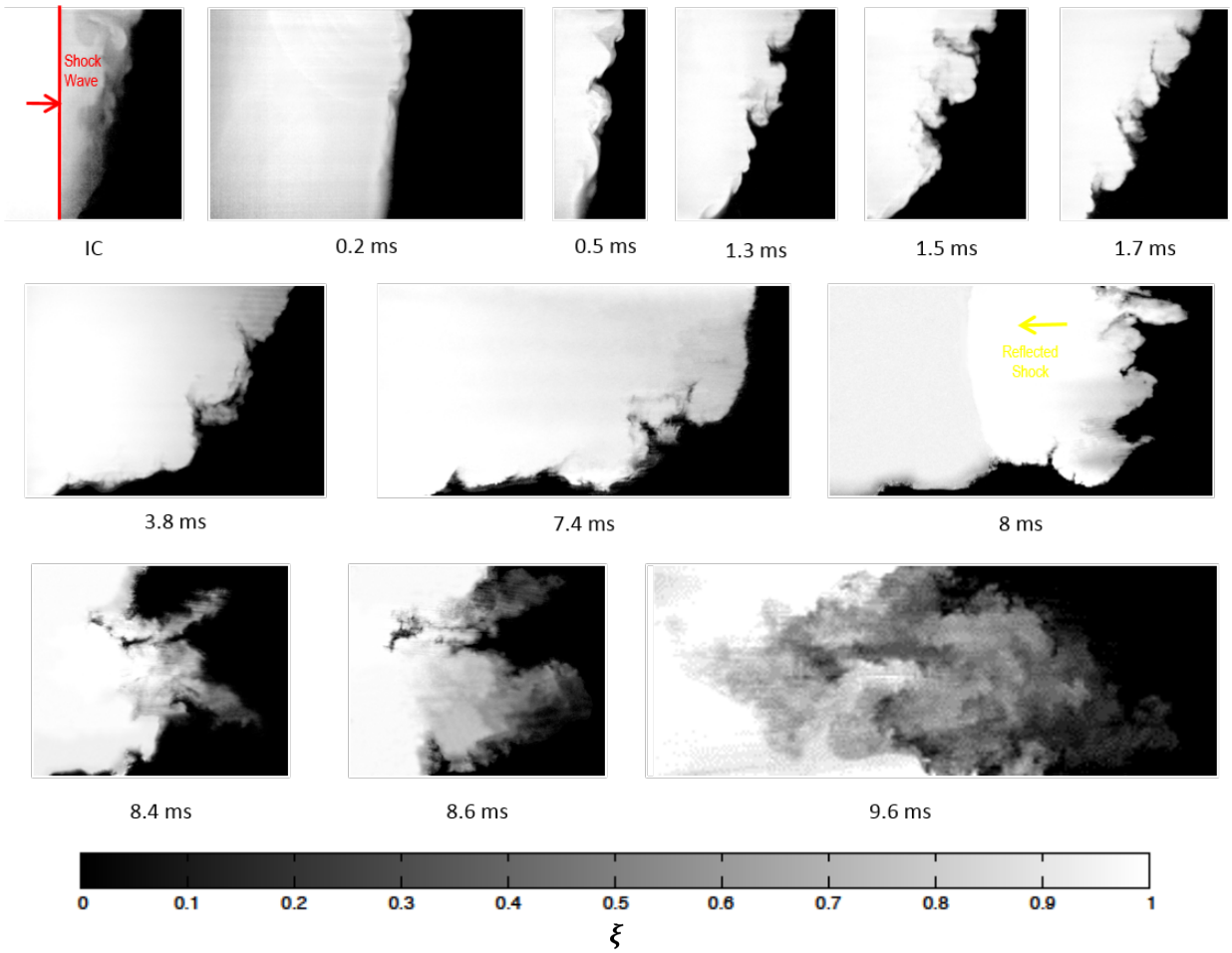

Figure 4.4: Concentration field evolution of $At = 0.67$ interface from the Multi-mode initial condition. The experimental times are shown.

4.1.1 Qualitative Analysis of Evolution of Density Fields

It is first valuable to visualize the entire flow development for each Atwood number through an image sequence. These high resolution images, shown in Figures 4.1, 4.2, 4.3, and 4.4, are not from the same experiment. Although they are not connected in time, these sequences are valuable to realize the continuity that is present in larger scales and mixing trends, illustrating the prominent effects of memory of initial conditions in shock-driven instability flows. They are also helpful in breaking down the development and analysing the differences between the cases. Thus, the analysis of the sequences in Figures 4.1, 4.2, 4.3, and 4.4 provides a thorough qualitative description of the instability arising from each Atwood number and initial interface.

Figure 4.1 shows the evolution sequence of the single mode interface for $At = 0.22$, and Figure 4.2 is for the multi-mode. To first give an overview, the images in the evolution sequences are shown such that the shock propagates from left to right, and experimental times are shown below each image. The first image shows the direction of shock travel (the actual shock is not shown). The interface begins to grow, then in the next few images the shock which has reflected off the end wall of the shock tube, or the reshock, propagates from right to left and interacts with the interface at approximately 5.2 ms. This is also highlighted with a yellow arrow. The shock appears as a sharp intensity contrast in the light fluid, as the gas behind the shock is more compressed.

When the incident (first) shock interacts with the interface, the shock compresses the gases, and the interface is sharpened. Following shock interaction, the amplitude of the perturbation begins to grow. The induced stretching of the interface results in further sharpening of the gradient between the two gases. The increased contact between the gasses and the intensified gradient result in increased diffusion, although it is obvious that the sharpening mechanisms are dominant over the slower process of diffusion at this point. This is generally true for both cases, but the multi-mode case has a much more

complex interface, and has more mixed material even before reshock as the additional small perturbations grow and interpenetrate across the interface. The shear between the two gases, which is well described by the baroclinic torque (Equation 1.2), is evident as rollup features begin to emerge. This is especially evident in the single mode case where the structures are very coherent and clearly emerge from the flat interface as same-signed vorticity begins to bunch up along the interface. The differences between the two cases are apparent at the later times before reshock.

The reshock wave interacts with a complex interface in both cases. This initial condition for reshock is seen at 5 ms. Although both cases are multi-modal before reshock, there is a difference in the content and distribution of scales, as the multimode case has many smaller features, increased diffusion, and an overall wider distribution of scales, while the single mode case is typified by more coherent larger features. Upon reshock, the interface is compressed again, yielding sharper density gradients, and baroclinic torque is deposited over a wider range of features and scales in both cases. Immediately after reshock the entire interface begins to overturn because the sign of the pressure gradient is now opposite of the incident shock. This constitutes a phase inversion for the inclined interface. The large-scale overturning motion is very similar for both single- and multi-mode cases because the long wavelength inclined perturbation is the dominant feature in this motion. The additional small features are observed to begin to grow after reshock as well. Inversion takes place on the smaller scales as well, but further interactions of features lead to a more complex flow. The vorticity in the single mode case is largely deposited with the same sign, leading to many corotating vorticies, while the vorticity is deposited in a more incoherent pattern in the multi-modal case. The features in the single mode case are predominantly corotating due to the dominance of positive vorticity in this case after reshock. Due to this, some of these rotating features merge and lead to larger structures which protrude out into the mixing region. These features then break down

and become mixed material in the core of the flow. This process is apparently slightly different in the multimodal case. Due to incoherency in the deposited vorticity, large features and same signed vorticity is not a dominant mechanism in the development. Many small features evolve and break down leading to mixed material, and the large wavelength eventually grows and penetrates between the two gases.

Figures 4.3 and 4.4 show the $At = 0.67$ development from the single and multi-mode experiments respectively. The IC (initial condition) for the single and multi-mode cases are visually identical to the corresponding $At = 0.22$ experiments. This was intentional, in order to maintain as many parameters consistent between test cases so that the Atwood number differences could be highlighted. Many major features of the development are also the same as the lower Atwood cases. The initial shock compresses the interface, the amplitude grows, reshock compresses the interface again, the interface overturns, and growth recommences with markedly increased mixing.

There are some differences between the Atwood numbers that are notable, including how the addition of modes to the initial condition affects the development. One thing which can be noticed early in the development, is that although the multi-mode interfaces are similar, the post initial shock interfaces seem different between the Atwood numbers. Although the initial conditions are almost identical, there is a higher degree of compression in the $At = 0.67$ case (about 3 times compression vs. about 2 in the low Atwood number case, as seen in Table 2.1). Further, while the difference between single and multi-mode interfaces manifests as quickly growing small-wavelength perturbations in the low At experiments, these features are less present in the higher At experiments. In addition to the compression due to a higher acoustic impedance mismatch, a factor that contributes to this is the rapid growth of the long-wavelength inclined perturbation; the high rate of stretching 'damps' the additional perturbations, resulting in the formation of features without extensive mixed material. Therefore, there are significant differences

between single and multi with both gas pairs, and additional features are found in the multi-mode case of each but increased mixing is more notable for the low At case than the high At case. Perhaps the most notable difference between the low and high Atwood numbers is the bubble-spike asymmetry which is prominent in the high Atwood case associated with the difference in dynamics between the two gases, a phenomenon which marks flows where there is a higher density contrast.

Due to the prior development, the initial condition for reshock is multimodal in both the single and multi-mode cases. As in the low At cases, the interface is recompressed and overturns. This results in the mixing region being confined to a smaller region while the phase inverts, then a spreading as it continues to grow. Due to the high degree of similarity between the single and multi cases before reshock, the sequences after reshock are very similar. One thing which can be noted is that there are a larger number of regions of locally high density in the multi-mode case than in the single mode case, where some of the multi-mode features have been separated from the interface, but have not been fully mixed, and remain in the core of the flow.

4.1.2 Mixing Width

With an understanding of how the interface develops qualitatively, the amplitude of the overall perturbation is also of interest for quantitative analysis. This is generally important, because it is the extent to which the fluids have penetrated into each other. This is important in many of the applications mentioned; it is also a typical way of characterizing instability growth as the large lengthscale of the flow and is good for comparative analysis. The amplitude width of the mixing region, or mixing width (η), is defined by the streamwise extents of the region of 5% to 95% concentration of light gas. The mixing width depends on the gas pair, the shock strength, and the misalignment between the shock and interface (pressure and density gradients).

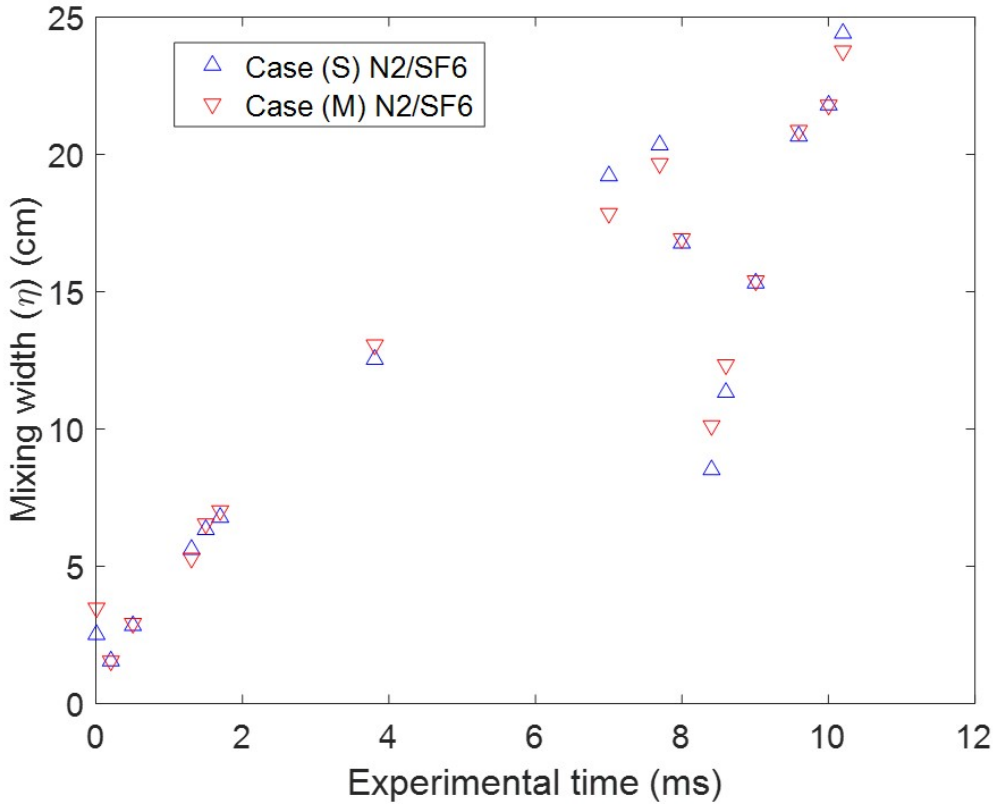

Figure 4.5: Amplitude mixed width from 5-95% definition for $At = 0.67$, N2/SF6 from the single mode (S) and multi-mode (M) initial conditions against experimental time.

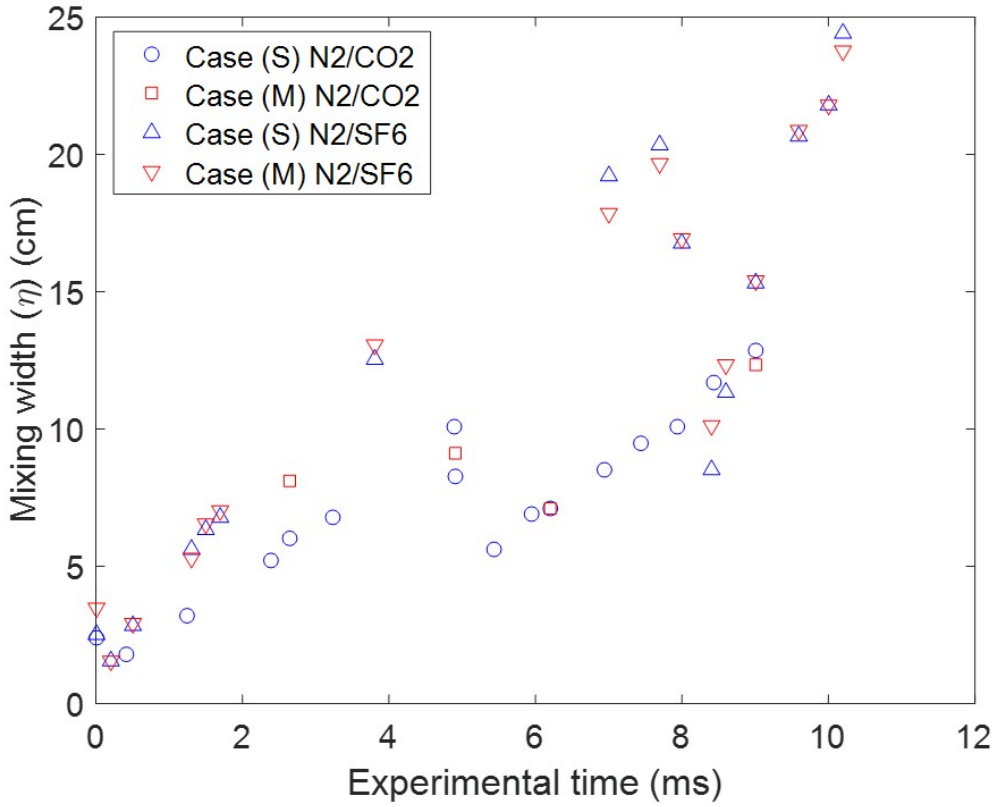

Figure 4.6: Amplitude mixed width from 5-95% definition for both $At = 0.22$, N2/CO2 and $At = 0.67$, N2/SF6 from the single mode (S) and multi-mode (M) initial conditions against experimental time.

Figure 4.5 shows the amplitude mixed width evolution of the $At = 0.67$ case from single and multi-mode initial interface profiles. The main features of the growth can be noted first. It is obvious that there is little difference between the single and multi-mode cases. This highlights that the overall amplitude mixed width is majorly dependent on the long wavelength inclined perturbation. In the early development, between the first few data points, the compression of the interface by the incident shock is observed as the amplitude initially decreases. Then rapid growth ensues with an initially linear trend.

Reshock compresses the interface again, as well as initiates the overturning, which is observed as a minimum near 8 ms in the graph. Once the overturning is complete, the interface grows more rapidly than before reshock. This is an indication of the kinetic energy imparted to the interface by the reshock wave, in the form of a velocity disparity in the flow. This is due to the high amplitude-to-wavelength ratio. Mixed width amplitude has been shown to converge in ~ 1 run for perturbations similar in the long wavelength such as these where IC variations are negligible. Any experimental error in the measurement is less than 1% according to the error in the PLIF images themselves and the integral nature of the measurement.

To compare the growth of the interface between the two Atwood numbers, Figure 4.6 shows the growth of both. Additional discussion of the $At = 0.22$ case can be found in [62]; comparison is the focus of the current work. There is a difference in the arrival time of reshock between the two Atwood numbers. This is because the shock travels slower through Sulfur Hexafluoride. The reshock arrives at about 5 ms in the low At case (N2/CO2), and arrives at about 8 ms in the high At case (N2/SF6). Again, this is observable as when amplitude suddenly decreases, then begins to increase again. The next thing which is notable, is that there is a significant difference in the growth rates between the Atwood cases, although the signature of the long wavelength dominates each case. This is especially true after reshock. Furthermore, there is a greater increase in

growth rate after reshock for the high At case than the low At case.

4.1.3 Models for Mixing Width

Similar to other instability-driven flows, understanding and modeling the amplitude growth of the perturbation, or mixing width has been a topic of much interest, because this is a major characteristic of the flow. This endeavor has been approached in several ways from linear analysis to empirical fits. If the amplitude of the perturbation is much smaller than its wavelength, linear analysis is reasonably valid. However, when the perturbation grows to be approximately the same as the wavelength, nonlinearities begin to affect growth as secondary instabilities, shear, and vortical motions are more prevalent. Multi-mode interfaces present a challenge as they are not simply a sinusoidal waveform. These have been thought of as either the sum of several waveforms, or using a dominant mode.

The Rayleigh–Taylor Instability (RTI) was studied from linear theory by Taylor [11], and later extended by Richtmyer. For a sufficiently weak shock, Richtmyer imposed assumptions that the flow is incompressible, and substituted an impulsive acceleration for gravity in the RTI analysis [9] which resulted in the expression for growth rate:

$$\dot{\eta} = kV_0A\eta_0' \tag{4.1}$$

where V_0 is the jump velocity when the shock interacts with the interface, $\eta_0' = \eta_0(1 - \frac{V_0}{w_i})$ is the amplitude at $t = 0$ ms, and w_i is velocity of the incident shock. Thus the shock strength and misalignment are considered, and impedance mismatch is a factor in $\frac{V_0}{w_i}$. Thus, when $k\eta < 1$, and linear analysis is valid, the growth estimated by the Richtmyer model is approximately linear. Efforts have also been made to model the interface when the nonlinear effects are significant, typically through series expansions which are truncated, which have been improved throughout the years [92, 93]. Recently, Sadot et al. furthered the attempt to model growth from early onset through the late

nonlinear growth [94]. The model is given as

$$v_{b/s} = \frac{v_0(1+v_0kt)}{1+(1\pm A)v_0kt+[(1\pm A)/(1+A)]v_0^2k^2t^2}. \tag{4.2}$$

where the ($\pm$), plus minus, applies to bubbles or spikes respectively so that $v = \frac{v_b+v_s}{2}$. From integration of this [64], the amplitude of the bubbles and spikes are, respectively:

$$h_b = \frac{1}{2k}\left[log((A+1)\tau+\tau^2+1) - \frac{2(A-1)tan^{-1}[\frac{A+2\tau+1}{\sqrt{-A^2-2A+3}}]}{\sqrt{-A^2-2A+3}}\right], \tag{4.3}$$

$$\begin{aligned} h_s = \frac{1}{2k}(A+1)\Bigg[&- \frac{log(-A^2\tau-A\tau^2+A+\tau^2+\tau+1)}{A-1} \\ &+ \frac{2\sqrt{A-1}tan^{-1}[\frac{\sqrt{A-1}(A+2\tau+1)}{\sqrt{-A^3-A^2-3A-3}}]}{\sqrt{-A^3-A^2-3A-3}}\Bigg], \end{aligned} \tag{4.4}$$

where, $\tau = kv_0t$, (similar to nondimensional time, τ_i and τ_r).

The instability growth has also been modeled after reshock, when in many cases a phase inversion must be accounted for, and nonlinear effects are influential sooner than after the initial shock. As in the current case, the interface can also be more complex upon reshock.

Mikaelian modeled the early reshock growth [95]. This is given as

$$\dot{h}_{rs} = C_M A \triangle u, \tag{4.5}$$

where C_M is in the range 0.28-0.34, and in the current work, about 0.28. $\triangle u$ and A are jump velocity and Atwood number after reshock.

To account for reshock interaction with a turbulent mixing layer, the interface has been modeled as diffuse by [61]. This is given as

$$\dot{h}_{diff} = C' A^2 g(A) \Delta u \tag{4.6}$$

where $\triangle u$ and A are jump velocity and Atwood number after reshock, and

$$g(A) = \frac{1}{A^2}\left[1 - \frac{1-A^2}{2A} log\left(\frac{1+A}{1-A}\right)\right]. \tag{4.7}$$

An empirical model was also developed by [61] for a reshocked mixing layer. The model is given as

$$\dot{h}_{emp} = 0.40(-\Delta u/\hat{c})^{-0.56} A^{1.96}(-\Delta u) \tag{4.8}$$

where $\hat{c}$ is the density-weighted average speed of sound.

In order to compare the two Atwood numbers, it is important to bring the two cases to similarity. This is done by using the growth of the amplitude as a characteristic of the interface, and thus a metric of the maturity of the interface. Thus the interface's amplitude and the time are both dimensionless or nondimensional. This provides similarity at any point in dimensionless time (τ), even though growth occurs at different rates in real, experimental time. Then at the same state of maturity according to this characteristic, various differences in other facets of the interface can be discussed where comparison is warranted.

The specific method of nondimensionalization used herein is described in [54] and [96]. The dimensionless time after incident shock, and before reshock is given as

$$\tau_i = k\dot{h}_0(t - t^*). \tag{4.9}$$

where $\dot{h}_0$ is the initial growth rate after incident shock, and t^* is the time required for the shock wave to traverse the inclined interface. Likewise, the dimensionless time after reshock is

$$\tau_r = k\dot{h}'_0(t - t'^*), \tag{4.10}$$

where $\dot{h}'_0$ m/s is the mixing width growth rate after reshock, $t'^* = \frac{h_{(pre-reshock)}}{w_r}$ is the time it takes the reshock wave to traverse the interface, and $t = t_{exp} - t_{(reshock-interface-interaction)}$, where t_{exp} is the actual experimental time (i.e. t here starts upon reshock, and τ_r is zero when the reshock completes traversal of the interface).

The dimensionless mixed width plotted against dimensionless time before reshock is shown in Figure 4.7. The single mode and multi-mode cases are shown as shapes, and models are shown as lines. Because of the rapid growth of the high At, and the slower speed of the reshock wave in SF_6, the High At case progresses to a much later nondimensional time, and displays a stronger nonlinear trend at later times. The thick dark line corresponds to Richtmyer's model and agrees very well until nondimensional time reaches about two. The lighter solid line (blue online) corresponds to Sadot's model ($h = \frac{h_b + h_s}{2}$) for the low At experiments and the dashed line (red) corresponds to Sadot's model applied to the high At experiments. This shows how the model varies with Atwood number. The early divergence of the low At calculation seems less than ideal, but still shows reasonable agreement. However, the calculation for high At shows a near-linear trend for a longer nondimensional time and demonstrates quite good agreement with experimental results until late times for the high At calculation, for which reasonable agreement is still observed. Good agreement was also observed for the model upon comparison with experiments (their own and external experiments) encompassing a few initial wavelengths, Atwood numbers, and mach numbers presented in the work of [94].

The dimensionless mixed width following reshock is shown in Figure 4.8. The experiments are shown as shapes and the models are shown as lines. The reshock model of Mikaelian [95] is shown as a dark line (same result for both At using this nondimensionalization scheme). The models of the low Atwood case are shown as solid lines and the models of the high Atwood case are shown as dashed lines.

The Mikaelian model fits the low Atwood case very well, and agrees with the high

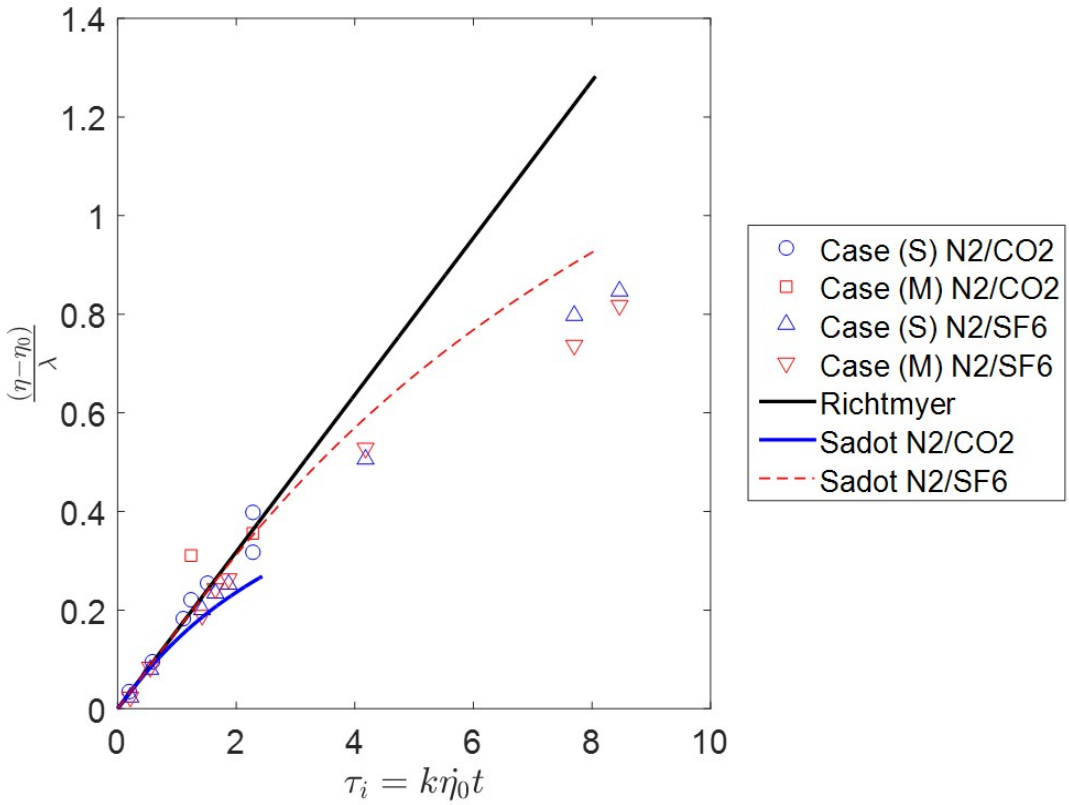

Figure 4.7: Nondimensional amplitude mixed width from 5-95% definition for both $At = 0.22$, N2/CO2 and $At = 0.67$, N2/SF6 from the single mode (S) and multi-mode (M) initial conditions against nondimensional time before reshock.

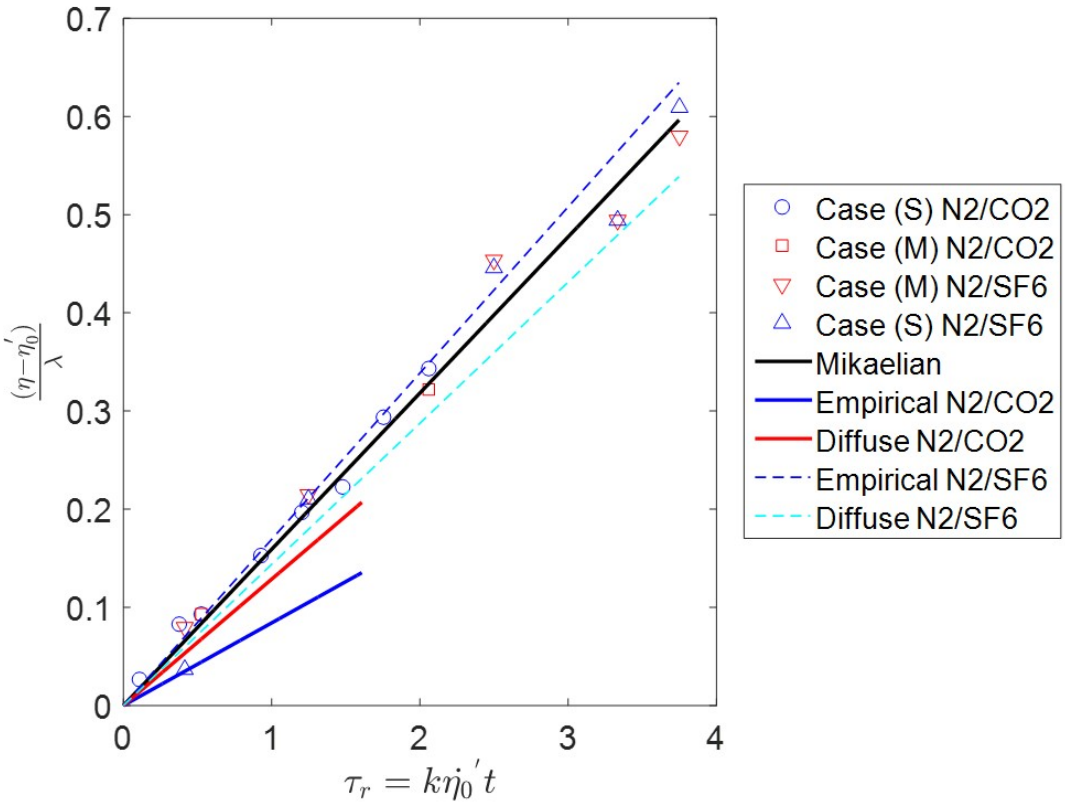

Figure 4.8: Nondimensional amplitude mixed width from 5-95% definition for both $At = 0.22$, N2/CO2 and $At = 0.67$, N2/SF6 from the single mode (S) and multi-mode (M) initial conditions against nondimensional time after reshock.

Atwood case even until later nondimensional times after reshock. Both the empirical and diffuse models of Lombardini [61] show an increase in growth rate with increasing Atwood number, but the empirical model shows a higher sensitivity to Atwood number. While the empirical and diffuse models both agree with the Mikaelian model reasonably at higher Atwood number, the Diffuse model is closer at low Atwood number, but not the empirical model, which also corresponds to the degree of agreement with the experimental data. Similar trends can be seen in the numerical study for these models [61]. It is worth noting that the Mach number study of Mohaghar et al. also saw excellent agreement and good collapse of the data with the model of Mikaelian with changing Mach number [63].

4.1.4 Mixing Layer Thickness

Mixing layer thickness, δ, is the average streamwise thickness of the mixed material in the range $4X_{light}X_{heavy} > 0.84$ (sometmes referred to as the inner mixing region, where material is significantly mixed). Here, Y_{light} and Y_{heavy} are the mole fraction of the light and heavy gases respectively at each spanwise location. For this region, δ is calculated as

$$\delta = \frac{\int\int 4X_{light}X_{heavy}dxdy}{\int dy}. \tag{4.11}$$

Figure 4.9 shows Mixing layer thickness for the single mode and multi-mode initial conditions before reshock. There is not a significant difference between the initial conditions for this parameter before reshock with values centered around approximately 1 cm, with variations in the small amount of very mixed material possibly due to the small size of the Batchelor scale, and the approximate error is likely on the order of 0.5 cm. The multi-mode case could possibly display a higher mixing layer thickness at later times due to additional features which are more developed and have broken down to smaller scales. Both cases display small mixing layer thickness throughout the prereshock development,

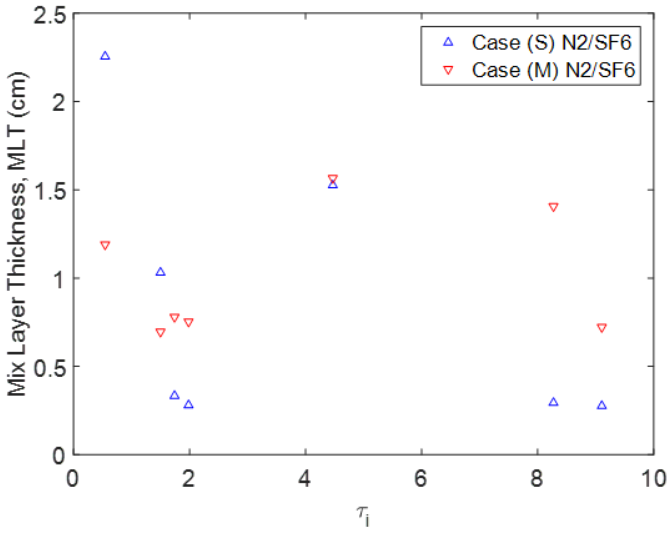

Figure 4.9: Mixing layer Thickness for the single mode (S) and multi-mode (M) initial conditions against nondimensional time before reshock.

characteristic of the sharp interface of the high Atwood number case. Both cases also display little growth, because the rate of diffusion is quite low without more violent stirring motions at more length scales, as observed after reshock. However, the entrainment was observed to increase rapidly during the time before reshock.

Figure 4.10 shows Mixing layer thickness for the single mode and multi-mode initial conditions after reshock (τ_r). The mixing layer thickess is observed to increase steadily for both cases. Similar to before reshock, the mixing layer thickness contains some error because of the small regions which must be captured. Thus there is more variability at earlier times whenthe values are smaller; however, at later times after reshock mixing layer thickness appears to converge well because there is considerably more mixed material, and the small diffusion layers are almost negligible. This error is not based on magnitude of the measurement, and is more of an absolute error due to the amount of very small diffusion surfaces. Therefore, the conservative estimate for error is about 0.5 cm, which is $\pm$ 10 % of the maximum value at late times.

It is not possible to determine exactly what events transpired between datapoints;

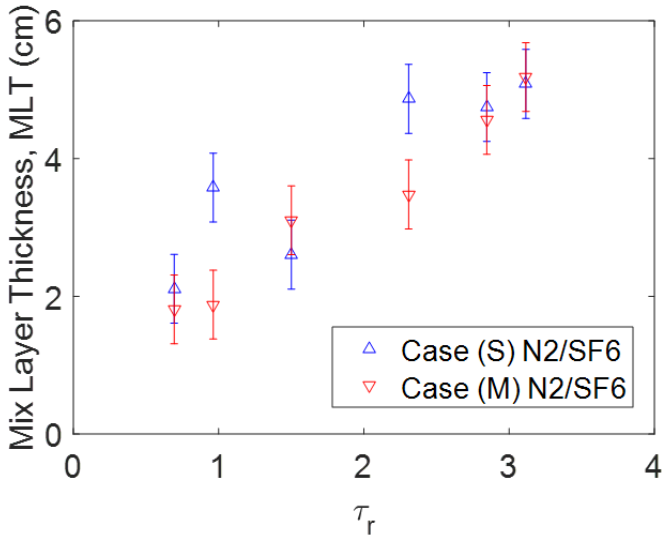

Figure 4.10: Mixing layer Thickness for the single mode (S) and multi-mode (M) initial conditions against nondimensional time after reshock.

the points are not connected in time. Therefore it is valuable to eventually consider the amount of mixing from a temporally resolved dataset. This will be explored in this work, and expansion is recommended as future work. The steady increase is to be expected and is the same trend observed by Mohaghar et al. for both Mach 1.55 and Mach 1.9 experiments [63]. However, the high Atwood number case eventually reaches a higher value of mixing layer thickness at late times after reshock, although a later nondimensional time after reshock is achieved in the current work. This increase should be considered along with the aforementioned mixing width which denotes entrainment, primarily, and mixedness in Section 4.1.5, where the relationship between these features of the flow are further explored through mixedness, a quantity which compares them to describe the level of homogeneity in the flow.

4.1.5 Mixedness

Mixedness profiles are a measure of what proportion of fluid which is entrained is also molecularly mixed, the limits of which are complete separation of species (imiscible), and

a state in which the species are fully mixed in the same proportions as they are present, ie., no inhomogeneity. The integral Mixedness for the mixing layer, θ, which can be found by averaging profiles over the mixing region, is calculated as

$$\theta = \frac{\int \overline{X(1-X)}dy}{\int \overline{X}\,\overline{(1-X)}dy} \tag{4.12}$$

where heavy fluid has a mole fraction of

$$X = \frac{\rho - \rho_1}{\rho_2 - \rho_1}. \tag{4.13}$$

Figure 4.11 shows mixedness for the multi-mode case and single mode case before reshock. The trend exhibited for the mixedness in the two initial conditions is similar, but the multi-mode initial condition exhibits a slightly larger degree of mixedness than the single mode case. Some of the more complex features produce a greater amount of mixed material compared to the amount of entrained material, which is very similar for the two initial conditions (4.6) thus resulting in a slightly larger ultimate mixedness. Another notable feature of both initial conditions is the sudden decrease right after incident shock which corresponds to the rapid growth of the interface amplitude, while molecular mixing has yet to become very large. This is followed by a relatively stable mixedness value, which denotes that the amplitude growth rate, the extents of the entrainment of fluid is pacing the molecular mixing.

Figure 4.12 shows the mixedness vs nondimensional time after reshock, the mixedness values for the two initial conditions are similar, with a final steady value of mixedness being achieved late after reshock near 0.7 for both cases. A similar trend and asymptotic value from ILES of $At = 0.5$ RMI with multi-mode initial perturbation, much like the current interface upon reshock, was found by Thornber and Zhou [97]. Later, Zhou et al. also found a similar trend with asymptotic value of about $\theta = 0.81$ and 0.71 for

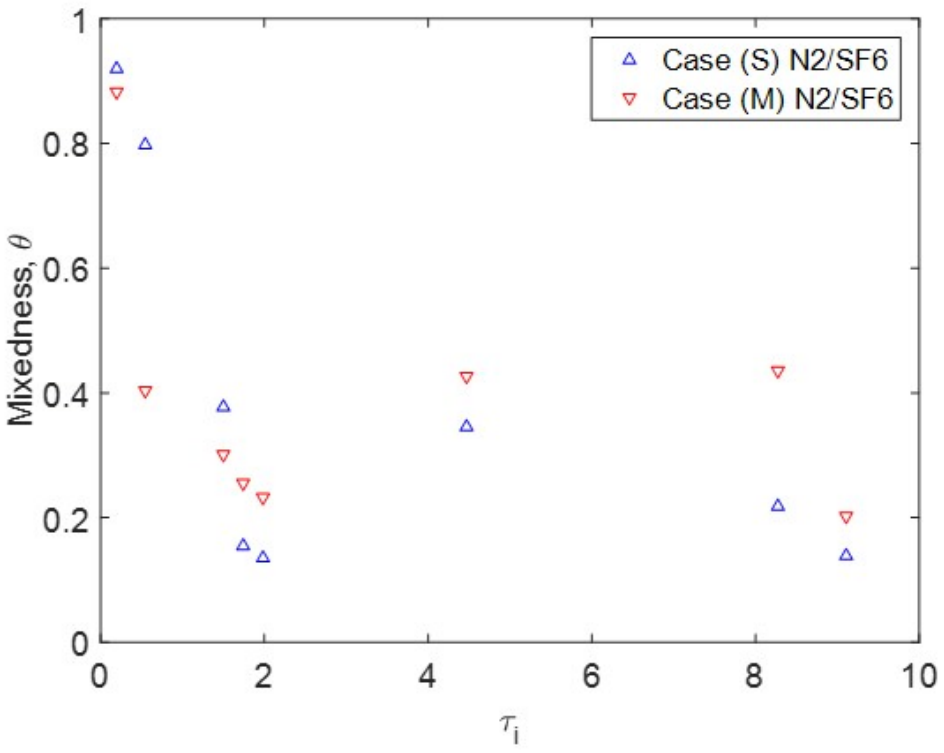

Figure 4.11: Mixedness against nondimensional time before reshock.

Atwood numbers of $A = 0.5$ and 0.8 respectively, and noted that the result for RTI flows was 0.78 regardless of Atwood number [98]. The current work displays very similar asymptotic behavior. Regarding the implications of error analysis, mixedness is slightly more variable at early times after reshock due to the overturning phenomenon which occurs because the shock travels from heavy to light gas depositing positive baroclinic torque, causing variations in the amount of entrainment. However, it converges well at late times where more breakdown of scales has occurred. Furthermore, for example, the sample of 97 runs resulted in a standard deviation of 0.02, or about 3%. However, due to the limited number of times available with large ensembles a conservative error estimate is around 6% and is shown for all times, however the two early times are slightly less converged and should be considered as such. These results provide an inspiration for future work with larger ensembles of temporally resolved data in order to further define this asymptotic value. While the average of experimental runs seems to approach an asymptotic value. A result of the current analysis is a hypothesis which can be answered with larger sets of temporally resolved data: each individual experimental run approaches an asymptotic value, which may vary slightly due to initial conditions.

In consideration of low Atwood number results which display a slightly higher value of mixedness at late times [63], it is apparent that the larger momentum effects of the high Atwood number case play a role in the mixing dynamics as heavy fluid is carried deep into the light fluid, increasing entrainment and inhomogeneity more rapidly than in the low At case. Simply the rate of entrainment is higher in the high At case, as can be readily observed in the density fields.

The physical phenomenon described by the asymptotic state is that the rate at which new fluid is entrained and the rate at which it is mixed at smaller scales is similar, which follows from the asymptotic values found for both mixedness and scalar dissipation rate by Tritschler et al. [99]. Thus contained therein is also a description of the scales of

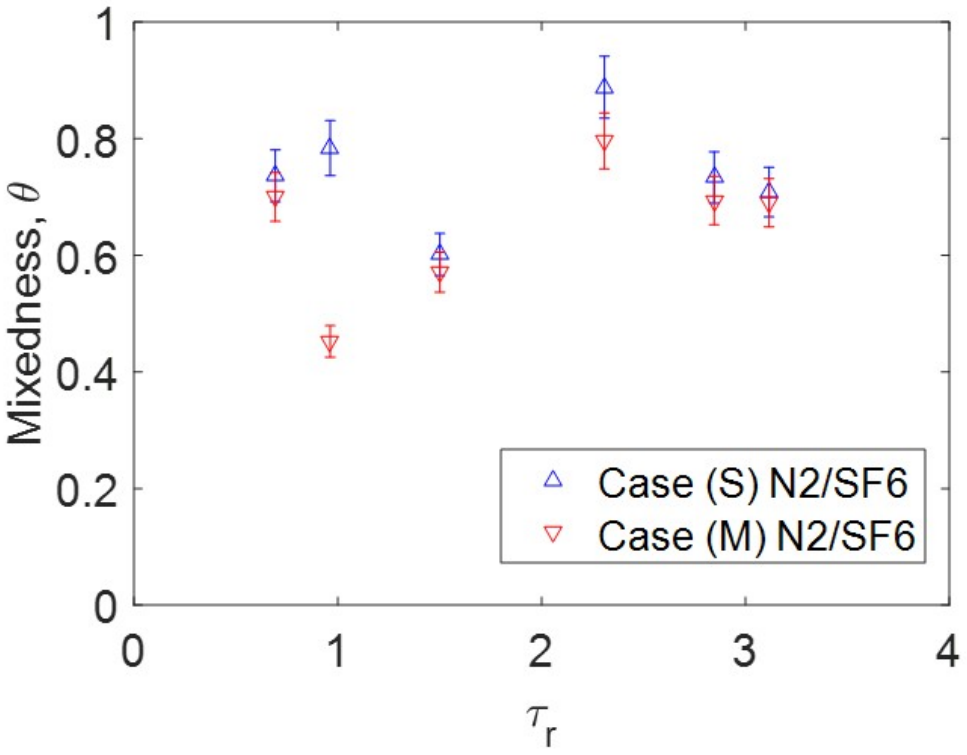

Figure 4.12: Mixedness against nondimensional time after reshock.

the flow. The large scale, driven by the large wavelength in the initial perturbation and the small scales are at this point connected by an inertial range, which will be explored in section 4.3.2. Thus in the relationship of the large scales to the medium and small scales lies the mechanism of this phenomenon, having some constant ratio as the large scale coasts and energy is removed from the flow at the smallest scales. Thus the scalar density field is connected to the velocity field. RMI, recall, has unsteady forcing of the large scale, with monotonic decay. Therefore, the conclusion is that the large scale motion decays in tandem with the small scale motions. Simply, in these flows, the large scale is the forcing for the kinetic energy of the mixing region; the entrainment drives the motions which cause molecular mixing.

Lastly, an implication of the asymptotic value for mixedness in RMI flow is that the flow has self similarity in some aspects, described by the aforementioned parameters and others. Further understanding of this behavior, and the corresponding flow parameters will result in better schemes to describe time and length scales in the flow.

4.2 Turbulence Analysis

Turbulence is not yet fully understood, because of the chaotic nature of motions which occur on a broad range of scales. It is usually described statistically, at least on some scales of the flow, and eludes direct solutions, due to the random nature subject to variations caused by the smallest of disturbances. In many cases it is desired to statistically describe the flow. In this work, the flow is described statistically using joint velocity and density data. This leads to further understanding of how the density ratio affects these statistics and how that information is retained even after transition to turbulence.

4.2.1 Density Self-Correlation

The density-specific volume correlation, also referred to as the density self-correlation (DSC), is the correlation between density fluctuations and specific volume fluctuations. This statistic is a factor in closure of many turbulence models, connecting the turbulent fluctuations to the level or intensity of mixing. It was termed the b parameter in the Besnard, Harlow, and Raunzen (BHR) model [69]. It has been extensively investigated, and the field of instability-driven turbulence is beginning to understand its relevance to descriptions of real flows as well as simplified modeling of these flows. These works are valuable in understanding the present work's efforts, and should be referred to for perspective. Various facets of this parameter have been explored previously, particularly the effect of averaging method [68, 62, 63]. The DSC is evaluated as

$$b = -\langle \rho'(1/\rho)' \rangle \tag{4.14}$$

where angle brackets denote ensemble averaging, as opposed to an overbar which denotes spatial averaging.

In the Boussinesq limit, the DSC reduces to the density variance. Thus, this quantity has been simplified, based on the assumption that species is not important to the flow physics, relating to the momentum terms of NS equations. The approximation utilizing density variance is given by

$$b_{approx} = \langle \rho'^2 \rangle / \langle \rho \rangle^2 \tag{4.15}$$

This is critical to understanding the meaning and utility of the variable. This concept is similar to the better known concept of Favre-averaged Reynolds stress and velocity variance, which describe the turbulence intensity. Thus, this variable describes the mixing intensity. That is, the current level of active mixing due to turbulent fluctuations. This is

not to be confused with mixedness, or how much of the entrained fluid has mixed already (not "is mixing", but "has mixed"), which is inversely proportional to the DSC from spatial averages, which describe a spatial characteristic of the flow, namely the homogeneity or inhomogeneity, respectively. Essentially, the DSC calculated from spanwise averages is a description of spatial inhomogeneity, and is tied to the turbulent fluctuations with dependence on the flow characteristics such as isotropy and homogeneity [100]. To summarize previous discussions about the parameter in regards to this averaging, the DSC from spatial averaging is not like typical turbulence descriptors, but simply a description of inhomogeneity, and is inversely proportional to mixedness, and thus provides no additional information about the state of the flow [69, 68, 62, 63, 64]. Therefore, the current work calculates mixedness as a measure of inhomogeneity, and the DSC as a turbulence statistic, from ensemble averages to provide independent, additional information about the flow.

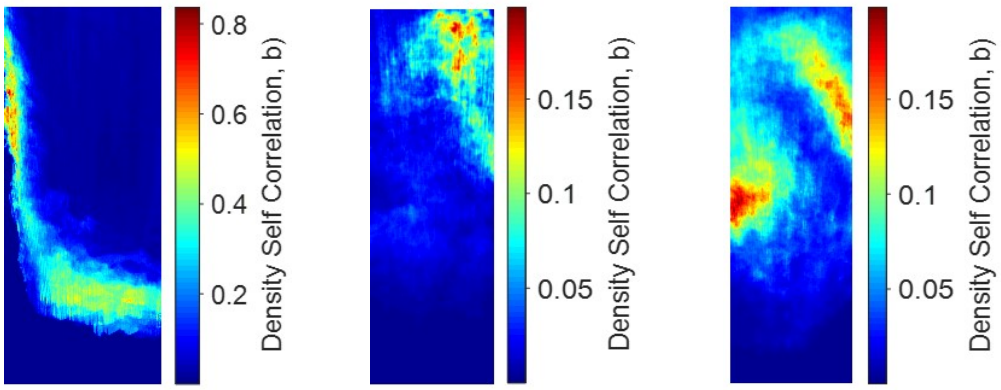

(a) Multi-mode $\tau_i = 8.46$ *(b)* Single mode $\tau_r = 2.1$ *(c)* Multi-mode $\tau_r = 2.1$

Figure 4.13: Density Self Correlation (DSC), or b parameter for the high Atwood case for (a) the multi-mode IC at $\tau_i = 8.46$ (b) the single mode IC at $\tau_r = 2.1$ and (c) the multi-mode IC at $\tau_r = 2.1$.

DSC fields can therefore be calculated because ensemble averaging is employed in this work. Figure 4.13 Shows the fields of the DSC, or b parameter, for the high Atwood

number case, comparing the latest times before and after reshock and the single and multi-mode cases after reshock. Figure 4.13a displays a much higher value for the DSC than either case after reshock. This should be noted because it shows the relationship between spatial inhomogeneity and turbulent mixing, in accordance with intense shear at the interface causing interpenetration of the gases. The spike demonstrates this with elevated values of DSC where the shear is highest.

After reshock, much lower values are observed overall due to homogenization which has resulted from the active mixing up to this time (time-integrated mixing, begets mixed material) in the evolution. Similar values are observed in the single and multi-mode cases in the spike region, but not in the bubble region. In the bubble region the multi-mode case indicates an elevated level of active mixing denoted by higher DSC values, in connection to the complex perturbations which cause additional small features along the interface which are driven into the bubble region by shear, separating and becoming inhomogeneities which are broken up by turbulent motions and provide the gradient for active mixing.

Figure 4.14 Shows the comparison between low and high Atwood numbers for the DSC. Note that the axes are different between the two cases, highlighting the large increase in the DSC with Atwood number. This is noteable, because the DSC is a nondimensional parameter. Although the statistic is calculated at the same nondimensional times, the values are much different, indicating a lack of scaling based on the current similarization scheme, which is primarily based on interface amplitude similarity. Wherein that in a state of interface similarity in the large wavelength perturbation, some statistics such as this do not achieve similarity.

Further, elevated values of the DSC before reshock are observed, and the effect of the geometery of the interface on the calculation of profiles is especially highlighted. There is a very high peak where the spanwise average used to calculate the profile as a function

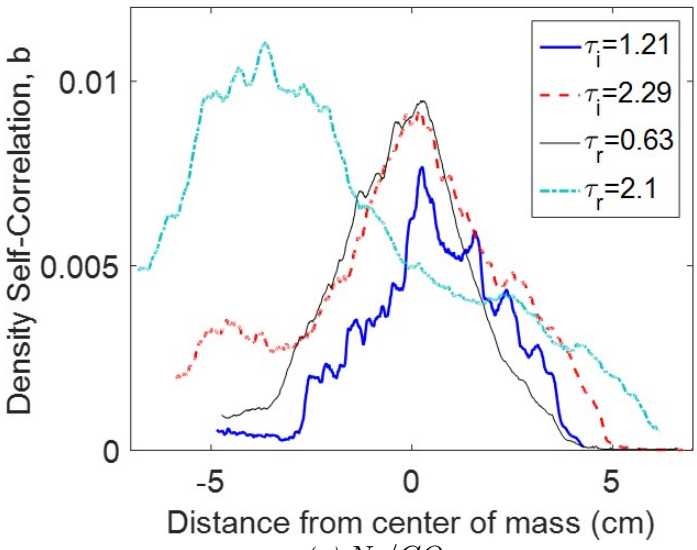

(a) N_2/CO_2

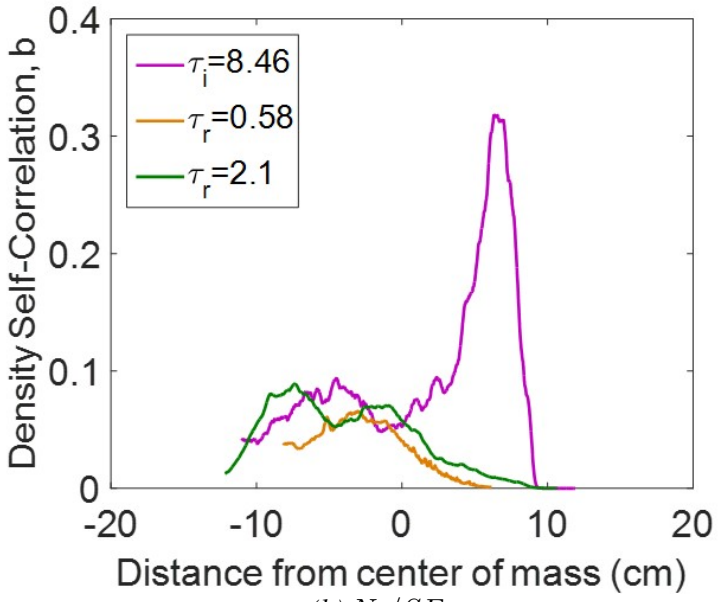

(b) N_2/SF_6

Figure 4.14: Density Self Correlation (DSC), or b parameter for the multi-mode initial condition (IC): (a) Low Atwood case. (b) High Atwood case.

of streamwise distance encompasses a cross region of primarily moderate to high-valued DSC, and very little of the region is low-valued, resulting in a large value for the average due to geometry and the nature of averaging over an inhomogenous region. At later times, after reshock, in regions which are more homogenous, the DSC is observed to be more well-distributed, with slightly higher values on the spike side.

To consider the validity of the Bousinnesq approximation at different Atwood numbers, the DSC is compared to its approximation, based on the assumption that the fluid momentum is independent of species for both Atwood numbers. In general the momentum terms will depend more on species a higher Atwood numbers. Figure 4.15 shows the density self correlation compared to its approximation as the first term of its Taylor series expansion for the low Atwood number case. There is a small difference between the DSC and its approximation, and it would be reasonable to use the approximation for conditions such as these with an Atwood number close to 0.22. These display that the bubble region has a higher level of active mixing in the multi-mode case than the single mode case.

To further consider the difference between the two Atwood number cases, the DSC and its approximation are also calculated for the high Atwood case; figure 4.16 shows the profiles of the DSC and its approximation for high Atwood number. In contrast, both cases show a higher degree of mismatch between the DSC and its approximation. A notable feature of both cases is the elevated level of active mixing in the bubble region. However, the Higher Atwod number case displays a more distinguishable difference between the initial conditions, highlighting the effect of Atwood number on initial condition dependency.

To take a closer look, Figure 4.17 shows the approximation divided by the DSC. It is observed that in certain regions of the flow, the approximation differs by around 20% from the DSC. This result is important when it is desired to employ this approximation to reduce computational costs. This also provides a useful insight into the flow dynamics;

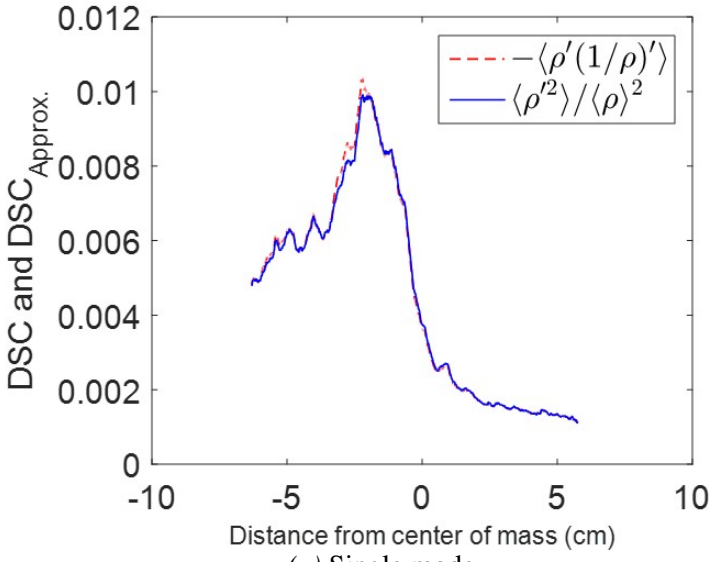

(a) Single mode

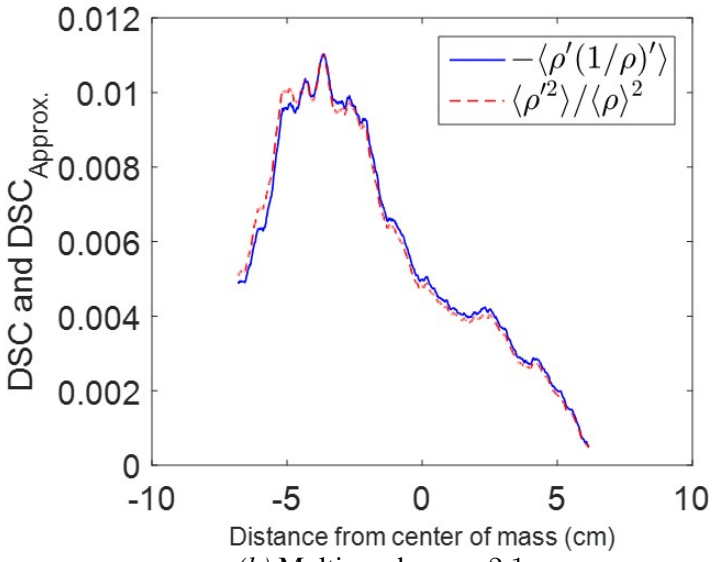

(b) Multi-mode $\tau_r = 2.1$

Figure 4.15: Density Self Correlation (DSC), or b parameter and its approximation at $\tau = 2.1$ for the low Atwood case for (a) the single mode IC and (b) the multi-mode IC.

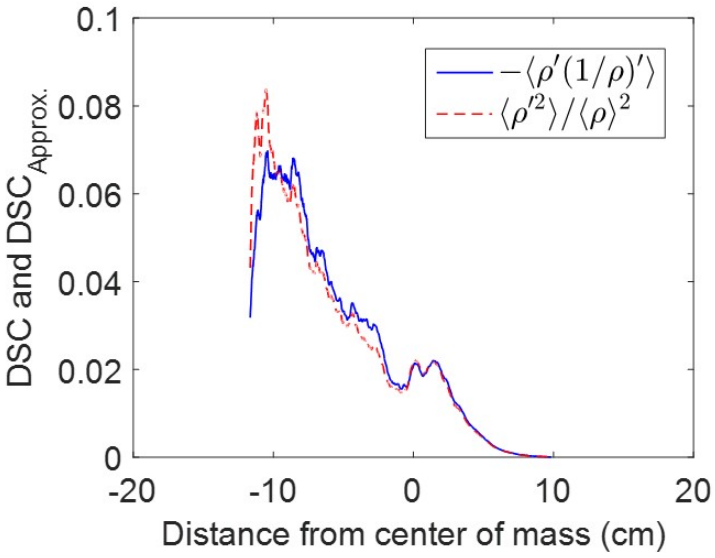

(a) Single mode

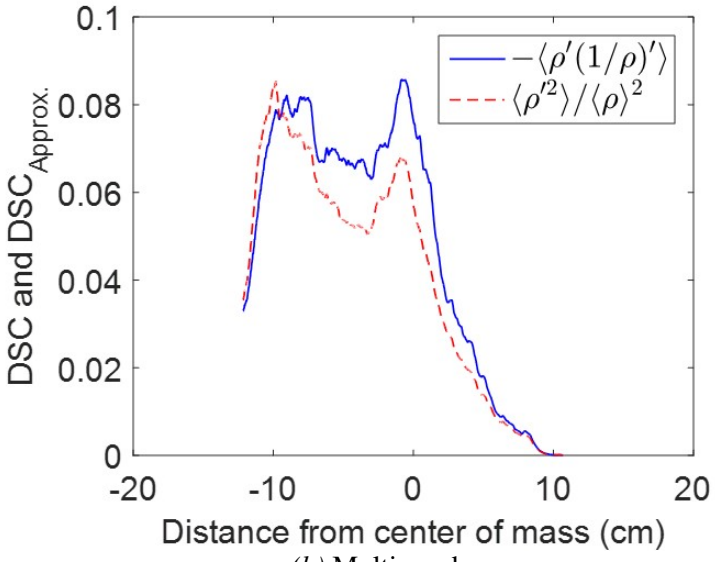

(b) Multi-mode

Figure 4.16: Density Self Correlation (DSC), or b parameter and its approximation at $\tau = 2.1$ for the high Atwood case for (a) the single mode IC and (b) the multi-mode IC.

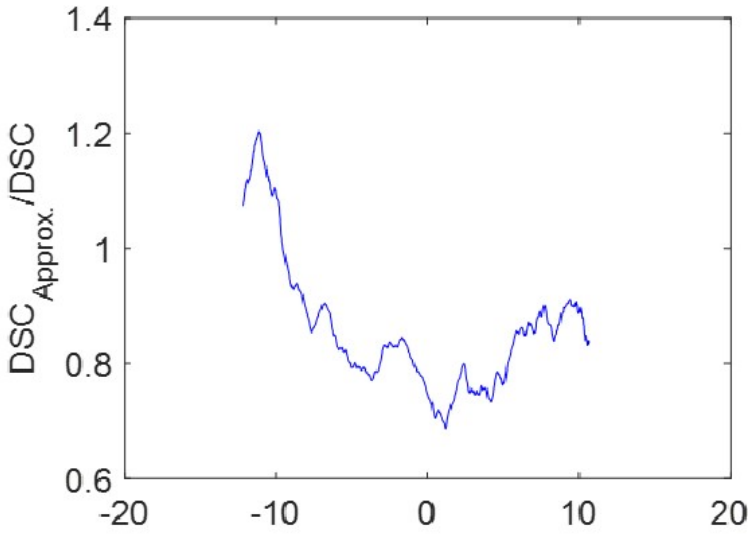

Figure 4.17: Comparison of the approximation of the DSC to the DSC for the multi-mode (M) initial condition at Late time after reshock, $\tau = 2.1$.

that the momentum of the heavy gas is relavant to flow dynamics, and the two fluids do not behave as similarly to each other as in a comparable low Atwood number flow. Thus species and momentum are truly coupled in this flow.

4.2.2 Turbulent Mass-Flux

The average velocity of the flux of mass due to turbulent motions is a valuable statistic in variable-density flows. This quantity is interconnected with both turbulent velocity fluctuations and density fluctuations associated with active mixing. The the selection of density fluctuations to velocity fluctuations drives the production of Reynolds stress. From the equations of motion for fluid flow, a popular model for the turbulent flow is the BHR model which utilizes Reynolds averaging of the Navier-Stokes equations. The production term of the Reynolds stress from the BHR model [101] is:

$$[a_i \overline{P}_{,j} + a_j \overline{P}_{,i}] - \overline{\rho}[\widetilde{R}_{ik}\widetilde{u}_{j,k} + \widetilde{R}_{jk}\widetilde{u}_{i,k}] \tag{4.16}$$

where a is the turbulent mass-flux velocity, given by

$$a(x,y)_i = \frac{\langle \rho' u_i' \rangle}{\langle \rho \rangle} \tag{4.17}$$

This highlights the role of the turbulent mass flux velocity in production of reynolds stress, and, in analog, turbulent kinetic energy. This is furthermore closely related to the b parameter (density self-correlation), since b appears in the production of turbulent mass-flux. Additionally, turbulent mass-flux appears in the primary production term of turbulent kinetic energy [102, 103]. It also appears in the second term of the Reynolds stress decomposition.

Figure 4.18 Shows the comparison between low and high Atwood numbers for the Turbulent Mass Flux (TMF) velocity, or the a parameter for the multi-mode case. Note that the axes are different between the two cases, highlighting the large increase with Atwood number. Further, in conjunction with the peak in the DSC befre reshock, the turbulent mass flux velocity also displays a peak in the bubble region. Again, this is primarily a phenomenon of the geometry of the interface. After reshock the interface displays an interesting trend at early times, positive values in the spike region. This denotes that the spike penetrating into the light gas is going slower to the left (positive fluctuation in velocity) when it is more pure heavy gas (positive density fluctuation). This is understood as, a thicker spike travels slower, signifying the finite energy availability of the mass extending from the interface. Thus a conservation of momentum is observed with ejecta-like features.

Along with the DSC at late times after reshock, the mass flux velocity displays similarity between Atwood numbers. The mass flux velocity is observed to be larger in the spike side at late times after reshock, with more interchange of high-density-contrast material for both Atwood numbers. However the mass flux velocity is around three times higher in the high Atwood number case.

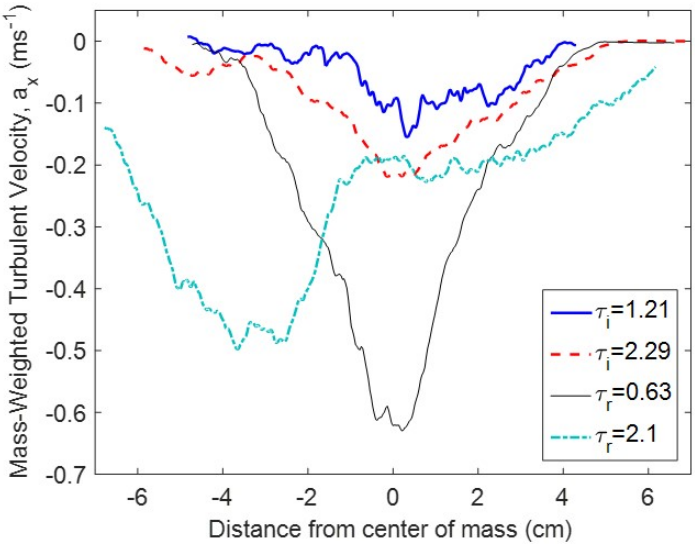

(a) N_2/CO_2

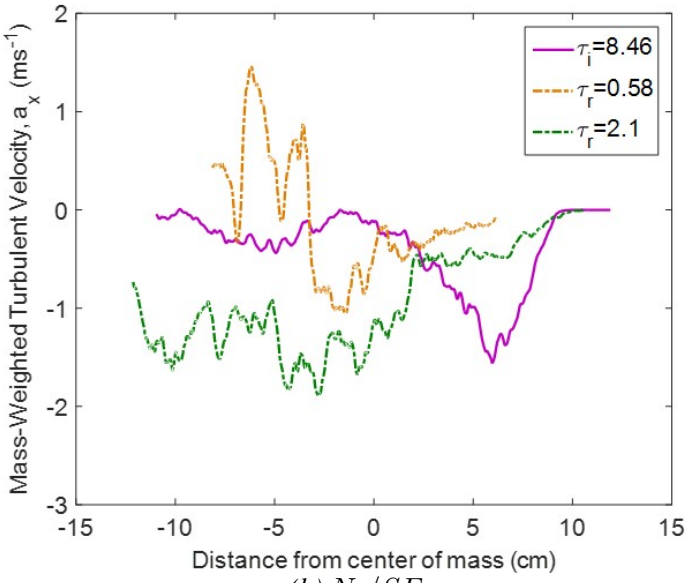

(b) N_2/SF_6

Figure 4.18: Turbulent Mass Flux (TMF) velocity, or the a parameter for the multi-mode case: (a) Low Atwood case. (b) High Atwood case.

4.2.3 Reynolds Stress

The Reynolds stress expresses the intensity of velocity fluctuations, and in this case, the Favre-averaged Reynolds stress expresses the quantity, weighted by mass. The trace of Reynolds stress is the turbulent kinetic energy (TKE) of the flow. The Reynolds stress and TKE are critical quantities for closure of many turbulence models. The on axis components indicate the energy in the flow, and act like a pressure, while the off axis components indicate the transport of momentum in the orthogonal direction by turbulent fluctuations, thus acting like a turbulent viscosity. The Reynolds stress is given by

$$R_{ij} = \langle \rho u_i'' u_j'' \rangle \tag{4.18}$$

where the double prime indicates Favre averaging ($u_i'' = u_i - \frac{\langle \rho u_i \rangle}{\langle \rho \rangle}$). The first dimension of velocity, which is the streamwise direction, or direction of shock travel, is denoted by u, while the spanwise direction is denoted by v, ie., $R_{12} = \langle \rho u'' v'' \rangle$.

Figure 4.19 shows three components of the Reynolds stress for the single and multi-mode cases of the high Atwood number case. These demonstrate that the single mode initial condition has a larger amount of reynolds stress in the streamwise direction, the R_{11} component. There are less intense fluctuations occurring in the spanwise direction for both initial conditions. Intuitively, the velocity fluctuations in the streamwise direction are not significantly selected to the fluctuations in the spanwise direction, as denoted by the low value of the cross correlation term throughout the mixing region.

In order to compare to low Atwood results, the R_{11} term is shown for the low Atwood case in Figure 4.20 along with an approximation. This approximation is often used and is the first term in the following expansion of the Reynolds Stress into Reynolds-averaged

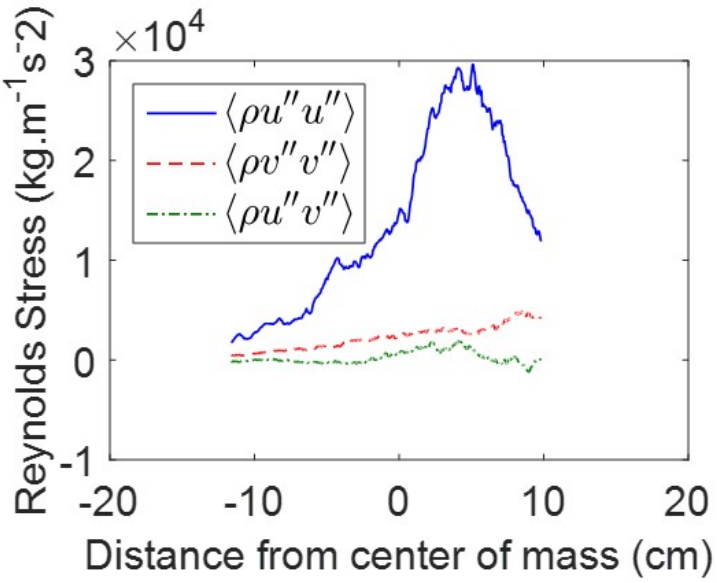

(a) Single

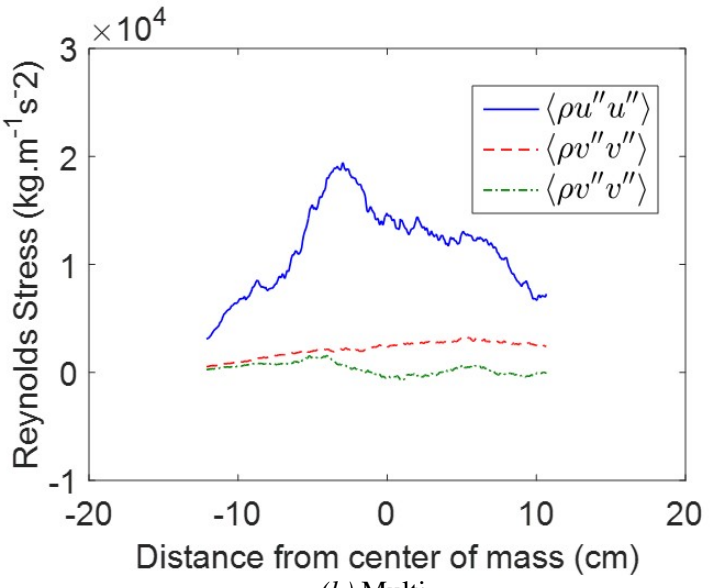

(b) Multi

Figure 4.19: Reynolds Stress for the High Atwood case for: (a) single mode IC. (b) multi-mode IC.

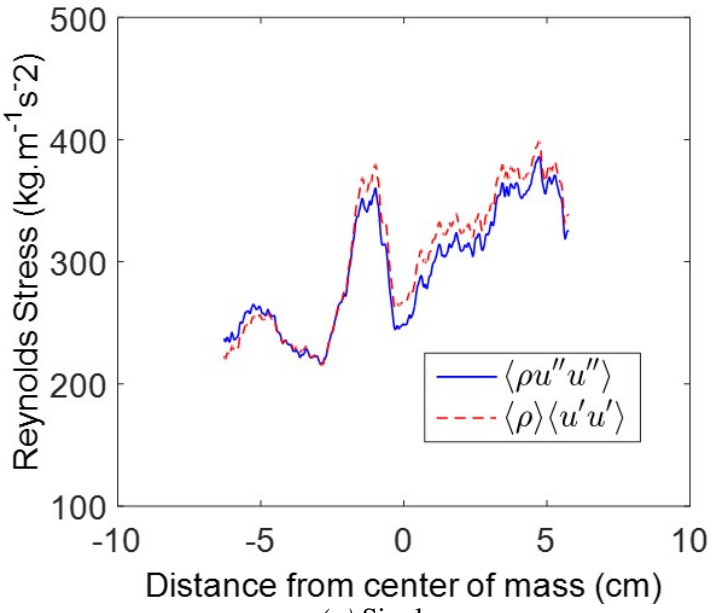

(a) Single

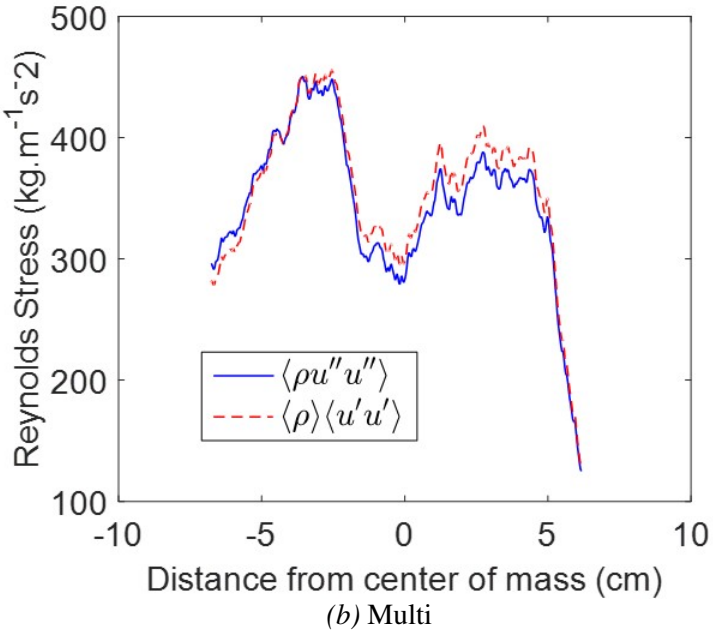

(b) Multi

Figure 4.20: Reynolds Stress for the Low Atwood case for: (a) single mode IC. (b) multi-mode IC.

components:

$$R_{ij} = \langle \rho u_i'' u_j'' \rangle = \langle \rho \rangle \langle u_i' u_j' \rangle - \langle \rho \rangle \langle a_i \rangle \langle a_j \rangle + \langle \rho' u_i' u_j' \rangle, \tag{4.19}$$

The Favre-averaged Reynolds stress can be simplified to the first term of this expression when the instantaneous local species concentration has a sufficiently low effect on the momentum, and the average density can be used. However, the second term contains the mass flux velocity, indicating that when the degree of correlation, or selection, between the density and velocity fluctuations is sufficiently large, this term will begin to have a nonnegligible effect on the Favre-averaged Reynolds stress.

The streamwise component of the Favre-averaged Reynolds stress and the first term approximation for the Favre-averaged Reynolds stress are shown in figure 4.20 for the low Atwood number case. Single and multi-mode initial conditions are shown here. There is a region of slightly elevated Reynolds stress in the spike region of the multi-mode case compared to the single mode case, with much similarity to the trend displayed in the high Atwood results. Further, the approximation is observed to be close to the actual value for the entire mixing region with differences of up to around 10% observed in some regions.

Figure 4.21 Shows the comparison between Favre-averaged Reynolds stress and the first term approximation for the high Atwood number case for the multi-mode initial condition. Figure 4.21a shows the multi-mode case for the Favre-averaged Reynolds stress and its first term approximation, and Figure 4.21b shows the difference between the two ($R_{ij} - \langle \rho \rangle \langle u_i' u_j' \rangle = -\langle \rho \rangle \langle a_i \rangle \langle a_j \rangle + \langle \rho' u_i' u_j' \rangle$). This demonstrates that although the percent difference is similar to the low Atwood number case, the absolute difference is much larger for the high Atwood number case. It is particularly important to note that the location of largest discrepancy occurs in the region where the turbulent mass flux velocity is also high. It is concluded that the triple correlation term is small, but positive, and thus the negative value of this expression illustrates the importance of the correlation

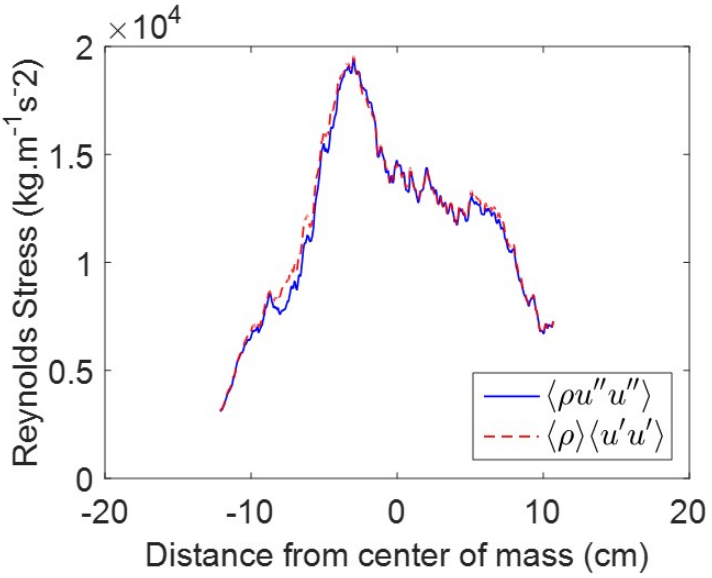

(a) Comparison

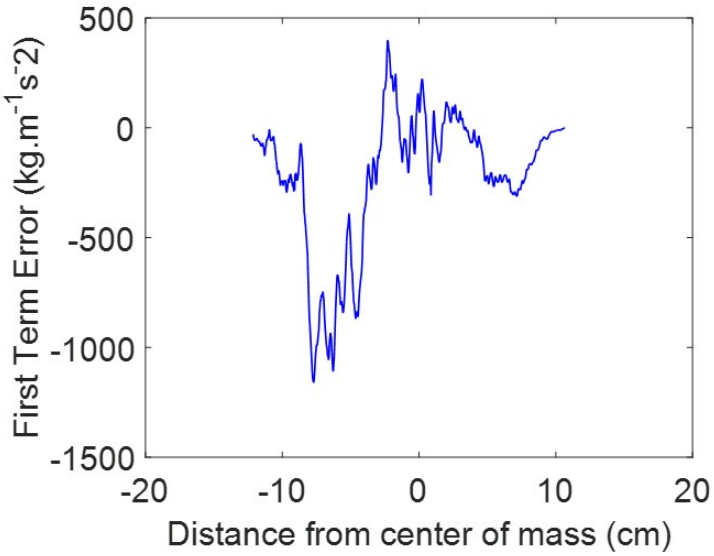

(b) Difference

Figure 4.21: Reynolds Stress for the High Atwood case multi-mode IC: (a) Comparison of favre-averaged Reynolds stress to the first term approximation. (b) first term error: the favre-averaged Reynolds stress minus the first term approximation.

of density and velocity fluctuations expressed by the a parameter for these flows, and in particular in applications where simplification is desired.

4.2.4 Anisotropy Analysis

An important descriptor of turbulent flows is the degree of directionality in the flow, or how the flow departs from rotational symmetry. This is called anisotropy, and is calculated from the velocity fields. It is related to the Reynolds stress and depends on how much of the quantity is in each component of the tensor, thus the anisotropy tensor is

$$r_{ij} = R_{ij} - \frac{1}{3}R_{kk}. \tag{4.20}$$

However, instead of considering the magnitude of the departure from isotropy in the flow, it is valuable to consider this magnitude relative to the total Reynolds stress, thus each component of the Reynolds stress is considered in relation to the total Reynolds stress magnitude. Thus, the normalized anisotropy tensor is defined as

$$\beta_{ij} = \frac{R_{ij}}{R_{kk}} - \frac{1}{3}\delta_{ij}. \tag{4.21}$$

Thus a value of 2/3 denotes that all of the Reynolds stress is contained in that component, while a value of -1/3 denotes that none of the Reynolds stress is contained in that component.

Figure 4.22 Shows the comparison between Atwood numbers for normalized anisotropy components for the multi-mode initial condition. Figure 4.22a displays a greater amount of isotropy near the center of mass of the mixing region, while there is some aniotropy near the edges of the mixing region with the streamwise component having a slightly proportionally higher amount of the Reynolds stress. The spanwise component contains little of the stress, and the perpendicular components are not very selected to each other,

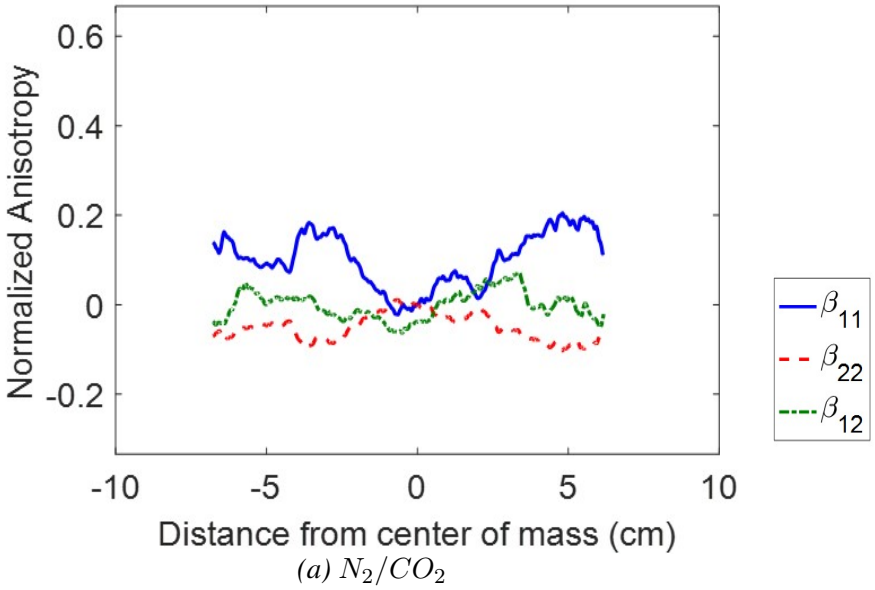

(a) N_2/CO_2

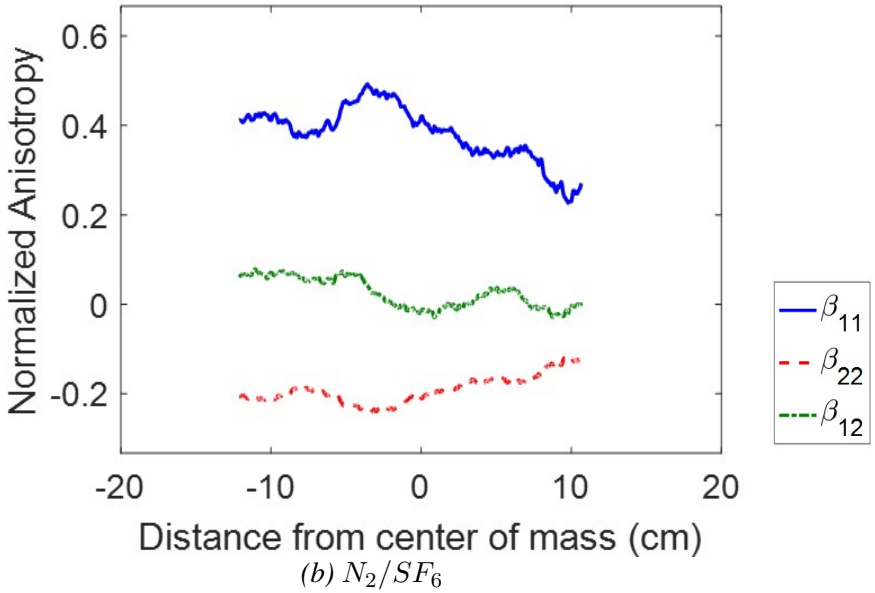

(b) N_2/SF_6

Figure 4.22: Atwood number comparison of Anisotropy for the multi-mode IC: (a) Low Atwood number case, N_2/CO_2 (b) High Atwood number case, N_2/SF_6.

denoted by β_{12}, which is nearly zero for the entire mixing region.

However, Figure 4.22b demonstrates a large amount of anisotropy with values closer to 0.4 for the bulk of the mixing region in the streamwise component. The spanwise component also demonstrates that it makes up very little of the total fluctuating stress compared to an isotropic state, which results in the negative values for β_{22}. Both components demonstrate a slightly more isotropic state in the bubble region. Again, the streamwise and spanwise components are not selected to each other, and do not constitute a large amount of the Reynolds stress, which is typical of isotropic flows.

The anisotropy demonstrated by the high Atwood case leads to the conclusion that this flow retains more of the directionality of the initial shock input than the low Atwood case, leading to higher mass flux and velocity fluctuations in the streamwise direction. This is an important conclusion for this flow because it indicates that the memory of the conditions at the onset of instability are retained for longer, even though the flow is at the same level of "maturity" or nondimensional time as the low Atwood number case, and even in more homogenous regions, where there is less memory of initial density contrast, there is still momentum memory in the flow.

4.3 Transition Evaluation

The definition of turbulence is founded on the phenomenon of growth of small perturbations into unpredictable chaotic motion given sufficient energetic input. The transition to this state is typically defined by criteria specific to the flow. There are several criteria which define various charistics of the flow. Hence a flow may have intense fluctuations or develop a wide range of scales in the motions of the flow. etc, but a flow need not be isotropic or homogenous. The criteria for RMI are not yet understood, but the current work shows that criteria for relevant scalar mixing flows are well surpassed. The importance of this transition is that the conclusions of memory of initial conditions are beyond

transition of the flow to turbulence, and the specific level of turbulence is evaluated via these quantities.

4.3.1 Reynolds Number

One of the foremost quantities in defining the state of the flow relates the momentum forces to viscous forces. This quantity is the Reynolds number. The momentum pushes the flow towards uncontrollable motion while the viscosity damps this motion. Given sufficient momentum, the flow will transition to turbulence where instabilities in the motions grow and become chaotic. This point where instabilities driven by large momentum overcome the viscous dissipation and grow into chaotic motions depends on the type of flow. Dimotakis proposed a value of 10^4 for transition in some mixing flows, and values of ten times this are proposed for full scale turbulence [104]. The current work evaluates the state of the flow based on Reynolds number and discusses the proposed criteria for this type of flow. The Reynolds number from kinetic energy, which is very similar to that calculated from growth rate in this flow, is calculated as

$$Re = \frac{K\delta}{\nu_{mix}}, \tag{4.22}$$

where K is kinetic energy, and ν_{mix} is the kinematic viscosity of the mixture. δ, the mixing layer thickness, is the length scale chosen instead of mixing width (h). Mixing layer thickness is a more relevant mixing length scale in this type of flow than the mixed width; this choice is more similar to the relevant length scales in other canonical flows, which were outlined by [104].

Figure 4.23 Shows the comparison between Atwood numbers of Reynolds number for the multi-mode initial condition. Figure 4.23a shows the Reynolds number before reshock. The N2/SF6 case is at a much later nondimensional time before reshock, because of the aforementioned differences in the temporal trajectories of the experiments

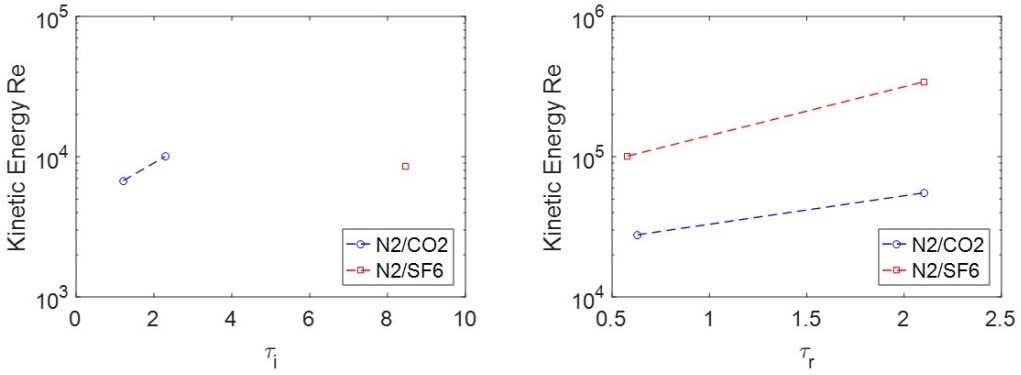

(a) Pre-RS *(b)* Post-RS

Figure 4.23: Atwood number comparison of Reynolds number from kinetic energy, Re_K, from the multi-mode IC : (a) Pre-RS (b) Post-RS.

which are accounted for by the nondimensionalization (2.7, 2.8), the latest time before reshock possible for the high Atwood case is much later, in both experimental time and nondimensional time. Both cases have Reynolds numbers near the 10^4 criterion. This could indicate that the flow is approaching transition, however the flow has not clearly undergone transition and visual inspection of the density fields, for instance, shows the same trend: some degree of perturbations growing, but not yet very chaotic, and not yet encompassing a large region of the flow.

For both cases after reshock a higher level of turbulent intensity is observed. Figure 4.23b shows the comparison of Atwood numbers for the multi-mode case after reshock. It is obvious that both cases have surpassed the criterion of 10^4 for Reynolds number, and the high Atwood case has a higher Reynolds number at both times after reshock. Further, the high Atwood number case displays a growth in Reynolds number which is greater than the low Atwood number case as the higher mixing layer thickness allows for larger scale turbulent fluctuations, and the higher density contrast leads to more intense fluctuations.

4.3.2 Energy Spectra

Turbulent flows exhibit fluctuations over a range of lengthscales. The fluctuations at the larger, driving lengthscales are thought to be separated by varying degrees from the smallest, dissipating lengthscales in the flow. The energy at the various scales was thought to flow from larger scales to smaller, but recent thought has considered the lengthscales as more interconnected, especially in light of increasing evidence of memory in turbulent flows [19, 20]. The current work considers the turbulent kinetic energy spectra and how they are affected by Atwood number. This one dimensional spectra of a generic quantity, $\varphi(x, y, t)'$ are calculated as

$$[E_{\varphi'}]_i = FFT(\varphi') \cdot conj(FFT(\varphi')), \tag{4.23}$$

where $FFT(\varphi')$ is the Fourier coefficient calculated from a fast Fourier transform (FFT) of the 2π periodic function $\varphi(x, y, t)'$ in the spanwise direction and $conj(FFT(\varphi'))$ is its complex conjugate.

Figure 4.24 Shows the comparison between atwood numbers of the spectra of turbulent kinetic energy (TKE) for the multi-mode initial condition, both for normalized (4.24a) and compensated (4.24b) spectra. Because the high Atwood number case contains significantly more kinetic energy, as shown in Figure 4.23, it is valuable to normalize the kinetic energy spectra by the maximum in order to compare the relevant features of each spectra. This method of displaying the energy content allows a comparison of the relative energies for different ranges of scales in each case. Figure 4.24a shows that the medium lengthscales contain slightly more energy in the High Atwood number case. Thus at the scales where the inertial range is forming, there is more TKE, whereas the ratio of the large lengthscales to the smallest lengthscales is similar between the two cases. The fiducial line for $k^{-1.8}$ is shown for reference.

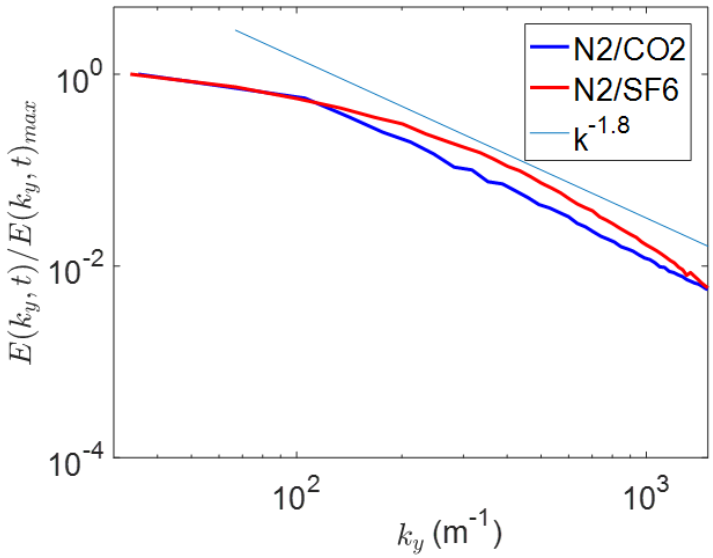

(a) Normalized Spectra

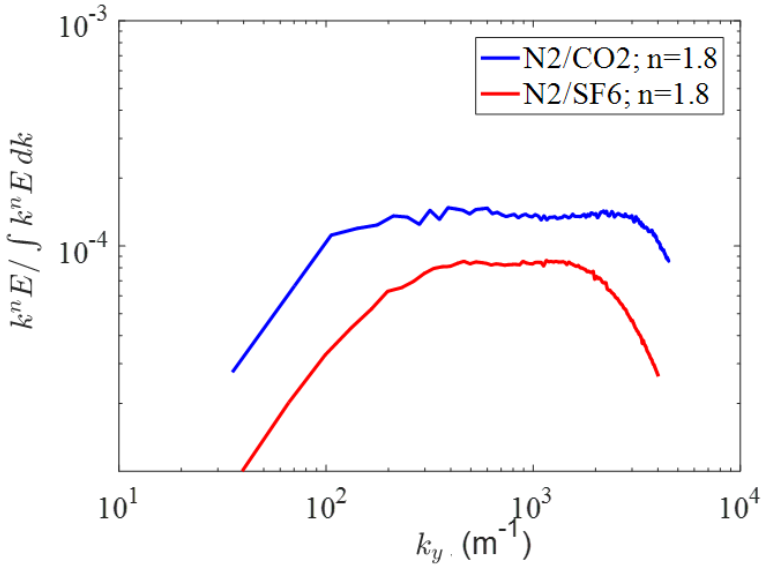

(b) Compensated Spectra

Figure 4.24: Turbulent Kinetic Energy (TKE) Spectra for both gas pairs for the multi-mode IC : (a) Spectra normalized by the maximum energy (b) Spectra compensated by k^n, where n=1.8 for both cases.

Although the differences in proportions of energy content across different ranges of scales for the two cases is apparent in Figure 4.24a it is not easy to observe how closely either case is described by a power law decay, which is the proposed trend for inertial ranges with constant energy transfer throughout the range. To investigate the existence and features of an inertial range, the spectra are each multiplied, or compensated by $k^{-1.8}$ in Figure 4.24b to illustrate the degree to which the inertial range follows this scaling in both cases. It is observed that the low Atwood number case follows this scaling for much more than one decade. This is a criteria that indicates separation of scales and transition to turbulence. The high Atwood number case, however, only displays this scaling for approximately one decade. This indicates that the momentum forces of the initial condition are more persistent in the high Atwood number case which is consistent with the findings that the high Atwood case retains more directionality illustrated by the high degree of anisotropy in the flow for this case. This shows that although the high Atwood case has more intense fluctuations and has surpassed several criteria for transition to turbulence, the flow has not achieved a state where all memory of initial conditions is forgotten. This has implications for the study of this instability in regards to self-similarity and how the state of the flow is defined from different parameters. It is also important to note that both cases follow this scaling reasonably well. This scaling agrees with the level of intermittency in these flows, due to their inhomogenous nature, but there is still much conversation in the community about the existence of common scaling across various parametric differences.

CHAPTER 5

HIGH-TEMPORAL RESOLUTION EXPERIMENTS

Because the RMI evolves temporally, it is desirable to capture the development from beginning to end. This has generally been accomplished by running the experiment multiple times and imaging at various stages in the development to form a complete sequence as presented in Section 4. However, because of the unpredictable variability in the growth of small perturbations in this instability, images in a sequence which are captured in this way are not connected in time. The current work uses simultaneous PLIF and PIV to analyze the time correlated evolution of RMI for the first time.

5.1 Comparison with High-Resolution Experiments

An initial campaign with the same experimental setup as the main campaign was undertaken to investigate the utility of high speed measurements. The initial campaign only employed PIV, while the main campaign used simultaneous PLIF and PIV. The evolution of vorticity for the Mach 1.55, and $At = 0.23$ case for both initial conditions is shown in Figrure 5.1. The latest time of the high speed development is compared to approximately the same time in the high resolution experiments. This field shows excellent overall agreement with the high resolution vorticity fields. Even though the two fields are from different runs, and the variation between runs inherent to the chaotic nature of the instability causes differences between the fields, this demonstrates the ability to capture many relevant scales in the vorticity dynamics of RMI. To clearly show the vorticity evolution, the images shown in Figure 5.1 have inter-image spacing of 250 μs. Early after reshock at 5.75 ms, the vorticity is concentrated in a small area due to shock compression of the mixing region and because deposited baroclinic torque is strongest where the den-

sity gradients are sharpest. As the interface overturns, vorticity redistributes. Whereas the single-mode interface is mostly characterized by positive vorticity, the multi-mode case has more negative vorticity due to additional features which cause negative baroclinic torque to be applied by reshock. The predominantly co-rotational vorticity of the single-mode case is observed to merge into two features, while the vorticity of the multi-mode case forms a more complicated field with a notable amount of negative vorticity. In this case, the vorticity is configured such that strong advection occurs in the center of the flow between regions of opposite signed vorticity as the interface continues to overturn at the long wavelength. The region of mostly positive vorticity is elongated but remains more towards the bubble region and the more negative region progresses up the tube towards the light gas. In both cases the comparison with the high-resolution vorticity field is reasonable. Although they are not from the same run, the general distribution of vorticity is very similar. The vorticity resolution from the high-speed data is not high enough, but by comparison with the high-resolution data, the small flow vorticity structures are still shown clearly.

To demonstrate the viability of the PLIF results in the high speed simultaneous PLIF and PIV results the processed high-speed PLIF images are compared with the high resolution images of the evolution previously presented in Mohaghar et al. [62] in Figure 5.2. show excellent agreement with previous high-resolution observations [62] on the same physical facility, especially at more predictable large scales. This can be seen in Figure 5.2 where the the PLIF mixture fraction fields from high-resolution experiments at W3 are compared to the images of the corresponding high-speed case at various evolution times. Supplementary video S1 shows the full evolution of the interface at the three different windows $W1 - W3$ from the current experiments (note that the three views in $W1-W3$ are from different experimental runs). Note that while the previous data was acquired from separate experiments (one field per experiment-time), the current data shown

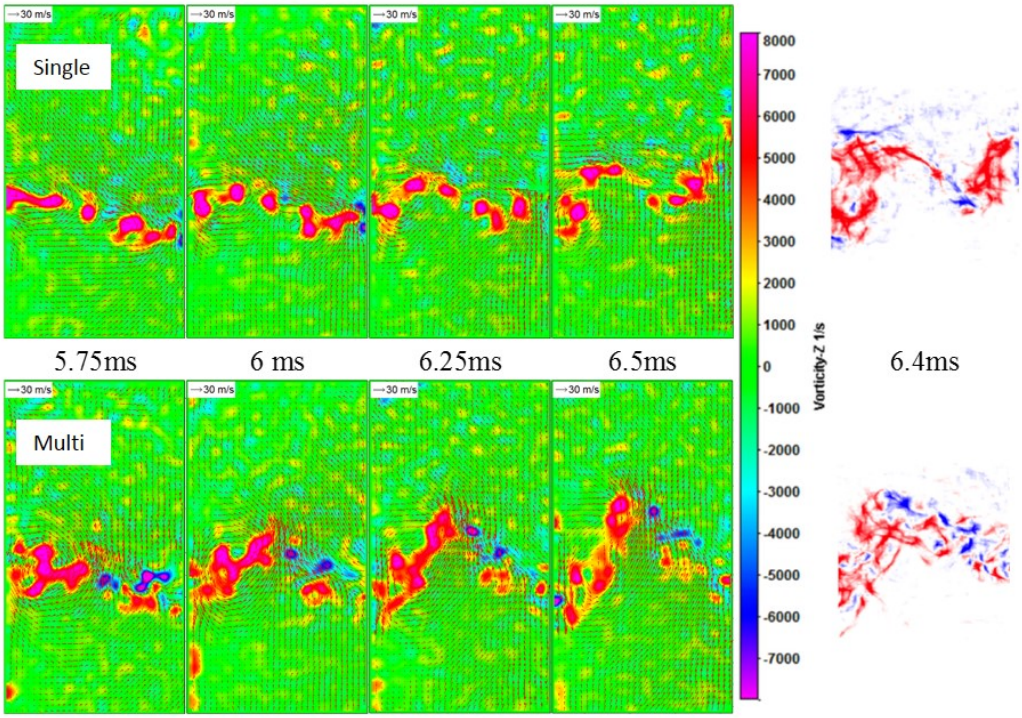

Figure 5.1: High-speed PIV image sequences and the corresponding vorticity fields for single (top row) and multi-mode (bottom row) cases shown with incident shock direction from top. Reshock occurs at t 5.3ms. High resolution images are shown on the far right with a blue-to-red color bar of the same range for clarity (from Mohaghar et al. [62]).

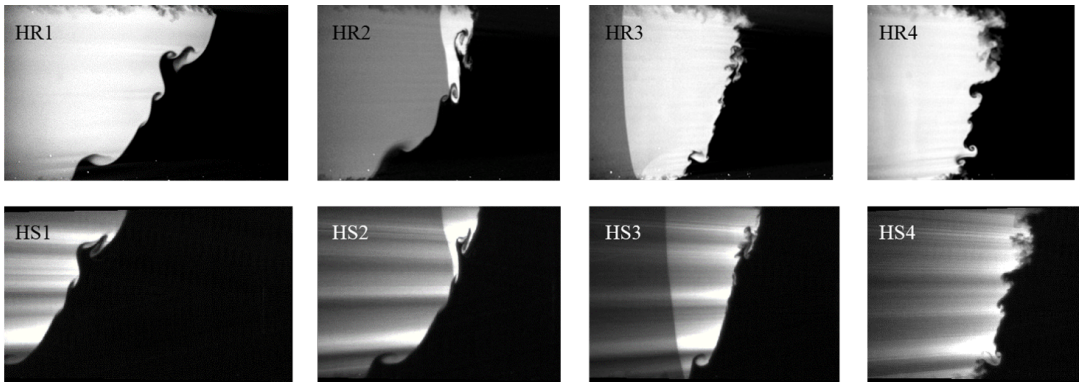

Figure 5.2: Qualitative comparison of interface images captured employing low-speed, high-resolution (HR, from Mohaghar et al. [62]) PLIF and current high-speed moderate resolution (HS) PLIF are shown at four times ($1-4$, $5.0, 5.2, 5.3, 5.5\,ms$ after incident shock). The passage of reshock from right to left can be seen in images 2 and 3.

is acquired from a single continuous progression of the interface. This enables tracking the evolution and mode merging of individual flow structures that were previously not possible owing to random variations in the interface growth at the smallest scales. Further, the current experimental data also enables the study of interface compression due to reshock (times 2-3 in Fig. 5.2), phase inversion of mean interface evolution, and the continuous evolution of the small scale features (time 4 in Fig. 5.2). The complete progression as a video can be seen in the supplementary video S1, which shows details of the evolution of small turbulent vortical scales and the turbulent mixing of the two gasses by the instability mechanisms. Also evident at late times in the supplementary video S1 is the aforementioned reduction in laser energy at late times, and the associated decrease in signal-to-noise ratio in the PLIF results.

5.2 Velocity and Vorticity Dynamics

Richtmyer-Meshkov instability is primarily a vorticity-driven phenomenon, and the current experiments provide valuable information on the evolution of the same. Figure 5.3 shows the velocity fields overlaid on the vorticity contours at three important times of

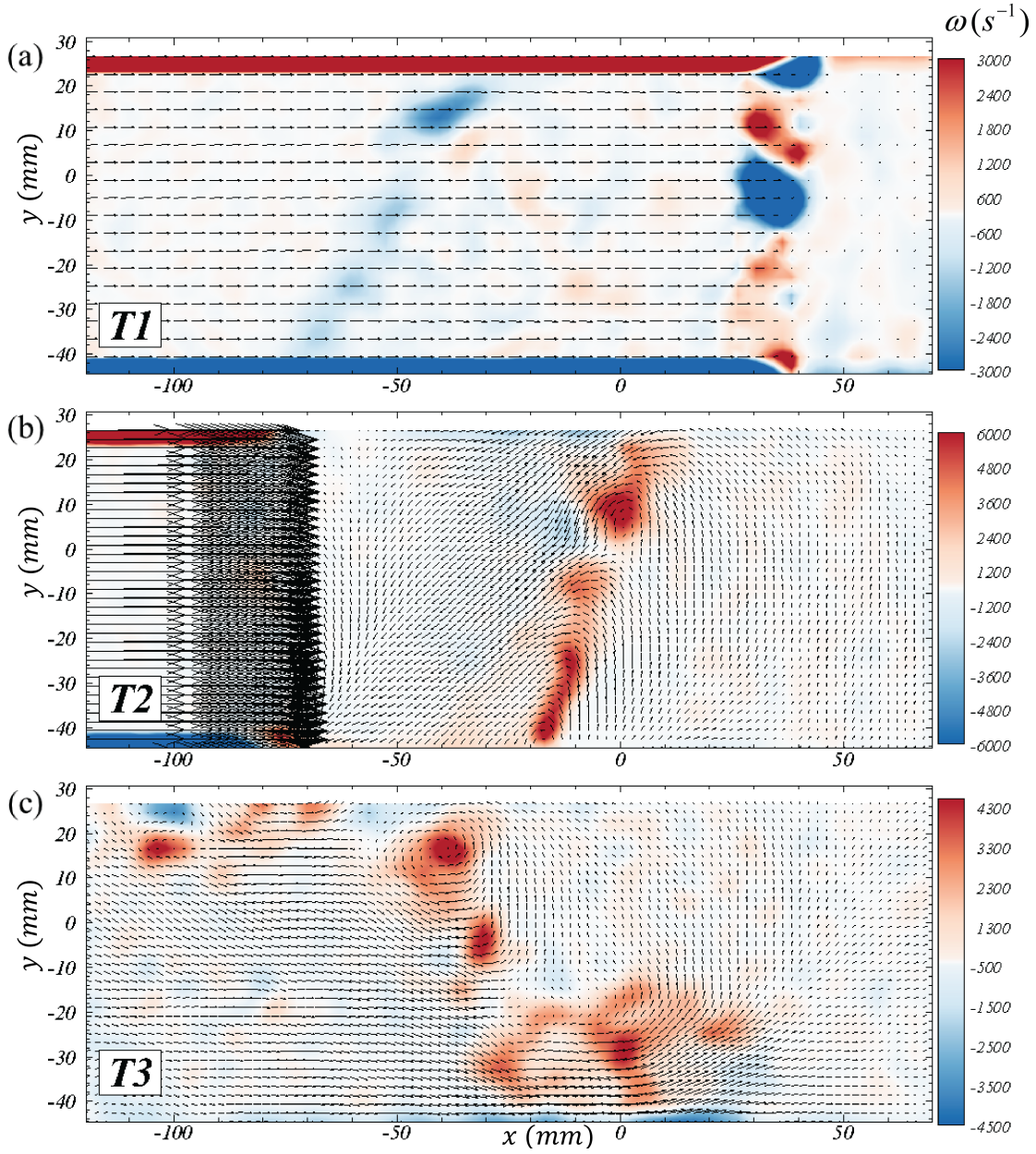

Figure 5.3: Evolution of vorticity (ω in s^{-1}) at three different times corresponding to *(a)* late-time pre-reshock ($T1 = 4.9\,ms$), *(b)* early time post-reshock ($T2 = 5.3\,ms$) and *(c)* late time post-reshock ($T3 = 7.5\,ms$). Velocity vectors are scaled to 1% of magnitude in *(a)* and to 10% in *(b)* and *(c)*. See Supplementary video S2 for the full evolution in W3.

the evolution - late time interface after incident shock ($T1 = 4.9\,ms$ from incident shock), early time interface after reshock ($T2 = 5.3\,ms$), and late time after reshock ($T3 = 7.5\,ms$). Contour levels of magnitude $< 8\%$ of peak are not shown to avoid small-scale noise in gradients and for clarity. The wholly negative orientation of deposited vorticity at T1 (from the initial orientation between interface and incident shock) is accurately captured. Also captured at T1 is the noise in vorticity from spurious vectors at the reshock front ($30\,mm \lesssim x \lesssim 40\,mm$, due to refraction of particle signal) and near the walls ($y > 20$ and $y < -40$, due to large shear). As the vortex sheet is stretched, interface at T1 develops the vortex reorganization into pockets of concentrated clockwise vorticity. This also manifests as strong perturbations in shape of the interface as the reshock deposits additional vorticity on the same at T2. The phase inversion and strengthening of these vortices (owing to the additional deposition and greater mismatch) is evident immediately after reshock. The subsequent modal evolution, vortex merging and breakdown leading to a rich turbulent mixing environment is evident at T3. Supplementary video S2 captures this detailed progression, and is the first measurement of the high-speed RMI evolution. The final interface velocity field shows strong intermixing and mean scalar transfer of each gas into the other.

The turbulent kinetic energy on the interface ultimately responsible for turbulence is deposited by shock at very small length scales [$\sim O(\text{diffusion thickness}) \approx O(mm)$]. The vortex stretching and inviscid instability mechanisms redistribute this turbulent kinetic energy spatially and spectrally leading to a rich range of velocity (and consequently scalar) scales. The two-dimensional estimate to the turbulent kinetic energy (TKE_{2D}) can be obtained via the in plane velocity fluctuations as the flow is statistically homogenous in the $z-$direction. Assuming reflective symmetry of the initial conditions and spatial homogeneity in the spanwise direction, Figure 5.4 shows this measure from fluctuating velocities computed via spanwise averaging. Immediately after the interaction with the

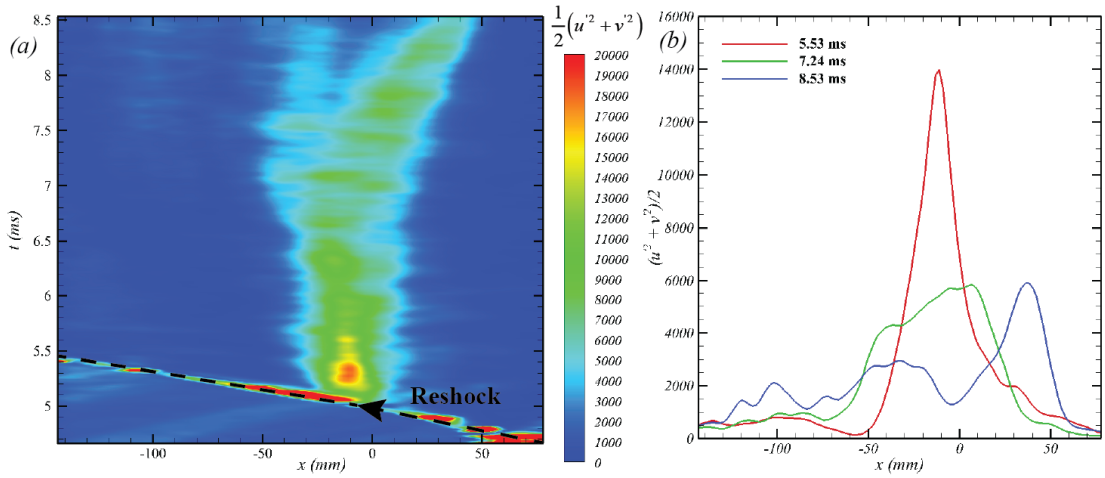

Figure 5.4: (a) Temporal evolution of two-dimensional, spanwise averaged TKE estimate and (b) the streamwise redistributions of the peak energy at different evolution times after reshock.

reshock, a localized peak in turbulent fluctuations is observed. This peak TKE grows spatially across the interface as the classical instability mechanisms redistribute the same. Further, the total TKE_{2D} in the FOV remains relatively constant owing to the negligible dissipation relative to redistribution mechanisms (this value starts to show a decay-trend at late times for $t > 8\,ms$). These demonstrate the strong inverse cascade of energy expected at early times of the instability growth without a significant dissipation.

Equivalently, the primary momentum for turbulence and mixing comes form the deposited baroclinic vorticity from the shock-interface interactions during incident shock and the reshock. Many studies studying the growth, transition and mixing of the RMI using computational methods approach the problem as two separate processes – (1) the shock-interface interaction (responsible for initial vorticity deposition), (2) and the subsequent evolution of the same (responsible for mixing). This decouples the compressibility effects involved in RMI initiation from the subsequent hydrodynamics, which can then be analyzed using divergence-free field analyses (Biot-Savart time-integration, e.g. [2]). The mechanics of the shock-induced vorticity-deposition has been done in many previous studies and depends on the problem geometry (interfaces vs bubbles [105, 78]), shock-

propagation direction (light-heavy vs heavy-light [106, 78, 1]), strength of secondary waves (reflected and refracted shocks and rarefaction waves [106]), etc. The availability of high-speed measurements of PIV and PLIF enable us to study the vorticity-deposition models and provide direct experimental information to evaluate the same. The current experiment provides two cases for the evaluation of such models - interaction of the incident shock with the inclined interface and (a short time later) the interaction of the reshock with the interface that has now slightly evolved to a more complex shape. In the following analysis, we use normal symbols ($\rho_{1,2}$, c, etc.) to refer to unshocked properties, *prime* ($'$) annotations for once-shocked properties (after passage of incident shock), and *double-prime* ($''$) for twice-shocked properties (after passage of reshock). Additionally, the subscripts 1 and 2 correspond to light (N_2) and heavy (CO_2) gasses respectively. These properties are obtained via 1-dimensional gas dynamics analysis which are detailed in the works of Mohaghar [64].

Assuming no dissipation of deposited vorticity, the measured value of the circulation is compared with the shock-polar model of Samtaney and Zabusky [78] (hereafter referred to as SZ94) which estimates the deposited circulation (σ) per unit interface length as

$$\frac{\sigma}{c_1/\sqrt{\gamma}} = (1-\eta^{-\frac{1}{2}})(\sin\alpha)(1+M_i^{-1}+2M_i^{-2})(M_i-1)(\gamma^{\frac{1}{2}}/\gamma+1). \qquad (5.1)$$

Here, the c_1 is the speed of sound in unshocked nitrogen, $\eta = \rho_2/\rho_1 > 1$, γ is the mean ratio of specific heats, α is the misalignment between the interface and the shock (10° here), and M_i is the Mach number of the incident shock.

Figure 5.5 shows the evolution of the net circulation on the interface seen in W3. The interface as viewed in this location is already shocked by the incident shock as it enters the field of view, and thus starts with a non-zero circulation (net-negative vorticity here). This comparison, shown in Figure 5.5 at $t < 5.0\,ms$, shows a remarkable agreement with the estimated circulation on the interface. Also shown in Figure 5.5 are the net positive

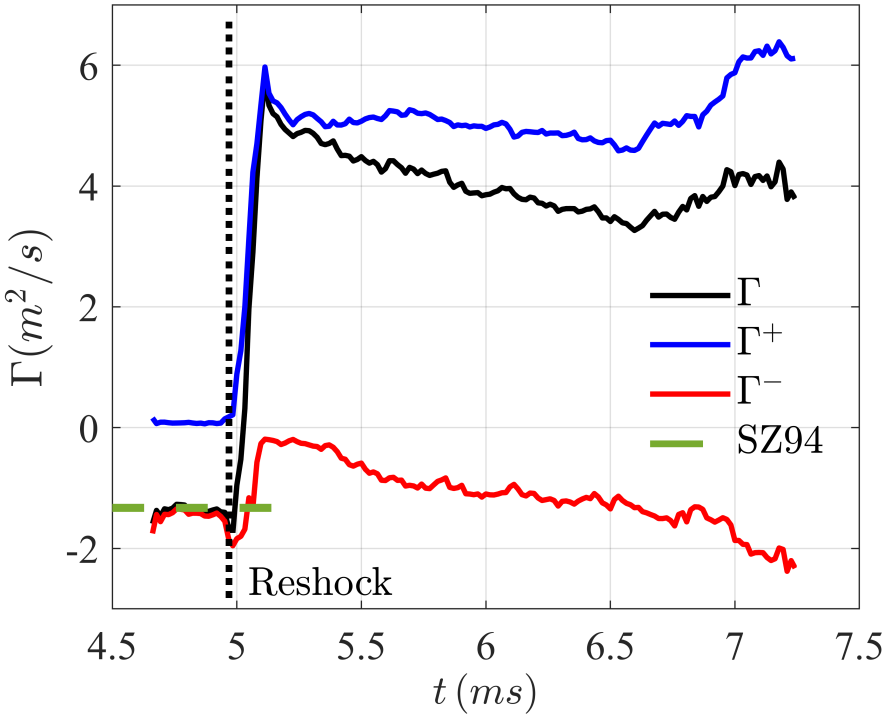

Figure 5.5: Evolution of the circulation of the interface by net vorticity, positive-vorticity and negative vorticity.

(Λ^+) and negative (Λ^-) circulation evolutions with time. Bulk of the circulation comes from the reshock, which quickly reorganizes owing to the unstable nature of the interface. This reorganization happens with negligible dissipation (shown by near-constant evolution of Λ^+), though the net circulation reduces in time. This linear decay in net vorticity is entirely consistent for small-inclination interfaces, as was previously noted in the computations of McFarland et al. [96], and arises due to a flux of negative vorticity from the wall-vortex (clockwise oriented) that detaches from the wall towards the center of the shock-tube [1]. The complex interaction of the interface deposited vorticity and the wall-vortex at late times ($t \gtrsim 6.5\,ms$) results in a net increase in both clockwise and counter-clockwise vorticity, as can be seen in supplemental video S2.

More importantly, we can also utilize the late-time pre-reshock interface configuration (at time t_r^-, Figure 2.16a) measured using PLIF images and the velocity fields after

reshock (t_r^+, Figure 2.16b) to study the net vorticity-deposition by the reshock. For this analysis, the shock propagation configuration is 'slow-fast' in nature (heavy-to-light gas), deposition is assumed to be regular, and occurring over an interface of small perturbations ($A/\lambda \leq 0.1$, where A is the perturbation amplitude, and λ is perturbation wavelength [1]). We evaluate two models commonly used for vorticity initiation - (a) one based on shock-polar analysis and asymptotic treatment of shock refraction effects (Samtaney et al. [1], hereafter referred to as SRZ98), and (b) model based on integration of baroclinic torque, a first order approximation of impulsive acceleration and one-dimensional gas dynamics assumptions (Weber et al. [2], hereafter referred to as WCB2013). The reader is referred to the original works [1, 2] for more details of the models. We invoke the assumptions of 'regular' shock-refraction (ignoring the reflected and refracted shock and rarefaction effects), small perturbation amplitudes, impulse density gradients in the shock-propagation-direction at the interface, and a single-valued nature of the interface profile (at locations where this is strictly not obeyed, we consider the interface location representing the strongest density gradient in shock-propagation direction). Additionally, the interface is assumed to have infinitesimal width, and all the vorticity is assumed to be concentrated as an impulse function around it. Under these assumptions, the SRZ98 model can be summarized for the current case as

$$\frac{\sigma(s)}{c_2'/\gamma^{1/2}} = \frac{2}{\gamma^{1/2}}\left(1 - \frac{1}{\sqrt{\eta'}}\right)\xi(M_r)\sin\left[\alpha'(s)\right] \tag{5.2}$$

where $\sigma(s)$ is the deposited circulation per unit length along the interface coordinate (s), c_2' is the sound speed in heavy gas, $\eta' = \rho_1'/\rho_2' < 1$, $\alpha'(s)$ is the mismatch angle between the local tangent of interface and the reshock, M_r is the Mach number of reshock, and

$$\xi(M_r) = \frac{4\gamma}{\gamma+1}(M_r - 1). \tag{5.3}$$

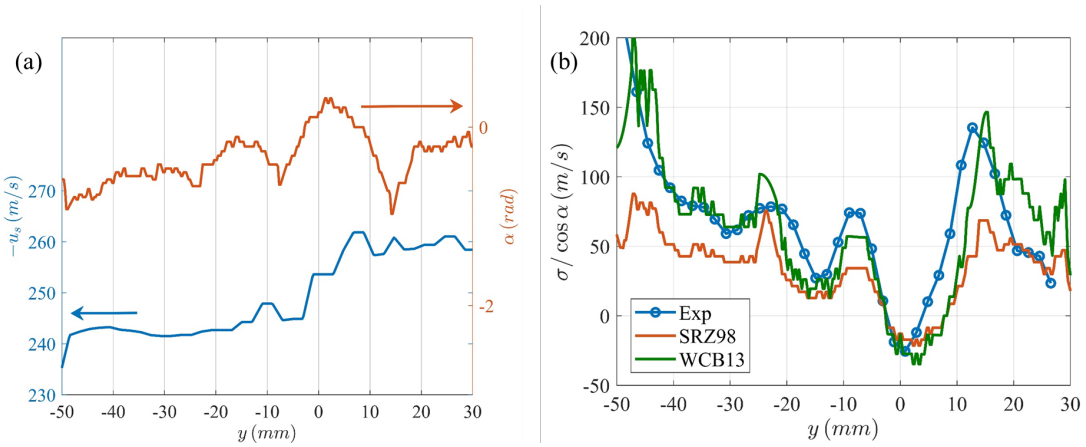

Figure 5.6: (a) The interface jump velocity and the misalignment of interface with reshock along the shock tube width, and (b) comparison of deposited circulation per unit shock-tube-width with the models of SRZ98 and WCB13.

Similarly, the estimated reshock-deposited-vorticity from the WCB13 can be rewritten for the current assumptions as

$$\omega(s) = \frac{u_s(s)\,(\rho_2' - \rho_1')\,(-\tan\alpha)}{\frac{1}{2}\,(\rho_1' + \rho_2')} \tag{5.4}$$

Here u_s is the jump in interface velocity from before to after reshock (note that there is a ratio of impulse function to its heavyside function that evaluates to unity at the interface and has dimensions of 1/length scale). The orientation of the interface immediately before its interaction with reshock forms the initial condition for the models. The 2-dimensional interface shape $s(y)$ before reshock is extracted from the PLIF images at $t = t_r^-$ to compute the local angle $[\alpha(s)]$ with respect to reshock (reshock is assumed to be vertical). The jump velocity, $u_s(s) = u_s^+ - u_s^-$ of the interface from reshock is also measured from the pre-reshock and post-reshock scalar and velocity fields (u_s^- and u_s^+ respectively). The variation of these two quantities along the shock-tube width (and along the interface, owing to its single-valued nature) is shown in Figure 5.6a.

Finally, the distribution of net circulation per unit interface length is computed from

the measured vorticity field, $\omega(x, y, t)$ as

$$\sigma(s) = \cos\alpha \int_{s(y)-\Delta/2}^{s(y)+\Delta/2} \left(\omega(x, y, t_r^+) - \omega(x, y, t_r^-)\right)\, dx \tag{5.5}$$

where Δ is an arbitrary neighborhood around the interface to fully encompass the measured/diffuse vorticity field.

Figure 5.6b shows the comparison between the predicted circulation deposition per unit shock tube width, $(\sigma/\cos\alpha)$, by the two aforementioned models together with the experimentally measured counterparts. The figure shows a remarkable agreement between the two models and the experiments, justifying both the approaches for these conditions. It serves to note that the SRZ98 model as is presented here utilizes only the measured shape [$s(y)$], and implicitly estimates the jump velocity (u_s) based on 1-dimensional gas dynamics relations. The WCB13 model, however, directly utilizes the measured jump velocity profile across the interface together with the interface orientation relative to the shock. This latter approach offsets some of the assumptions made in the current work, which lead to the discrepancies. For example, the assumption of single interface interaction (that the interface is a single valued function) is strictly not valid everywhere (i.e. $10\,mm < y < 20\,mm$), and the ability to specify a jump-velocity profile in WCB13 from experiments improves the estimated vorticity deposition in the corresponding region. This deposited circulation serves as the initial condition for subsequent instability growth, transition and mixing dynamics. While many computational studies have investigated the ability of these models to represent the deposited baroclinic vorticity [e.g. 2, 1, 107, etc.], the current work experimentally measures the interface orientation and the vorticity before and after reshock in a time-resolved manner to provide a direct validation of slow-fast vorticity deposition.

5.3 Mixing Dynamics

The goal of the current simultaneous diagnostics is to visualize the effect of turbulent velocity scales and mixing simultaneously. Figure 5.7 shows the mixing induced (via PLIF images) by the vortical activity represented by the contours of vorticity. The Supplementary video S3 shows the continuous time version of the figure, elucidating the coupling between the mixing and vortical activity in an RMI. Pre-reshock, it can be seen that the deposited vorticity organizes itself into pockets of concentrated vortical structures, as the associated perturbations grow. The current work shows a clear lack of mixing transition [104] at this time, with very little mixing activity between the two gases. This late time interface before reshock at T1 forms the initial condition for the subsequent vorticity deposition by reflected shock at T2. A phase reversal is noticed as the opposite signed (positive) vorticity deposition occurs, which leads to strong vortical structures. Most of the intermediate-time turbulent mixing post-reshock is observed to be concentrated around these vortical hotspots. The interface sandwiched by these structures undergoes further shear instabilities leading to a sharp rise in scalar mixing, that continues until the advent of the expansion wave.

Molecular mixing in turbulent environments is a phenomena connected to a large range of scales, and the utility of current measurements lies in the ability to track temporal evolution of these scales. Figure 5.8 shows an illustrative temporal sequence highlighting these small scale dynamics (see Supplemental video S4 for evolution at full temporal-resolution). The vorticity contours overlaid on the PLIF images identifies two vortices (X and Y marked in Figure 5.8a). The velocities are marked in the frame of reference of the vortex X, showing the swirling motion around the same [108]. Both vortices are formed from the reshock-initiated vortex sheet, and the subsequent roll-up due to its unstable nature. Under their mutual influence, the symmetric-vortices approach each other and eventually merge [109]. This ‘mode-merging’ of vortices results not only in backward

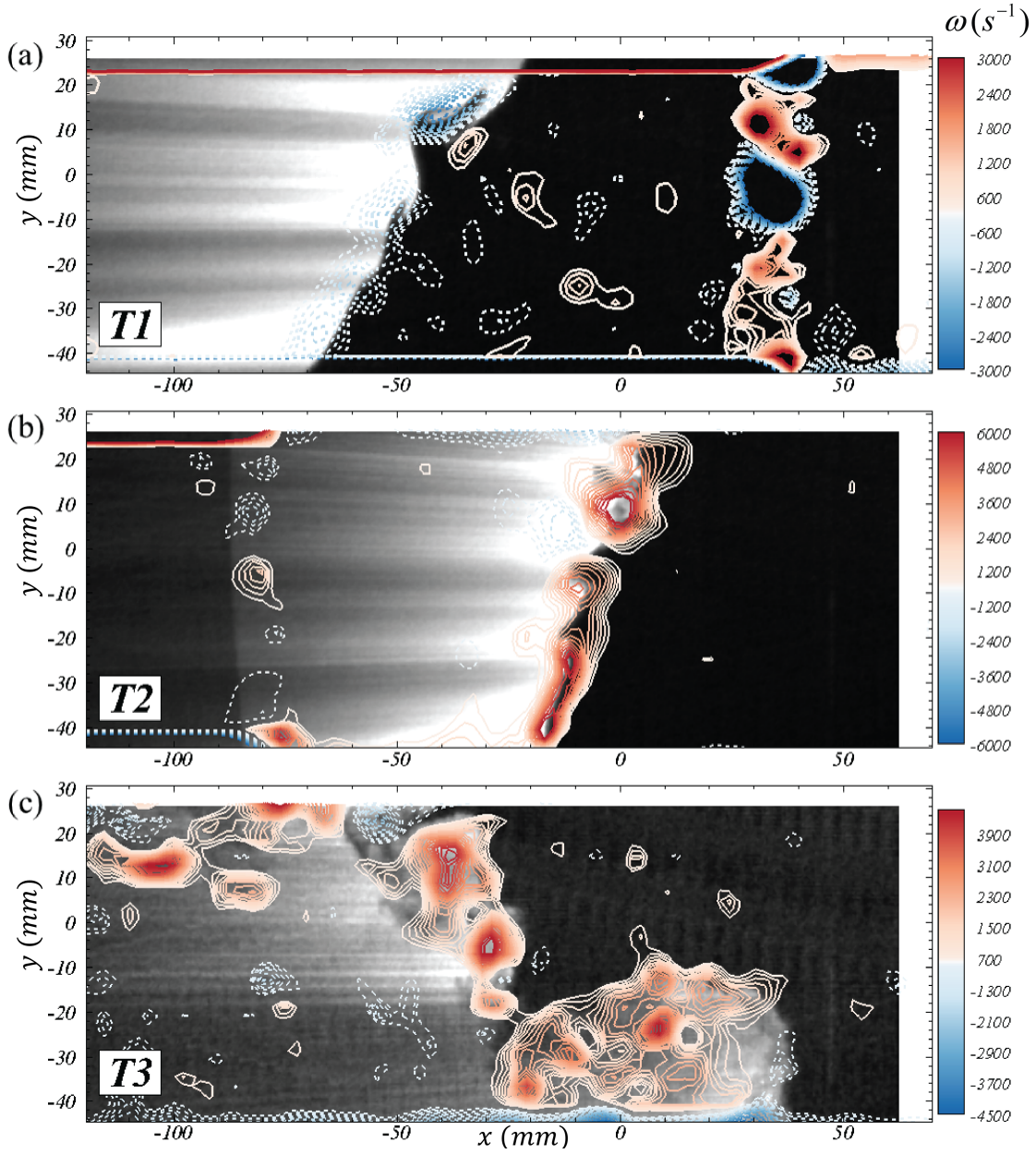

Figure 5.7: The vorticity-dominanted-mixing characteristics of RMI shown via contours of vorticity (ω) and corrected PLIF intensities (I_N). *(a-c)* correspond to same times *T1–T3* described in Fig. 5.3. The mixing activity of the gasses is concentrated as pockets of strong vorticity (in s^{-1}). See Supplementary video S3 for the full evolution in W3.

scatter of turbulence energy to smaller wave-numbers (large scales), but also in a local spike in scalar mixing as can be seen between Figures 5.8 f-i. This is the primary mixing mechanism in early stages of these vortex-dominated flows, and the mode merging has been studied theoretically ([e.g. 110, 110, 111, 112, etc.]), experimentally ([e.g. 110, 111, 113, etc.]) and using computational tools [e.g. 114, etc.]. However, existing studies on the effect of the mode-merging on scalar mixing (and specifically in variable density flows) are limited in scope and physics by the limitations of mixing models, or to low Reynolds numbers owing to the complexity of the same. The current high spatio-temporal resolution experiments are the first of its kind to capture this mode-merging and the induced mixing, specifically for shock-driven variable density phenomena. These advantages in the current diagnostics enable such studies related to temporal evolution of small scales that were previously not possible with conventional low speed approaches. Other possible directions currently being studied are the studies of vortex-accelerated vorticity deposition (VAVD) [114], vorticity-based mixing models, etc.

The current work demonstrates of the vortex dominated behavior of the turbulent mixing via time-resolved measurements of the vortex evolution. Further, the constraints on spatial resolution at these high speeds, especially in the velocity fields, is seen at instances where the PLIF images show vortical structures that are not captured individually by the vorticity fields owing to the lower resolution of the latter (see Supplementary video S3 at early times after reshock). This emphasizes the need for a coupled investigation using both high-resolution (low speed) and high-speed data, until such advances in imaging are available.

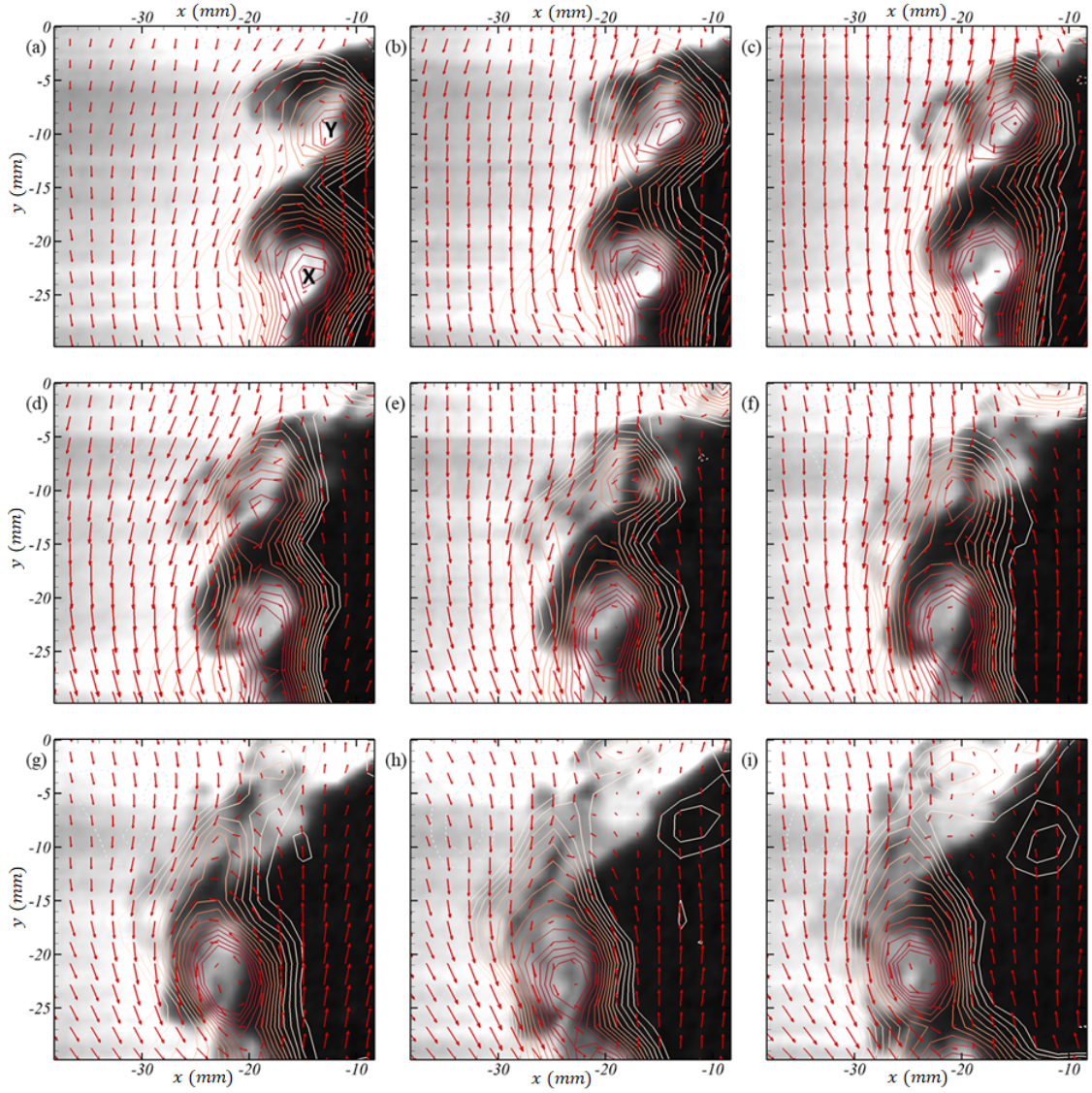

Figure 5.8: An illustrative temporal evolution of merging between two vortices [X and Y in *(a)*], and the associated scalar evolution shown in snapshots $67\,\mu s$ apart, starting at $5.550\,ms$ after incident shock in *(a)*, $5.617\,ms$ in *(b)*, $5.684\,ms$ in *(c)*, $5.751\,ms$ in *(d)*, $5.818\,ms$ in *(e)*, $5.885\,ms$ in *(f)*, $5.952\,ms$ in *(g)*, $6.019\,ms$ in *(h)* and $5.086\,ms$ in *(i)*. The vectors are velocities in the frame of reference of vortex-X (same scale as Fig. 5.3, in m/s) in (a) and line-contours represent vorticity with the same levels as Fig. 5.7 (in s^{-1}). See Supplementary video S4 for the evolution at full temporal resolution.

CHAPTER 6
CONCLUSIONS AND FUTURE WORK

6.1 Conclusions

The effect of Atwood number along with its relationship with initial conditions for the Richtmyer–Meshkov Instability were observed, and connected to a number of characteristic differences in the flow physics, with comprehensive experimental simultaneous velocity and density field statistical analysis for the first time compared between Atwood numbers. From the qualitative analysis of concentration field time sequences, it is strikingly clear that the Atwood number plays a key role in the development of the interface, resulting in bubble-spike asymmetry, and modulation of the effect of the initial condition. The growth of the mixing width amplitude before and after reshock were both driven higher by higher Atwood number. The qualitative results and growth results corroborate many previous experimental and computational findings, and the application of a scaling law [54, 96] showed indication of self similarity in the mixing width amplitude while other differences were apparent even at the same nondimensional times due to the difference in Atwood number. The Sadot model captured the growth of each Atwood number case best before reshock, while the model of Mikaelian showed excellent agreement with both Atwood number cases after reshock. At the molecular level of mixing, the quantities mixing layer thickness and mixedness indicate that the presence of mixed material is less in the high Atwood number case before reshock due to the rapid stretching of the interface, which outpaces molecular mixing. After reshock, the growth rate of the high Atwood number case is driven even higher, along with the molecular mixing which is partly due to the large contact surface between the gases upon which the shock imparts

vorticity.

The bubble-spike asymmetry observed in the high atwood number case is associated with species-dependent momentum dynamics, a phenomenon which marks flows where there is a high density contrast. This is highlighted in this flow due to the wavelength of the underlying inclined perturbation. The prominent bubble-spike asymmetry plays a factor in the density-self correlation, leading to increased values at the bubble edge in streamwise profiles of the statistic. The field values, presented for the first time for this atwood number, show spatial differences between initial conditions due to higher presence of local inhomogeneities in the multi-mode initial condition, which are actively mixing due to shear and rotation in the flow observed in the velocity fields. This results in a secondary peak in the bubble region of the profiles for the multimode initial condition. At high Atwood number for this flow, it is very clear that the Boussinesq approximation is not valid. The first term of the expansion of the density self correlation provides an approximation for the quantity; however, this approximation shows discrepancies of up to 20% from the actual quantity.

With a direct comparison being made experimentally for the first time in the correlation between density and velocity fluctuations, the effect of Atwood number on the selection of velocity to density fluctuations can be analysed. Large differences in mass flux velocity were shown between Atwood number cases, with positive mass flux resulting from interfacial momentum conservation in spike features early after reshock, but becoming universally negative after further development.

Further, the comprehensive experimental comparison between Atwood numbers for Favre averaged Reynolds stress is performed for the first time. Similar behavior to the mass flux velocity and density self correlation was observed in Reynolds stress magnitude and its boussinesq approximation where the high Atwood number case shows high discrepancy between the Favre-averaged Reynolds stress and its first-term approximation.

This discrepancy was observed primarily in the spike region which also showed high mass flux velocity, demonstrating the connection between species and velocity in these types of high Atwood number flows.

A high degree of Reynolds-stress anisotropy is observed in the high Atwood number case, with very high normalized values in the streamwise component also due to the high momentum disparity, in the flow resulting in delayed isotropization of the high density material. This anisotropy indicates in a strong retention of directional dependence along the direction of energy input by the shock, although the flow has transitioned to a turbulent state.

For a transition to turbulence to occur there must be a formation of a large enough inertial range. This is evaluated by the ratio of the Liepmann-Taylor to inner viscous scales. Lombardini [115] assumes that the flow will have an established inertial range if this ratio is much larger than 1, which is equivalent to the criteria $Re > 10^4$ suggested by Dimotakis [17]. Consistent with previous works, this criteria was met after reshock by both Atwood number cases. The Reynolds number was observed to be higher in the high Atwood number case, with a higher rate of increase as well. Both Atwood number cases demonstrated the same scaling of $k^{-1.8}$, while the high Atwood number case demonstrated a developed, but smaller range of scales which follow this trend; congruent with the elevated level of anisotropy in the high Atwood number case. Although a scaling law based on self-similarity was demonstrated to successfully collapse the mixing width amplitude [54, 96], the various differences between the Atwood number cases, and the modulation of the effect of initial conditions were observed even at the same scaled, nondimensional times. Thus, it is suggested that additional scaling laws for both temporal and spatial scales be investigated, warranting capture of both spatial and temporal scales, and the ability to calculate ensemble-derived turbulence statistics via large-ensemble high speed simultaneous PLIF and PIV campaigns.

The value of high resolution time sequences and large ensembles of high resolution results which draw a statistical connection between the late time and the initial conditions, as well as describing the effect of Atwood number was demonstrated. However, it was desired to draw a direct connection between the times in a single sequence to understand the exact flow behaviors which result in the observed flow fields at late time. Therefore, the current work demonstrates the recent ability for spatio-temporally resolved measurements for shock-driven variable-density mixing, by exploiting the advances in diagnostics for simultaneous velocity and mixture fraction measurements for the first time in Richtmyer–Meshkov flow. This work enables future studies of turbulent mixing phenomena and modeling for applications in shock-driven hydrodynamics (such as shock- and blast-driven RMI and RTI in HED applications). Important experimental considerations are emphasized for these high-speed measurements, particularly related to the acquisition challenges, laser energy and flow characteristics. The quality of results was assessed and validated by comparing the results to previously published high-resolution, single-shot measurements on Richtmyer-Meshkov Instability. The high-speed vorticity fields enable tracking and temporal analysis of small scale vortical features that are essential to understand the molecular mixing behavior of such turbulent flows, and this vorticity is connected to the mixing in this flow observable for the first time with these simultaneous field diagnostics. These simultaneous diagnostics are essential to these flows, which are inherently dominated by small scale physics, as the same cannot be achieved using time-uncorrelated independent experiments (owing to randomness in small-scale structures) or simulations (owing to high spatio-temporal requirements and modeling constraints). Two commonly used models for initiation of deposited vorticity (SRZ98 [1] and WCB13 [2]) for computational studies were evaluated with this unique dataset, and it was shown that the WCB13 approach is capable of offsetting the typical assumptions (to a limited extent) via a prescribed interface jump velocity when the same is available via measurements.

Further, an illustration of the often-studied symmetric vortex merging[109] was demonstrated in a shock-driven variable-density flow for the first time, together with the induced effects on scalar mixing in unprecedented detail.

This work comprises many valuable contributions to the broad knowledge in the field. This thesis demonstrates the effects of Atwood number and the associated modulation of the impact of initial conditions for the Richtmyer–Meshkov Instability through large-ensemble statistics for the first time. This work evaluated several existing growth models with similar results to various prior experimental and computational investigations, experimentally confirmed utility of an interface scaling law [54, 96] with two Atwood numbers while maintaing other parameters constant for the first time. This work analyzed the differences caused by Atwood number despite this scaling and with the highest level of possible parametric similarity. The current work strengthened the argument for the existence of asymptotic trends in turbulent mixing flows and demonstrated their dependence on Atwood number. This work analyzed the validity of the Boussinesq approximation for modeling several quantities, and identified a marked difference in isotropization due to increased density contrast. Because of the experimental similarity maintained between the Atwood number cases, the current work can be used to evaluate and improve turbulence models such as the BHR model under changes in Atwood number and initial conditions.

This work visualizes the development of the interface via simultaneous PLIF and PIV in unprecedented temporal detail as well. This work provides the blueprint for future work utilizing this technique. The comparisons with vorticity deposition models in this work postures the community to initialize simulations in new ways, reducing the need for expensive shock capturing schemes. These measurements and analysis have equipped and postured the scientific community to continue to seek understanding of these types of flows through time-resolved measurements of both velocity and density with possible trajectories leading to comprehension of phenomena such as vortex accelerated vorticity

deposition and pursuit of vortex-dynamic models for these flows.

6.2 Future Work

While this work contributed much to the scientific community, it also brings to light exciting next steps in the study of turbulent mixing driven by instabilities. This is the first comprehensive Atwood number comparison utilizing large ensembles of results in Richtmyer–Meshkov Flows, so there is much that can be built on the foundation laid in this thesis. Further Atwood numbers can be examined, as well as the effect of Mach number at the current Atwood number (A =0.67). The current shock tube can also be used to adjust the distance between the interface and the end wall. This would be valuable in varying the initial condition before reshock to investigate its effect on the interface after transition to turbulence.

Simultaneous field temperature measurements, using the temperature-dependent emission spectra of a PIV tracer would be an improvement to the study of variable density flows where there is also a large temperature mismatch, such as the one induced by the shock in this flow. The refractive index mismatch can hamper laser diagnostics, which could be alleviated by a robust temperature correction based on field temperature data. Further diagnostic improvements would include tomographic PIV to capture out-of-plane gradients, and better understand the three-dimensionality of the flow, and the factors that affect this feature.

This work prompts future study in even greater depth and breadth, especially utilizing high speed diagnostics. Specifically, the current work should be used to aid in planning a future large-ensemble high speed simultaneous PLIF and PIV campaign to analyze temporally-resolved evolution of turbulence statistics from ensemble results, allowing unprecedented insight into the generation and transport of turbulence quantities such as mass flux, and the statistical correlation of actual mixing rate with certain vorti-

cal features. The visualization of this flow in this work can be used for comparison with simulations to evaluate capture of flow events in unprecedented detail. Detailed analysis on non-stationary physics such as the Vortex Accelerated Vorticity Deposition (VAVD) [114], vorticity-based stochastic modeling of mixing, etc. are made possible with these techniques, that were previously not amenable to experimental methods. This thesis sets the stage for new horizons in the study of turbulent mixing.

REFERENCES

[1] R. Samtaney, J. Ray, and N. J. Zabusky, "Baroclinic circulation generation on shock accelerated slow/fast gas interfaces," *Physics of fluids*, vol. 10, no. 5, pp. 1217–1230, 1998.

[2] C. Weber, A. Cook, and R. Bonazza, "Growth rate of a shocked mixing layer with known initial perturbations," *J. Fluid Mech.*, vol. 725, pp. 372–401, 2013.

[3] J. Kane, R. P. Drake, and B. A. Remington, "An evaluation of the Richtmyer–Meshkov instability in supernova remnant formation," *Astrophys. J.*, vol. 511, no. 1, p. 335, 1999.

[4] K. Kifonidis, T. Plewa, L. Scheck, H. Janka, and E. Müller, "Non-spherical core collapse supernovae-II. the late-time evolution of globally anisotropic neutrino-driven explosions and their implications for SN 1987 A," *Astronomy & Astrophysics*, vol. 453, no. 2, pp. 661–678, 2006.

[5] D. Arnett, "The role of mixing in astrophysics," *The Astrophysical Journal Supplement Series*, vol. 127, no. 2, p. 213, 2000.

[6] I. A. Waitz, F. E. Marble, and E. E. Zukoski, "Investigation of a contoured wall injector for hypervelocity mixing augmentation," *AIAA J.*, vol. 31, no. 6, pp. 1014–1021, 1993.

[7] Q. Yang, J. Chang, and W. Bao, "Richtmyer–Meshkov instability induced mixing enhancement in the scramjet combustor with a central strut," *Advances in Mechanical Engineering*, vol. 6, p. 614 189, 2014.

[8] F. E. Marble, G. J. Hendricks, and E. E. Zukoski, "Progress toward shock enhancement of supersonic combustion processes," in *Turbulent Reactive Flows*, Springer, 1989, pp. 932–950.

[9] R. D. Richtmyer, "Taylor instability in shock acceleration of compressible fluids," *Commun. Pure Appl. Maths*, vol. 13, no. 2, pp. 297–319, 1960.

[10] R. Lord, "Investigation of the character of the equilibrium of an incompressible heavy fluid of variable density," *Scientific papers*, pp. 200–207, 1900.

[11] G. Taylor, "The instability of liquid surfaces when accelerated in a direction perpendicular to their planes. I," vol. 201, no. 1065, pp. 192–196, 1950.

[12] G. Dimonte and M. Schneider, "Turbulent Richtmyer–Meshkov instability experiments with strong radiatively driven shocks," *Phys. Plasmas*, vol. 4, no. 12, pp. 4347–4357, 1997.

[13] G. Dimonte and M. Schneider, "Density ratio dependence of Rayleigh–Taylor mixing for sustained and impulsive acceleration histories," *Phys. Fluids*, vol. 12, no. 2, pp. 304–321, 2000.

[14] J. W. Jacobs, V. V. Krivets, V. Tsiklashvili, and O. A. Likhachev, "Experiments on the Richtmyer–Meshkov instability with an imposed, random initial perturbation," *Shock Waves*, vol. 23, no. 4, pp. 407–413, 2013.

[15] C. R. Weber, N. S. Haehn, J. G. Oakley, D. A. Rothamer, and R. Bonazza, "An experimental investigation of the turbulent mixing transition in the Richtmyer–Meshkov instability," *J. Fluid Mech.*, vol. 748, pp. 457–487, 2014.

[16] J. Prasad, A. Rasheed, S. Kumar, and B. Sturtevant, "The late-time development of the Richtmyer–Meshkov instability," *Phys. Fluids*, vol. 12, no. 8, pp. 2108–2115, 2000.

[17] P. E. Dimotakis, "The mixing transition in turbulent flows," *J. Fluid Mech.*, vol. 409, pp. 69–98, 2000.

[18] H. F. Robey, Y. e. Zhou, A. C. Buckingham, P. Keiter, B. A. Remington, and R. P. Drake, "The time scale for the transition to turbulence in a high Reynolds number, accelerated flow," *Phys. Plasmas*, vol. 10, no. 3, pp. 614–622, 2003.

[19] W. K. George and L. Davidson, "Role of initial conditions in establishing asymptotic flow behavior," *AIAA J.*, vol. 42, no. 3, pp. 438–446, 2004.

[20] W. K. George, "Is there an asymptotic effect of initial and upstream conditions on turbulence?" In *ASME 2008 Fluids Engineering Division Summer Meeting collocated with the Heat Transfer, Energy Sustainability, and 3rd Energy Nanotechnology Conferences*, American Society of Mechanical Engineers, 2008, pp. 647–672.

[21] A. Banerjee and M. J. Andrews, "3d simulations to investigate initial condition effects on the growth of Rayleigh–Taylor mixing," *Int. J. Heat Mass Transfer*, vol. 52, no. 17, pp. 3906–3917, 2009.

[22] S. Kuchibhatla and D. Ranjan, "Effect of initial conditions on Rayleigh–Taylor mixing: Modal interaction," *Phys. Scr.*, vol. 2013, no. T155, p. 014 057, 2013.

[23] J. W. Jacobs and J. M. Sheeley, "Experimental study of incompressible Richtmyer–Meshkov instability," *Phys. Fluids*, vol. 8, no. 2, pp. 405–415, 1996.

[24] C. E. Niederhaus and J. W. Jacobs, "Experimental study of the richtmyer–meshkov instability of incompressible fluids," *J. Fluid Mech.*, vol. 485, pp. 243–277, 2003.

[25] P. R. Chapman and J. W. Jacobs, "Experiments on the three-dimensional incompressible richtmyer-meshkov instability," *Physics of Fluids*, vol. 18, no. 7, p. 074 101, 2006.

[26] J. Kane, H. Robey, B. Remington, R. Drake, J Knauer, D. Ryutov, H Louis, R Teyssier, O Hurricane, D Arnett, *et al.*, "Interface imprinting by a rippled shock using an intense laser," *Physical Review E*, vol. 63, no. 5, p. 055 401, 2001.

[27] E. E. Meshkov, "Instability of the interface of two gases accelerated by a shock wave," *Fluid Dyn.*, vol. 4, no. 5, pp. 101–104, 1969.

[28] E. Meshkov, "Instability of a shock wave accelerated interface between two gases," *NASA Tech. Trans*, vol. 13, p. 74, 1970.

[29] M. Brouillette and B. Sturtevant, "Experiments on the Richtmyer–Meshkov instability: Single-scale perturbations on a continuous interface," *J. Fluid Mech.*, vol. 263, pp. 271–292, 1994.

[30] L. Houas and I. Chemouni, "Experimental investigation of Richtmyer–Meshkov instability in shock tube," *Phys. Fluids*, vol. 8, no. 2, pp. 614–627, 1996.

[31] M. Vetter and B. Sturtevant, "Experiments on the Richtmyer–Meshkov instability of an air/SF6 interface," *Shock Waves*, vol. 4, no. 5, pp. 247–252, 1995.

[32] R. H. Cohen, W. P. Dannevik, A. M. Dimits, D. E. Eliason, A. A. Mirin, Y. Zhou, D. H. Porter, and P. R. Woodward, "Three-dimensional simulation of a richtmyer–meshkov instability with a two-scale initial perturbation," *Physics of Fluids*, vol. 14, no. 10, pp. 3692–3709, 2002.

[33] D. J. Hill, C. Pantano, and D. I. Pullin, "Large-eddy simulation and multiscale modelling of a Richtmyer–Meshkov instability with reshock," *J. Fluid Mech.*, vol. 557, pp. 29–61, 2006.

[34] O. Schilling and M. Latini, "High-order WENO simulations of three-dimensional reshocked Richtmyer–Meshkov instability to late times: Dynamics, dependence on initial conditions, and comparisons to experimental data," *Math. Acta Sci.*, vol. 30, no. 2, pp. 595–620, 2010.

[35] F. Poggi, M.-H. Thorembey, and G. Rodriguez, "Velocity measurements in turbulent gaseous mixtures induced by richtmyer–meshkov instability," *Physics of Fluids*, vol. 10, no. 11, pp. 2698–2700, 1998.

[36] D. Ranjan, *Experimental investigation of the shock-induced distortion of a spherical gas inhomogeneity*. University of Wisconsin–Madison, 2007.

[37] T. Si, Z. Zhai, J. Yang, and X. Luo, "Experimental investigation of reshocked spherical gas interfaces," *Physics of Fluids*, vol. 24, no. 5, p. 054 101, 2012.

[38] J. H. Niederhaus, J. Greenough, J. Oakley, D Ranjan, M. Anderson, and R Bonazza, "A computational parameter study for the three-dimensional shock–bubble interaction," *Journal of Fluid Mechanics*, vol. 594, pp. 85–124, 2008.

[39] D. Ranjan, J. Oakley, and R. Bonazza, "Shock-bubble interactions," *Annu. Rev. Fluid Mech.*, vol. 43, pp. 117–140, 2011.

[40] D. Ranjan, J. H. Niederhaus, J. G. Oakley, M. H. Anderson, R. Bonazza, and J. A. Greenough, "Shock-bubble interactions: Features of divergent shock-refraction geometry observed in experiments and simulations," *Physics of Fluids*, vol. 20, no. 3, p. 036 101, 2008.

[41] L. Liu, Y. Liang, J. Ding, N. Liu, and X. Luo, "An elaborate experiment on the single-mode richtmyer–meshkov instability," *Journal of Fluid Mechanics*, vol. 853, 2018.

[42] X. Luo, Y. Liang, T. Si, and Z. Zhai, "Effects of non-periodic portions of interface on richtmyer–meshkov instability," *Journal of Fluid Mechanics*, vol. 861, pp. 309–327, 2019.

[43] Y. Liang, Z. Zhai, J. Ding, and X. Luo, "Richtmyer–meshkov instability on a quasi-single-mode interface," *Journal of Fluid Mechanics*, vol. 872, pp. 729–751, 2019.

[44] J. W. Jacobs, "Shock-induced mixing of a light-gas cylinder," *Journal of Fluid Mechanics*, vol. 234, pp. 629–649, 1992.

[45] K Prestridge, P. Rightley, P Vorobieff, R. Benjamin, and N. Kurnit, "Simultaneous density-field visualization and piv of a shock-accelerated gas curtain," *Experiments in fluids*, vol. 29, no. 4, pp. 339–346, 2000.

[46] B. J. Balakumar, G. C. Orlicz, C. D. Tomkins, and K. P. Prestridge, "Dependence of growth patterns and mixing width on initial conditions in Richtmyer–Meshkov unstable fluid layers," *Phys. Scr.*, vol. 2008, no. T132, p. 014 013, 2008.

[47] B. Motl, J. Oakley, D. Ranjan, C. Weber, M. Anderson, and R. Bonazza, "Experimental validation of a Richtmyer–Meshkov scaling law over large density ratio and shock strength ranges," *Phys. Fluids*, vol. 21, no. 12, p. 126 102, 2009.

[48] M. A. Jones and J. W. Jacobs, "A membraneless experiment for the study of Richtmyer–Meshkov instability of a shock-accelerated gas interface," *Phys. Fluids*, vol. 9, no. 10, pp. 3078–3085, 1997.

[49] B. D. Collins and J. W. Jacobs, "PLIF flow visualization and measurements of the Richtmyer–Meshkov instability of an air/SF6 interface," *J. Fluid Mech.*, vol. 464, pp. 113–136, 2002.

[50] J. Jacobs and V. Krivets, "Experiments on the late-time development of single-mode richtmyer–meshkov instability," *Physics of Fluids*, vol. 17, no. 3, p. 034 105, 2005.

[51] C. R. Weber, N. Haehn, J. Oakley, D. Rothamer, and R. Bonazza, "Turbulent mixing measurements in the Richtmyer–Meshkov instability," *Phys. Fluids*, vol. 24, no. 7, p. 074 105, 2012.

[52] O. Schilling, M. Latini, and W. S. Don, "Physics of reshock and mixing in single-mode Richtmyer–Meshkov instability," *Phys. Rev. E*, vol. 76, no. 2, p. 026 319, 2007.

[53] M. Latini, O. Schilling, and W. Don, "Effects of WENO flux reconstruction order and spatial resolution on reshocked two-dimensional Richtmyer–Meshkov instability," *J. Comput. Phys.*, vol. 221, no. 2, pp. 805–836, 2007.

[54] J. A. McFarland, J. A. Greenough, and D. Ranjan, "Computational parametric study of a Richtmyer–Meshkov instability for an inclined interface," *Phys. Rev. E*, vol. 84, no. 2, p. 026 303, 2011.

[55] R. V. Morgan, R. Aure, J. D. Stockero, J. A. Greenough, W. Cabot, O. A. Likhachev, and J. W. Jacobs, "On the late-time growth of the two-dimensional Richtmyer–Meshkov instability in shock tube experiments," *J. Fluid Mech.*, vol. 712, pp. 354–383, 2012.

[56] A. W. Cook and W. H. Cabot, "Hyperviscosity for shock-turbulence interactions," *J. Comput. Phys.*, vol. 203, no. 2, pp. 379–385, 2005.

[57] A. W. Cook, "Artificial fluid properties for large-eddy simulation of compressible turbulent mixing," *Phys. Fluids*, vol. 19, no. 5, p. 055 103, 2007.

[58] B. Thornber, D. Drikakis, D. L. Youngs, and R. J. R. Williams, "Growth of a Richtmyer–Meshkov turbulent layer after reshock," *Phys. Fluids*, vol. 23, no. 9, p. 095 107, 2011.

[59] ——, "Physics of the single-shocked and reshocked Richtmyer–Meshkov instability," *J. Turbul.*, vol. 13, no. 1, N10, 2012.

[60] J. A. McFarland, D. Reilly, W. Black, J. A. Greenough, and D. Ranjan, "Modal interactions between a large-wavelength inclined interface and small-wavelength multimode perturbations in a Richtmyer–Meshkov instability," *Phys. Rev. E*, vol. 92, no. 1, p. 013 023, 2015.

[61] M Lombardini, D. Hill, D. Pullin, and D. Meiron, "Atwood ratio dependence of richtmyer–meshkov flows under reshock conditions using large-eddy simulations," *Journal of fluid mechanics*, vol. 670, pp. 439–480, 2011.

[62] M. Mohaghar, J. Carter, B. Musci, D. Reilly, J. McFarland, and D. Ranjan, "Evaluation of turbulent mixing transition in a shock-driven variable-density flow," *J. Fluid Mech.*, vol. 831, pp. 779–825, 2017.

[63] M. Mohaghar, J. Carter, G. Pathikonda, and D. Ranjan, "The transition to turbulence in shock-driven mixing: Effects of mach number and initial conditions," *Journal of Fluid Mechanics*, vol. 871, pp. 595–635, 2019.

[64] M. Mohaghar, "Effects of initial conditions and mach number on turbulent mixing transition of shock-driven variable-density flow," PhD thesis, Georgia Institute of Technology, 2019.

[65] C. Long, V. Krivets, J. Greenough, and J. W. Jacobs, "Shock tube experiments and numerical simulation of the single-mode, three-dimensional richtmyer–meshkov instability," *Physics of Fluids*, vol. 21, no. 11, p. 114 104, 2009.

[66] J. Ding, J. Li, R. Sun, Z. Zhai, and X. Luo, "Convergent richtmyer–meshkov instability of a heavy gas layer with perturbed outer interface," *Journal of Fluid Mechanics*, vol. 878, pp. 277–291, 2019.

[67] G. C. Orlicz, B. J. Balakumar, C. D. Tomkins, and K. P. Prestridge, "A mach number study of the Richtmyer–Meshkov instability in a varicose, heavy-gas curtain," *Phys. Fluids*, vol. 21, no. 6, p. 064 102, 2009.

[68] B. J. Balakumar, G. C. Orlicz, J. R. Ristorcelli, S. Balasubramanian, K. P. Prestridge, and C. D. Tomkins, "Turbulent mixing in a Richtmyer–Meshkov fluid layer after reshock: Velocity and density statistics," *J. Fluid Mech.*, vol. 696, pp. 67–93, 2012.

[69] D. Besnard, F. H. Harlow, R. M. Rauenzahn, and C. Zemach, "Turbulence transport equations for variable-density turbulence and their relationship to two-field models," Los Alamos National Lab., lA-12303-MS, Tech. Rep., 1992.

[70] B. Brock, R. H. Haynes, B. S. Thurow, G. W. Lyons, and N. E. Murray, "An examination of mhz rate piv in a heated supersonic jet," in *52nd aerospace sciences meeting*, 2014, p. 1102.

[71] M. P. Wernet, "Temporally resolved piv for space–time correlations in both cold and hot jet flows," *Measurement Science and Technology*, vol. 18, no. 5, p. 1387, 2007.

[72] S. Beresh, S. Kearney, J. Wagner, D. Guildenbecher, J. Henfling, R. Spillers, B. Pruett, N. Jiang, M. Slipchenko, J. Mance, *et al.*, "Pulse-burst piv in a high-speed wind tunnel," *Measurement Science and Technology*, vol. 26, no. 9, p. 095 305, 2015.

[73] J. Wagner, S. J. Beresh, E. P. DeMauro, K. M. Casper, B. O. M. Pruett, and P. A. Farias, "Time-resolved piv in a shock tube using a pulse-burst laser.," Sandia National Lab.(SNL-NM), Albuquerque, NM (United States), Tech. Rep., 2015.

[74] J. B. Michael, P. Venkateswaran, J. D. Miller, M. N. Slipchenko, J. R. Gord, S. Roy, and T. R. Meyer, "100 khz thousand-frame burst-mode planar imaging in turbulent flames," *Optics letters*, vol. 39, no. 4, pp. 739–742, 2014.

[75] S. Roy, P. S. Hsu, N. Jiang, M. N. Slipchenko, and J. R. Gord, "100-khz-rate gas-phase thermometry using 100-ps pulses from a burst-mode laser," *Optics letters*, vol. 40, no. 21, pp. 5125–5128, 2015.

[76] J. D. Miller, J. B. Michael, M. N. Slipchenko, S. Roy, T. R. Meyer, and J. R. Gord, "Simultaneous high-speed planar imaging of mixture fraction and velocity using a burst-mode laser," *Applied Physics B*, vol. 113, no. 1, pp. 93–97, 2013.

[77] B. Thurow, N. Jiang, and W. Lempert, "Review of ultra-high repetition rate laser diagnostics for fluid dynamic measurements," *Measurement Science and Technology*, vol. 24, no. 1, p. 012 002, 2012.

[78] R. Samtaney and N. J. Zabusky, "Circulation deposition on shock-accelerated planar and curved density-stratified interfaces: Models and scaling laws," *Journal of Fluid Mechanics*, vol. 269, pp. 45–78, 1994.

[79] B. J. Balakumar, G. C. Orlicz, C. D. Tomkins, and K. P. Prestridge, "Simultaneous particle-image velocimetry–planar laser-induced fluorescence measurements of Richtmyer–Meshkov instability growth in a gas curtain with and without reshock," *Phys. Fluids*, vol. 20, no. 12, p. 124 103, 2008.

[80] J. A. Mcfarland, "Experimental and computational study of the inclined interface richtmyer-meshkov instability," PhD thesis, 2013.

[81] D. Reilly, "Experimental study of shock-driven, variable-density turbulence using a complex interface," in *Master's thesis, Georgia Institute of Technology*, 2015.

[82] D. Reilly, J. McFarland, M. Mohaghar, and D. Ranjan, "The effects of initial conditions and circulation deposition on the inclined-interface reshocked Richtmyer–Meshkov instability," *Exp. Fluids*, vol. 56, no. 8, pp. 1–16, 2015.

[83] P. Lavoie, G. Avallone, F. De Gregorio, G. Romano, and R. Antonia, "Spatial resolution of PIV for the measurement of turbulence," *Exp. Fluids*, vol. 43, no. 1, pp. 39–51, 2007.

[84] M. Stanislas and J. Monnier, "Practical aspects of image recording in particle image velocimetry," *Meas. Sci. Tech.*, vol. 8, no. 12, p. 1417, 1997.

[85] M. N. Slipchenko, J. D. Miller, S. Roy, J. R. Gord, S. A. Danczyk, and T. R. Meyer, "Quasi-continuous burst-mode laser for high-speed planar imaging," *Optics Letters*, vol. 37, no. 8, pp. 1346–1348, 2012.

[86] M. N. Slipchenko, J. D. Miller, S. Roy, J. R. Gord, and T. R. Meyer, "All-diode-pumped quasi-continuous burst-mode laser for extended high-speed planar imaging," *Optics express*, vol. 21, no. 1, pp. 681–689, 2013.

[87] M. N. Slipchenko, J. D. Miller, S. Roy, T. R. Meyer, J. G. Mance, and J. R. Gord, "100 khz, 100 ms, 400 j burst-mode laser with dual-wavelength diode-pumped amplifiers," *Optics Letters*, vol. 39, no. 16, pp. 4735–4738, 2014.

[88] C. Weber, "Turbulent Mixing Measurements in the Richtmyer-Meshkov Instability," PhD thesis, The University of Wisconsin-Madison, 2012.

[89] J. J. Charonko and P. P. Vlachos, "Estimation of uncertainty bounds for individual particle image velocimetry measurements from cross-correlation peak ratio," *Meas. Sci. Tech.*, vol. 24, no. 6, p. 065 301, 2013.

[90] Z. Xue, J. J. Charonko, and P. P. Vlachos, "Particle image velocimetry correlation signal-to-noise ratio metrics and measurement uncertainty quantification," *Meas. Sci. Tech.*, vol. 25, no. 11, p. 115 301, 2014.

[91] J. S. Bendat and A. G. Piersol, *Random data: analysis and measurement procedures*. John Wiley & Sons, 2011.

[92] S. W. Haan, "Weakly nonlinear hydrodynamic instabilities in inertial fusion," *Physics of Fluids B: Plasma Physics*, vol. 3, no. 8, pp. 2349–2355, 1991.

[93] Q. Zhang and S.-I. Sohn, "Nonlinear theory of unstable fluid mixing driven by shock wave," *Physics of Fluids*, vol. 9, no. 4, pp. 1106–1124, 1997.

[94] O Sadot, L Erez, U Alon, D. Oron, L. Levin, G Erez, G Ben-Dor, and D Shvarts, "Study of nonlinear evolution of single-mode and two-bubble interaction under richtmyer-meshkov instability," *Physical review letters*, vol. 80, no. 8, p. 1654, 1998.

[95] K. O. Mikaelian, "Turbulent mixing generated by Rayleigh–Taylor and Richtmyer–Meshkov instabilities," *Phys. D*, vol. 36, no. 3, pp. 343–357, 1989.

[96] J. McFarland, J. Greenough, and D. Ranjan, "Simulations and analysis of the reshocked inclined interface Richtmyer–Meshkov instability for linear and nonlinear interface perturbations," *Trans. ASME: J. Fluids Engng*, vol. 136, no. 7, p. 071 203, 2014.

[97] B. Thornber and Y. Zhou, "Energy transfer in the richtmyer-meshkov instability," *Physical Review E*, vol. 86, no. 5, p. 056 302, 2012.

[98] Y. Zhou, W. H. Cabot, and B. Thornber, "Asymptotic behavior of the mixed mass in Rayleigh–Taylor and Richtmyer–Meshkov instability induced flows," *Phys. Plasmas*, vol. 23, no. 5, p. 052 712, 2016.

[99] V. K. Tritschler, B. J. Olson, S. K. Lele, S. Hickel, X. Y. Hu, and N. A. Adams, "On the Richtmyer–Meshkov instability evolving from a deterministic multimode planar interface," *J. Fluid Mech.*, vol. 755, pp. 429–462, 2014.

[100] S. B. Pope, *Turbulent flows*. Cambridge University Press, 2000.

[101] J. D. Schwarzkopf, D. Livescu, J. R. Baltzer, R. A. Gore, and J. R. Ristorcelli, "A two-length scale turbulence model for single-phase multi-fluid mixing," *Flow Turbul. Combust.*, vol. 96, no. 1, pp. 1–43, 2016.

[102] D. Livescu and J. R. Ristorcelli, "Variable-density mixing in buoyancy-driven turbulence," *J. Fluid Mech.*, vol. 605, pp. 145–180, 2008.

[103] C. D. Tomkins, B. J. Balakumar, G. Orlicz, K. P. Prestridge, and J. R. Ristorcelli, "Evolution of the density self-correlation in developing Richtmyer–Meshkov turbulence," *J. Fluid Mech.*, vol. 735, pp. 288–306, 2013.

[104] P. E. Dimotakis, "Turbulent mixing," *Annu. Rev. Fluid Mech.*, vol. 37, pp. 329–356, 2005.

[105] J. Picone and J. Boris, "Vorticity generation by shock propagation through bubbles in a gas," *Journal of Fluid Mechanics*, vol. 189, pp. 23–51, 1988.

[106] L. F. Henderson, P. Colella, and E. G. Puckett, "On the refraction of shock waves at a slow–fast gas interface," *Journal of Fluid Mechanics*, vol. 224, pp. 1–27, 1991.

[107] J Ray and L Jameson, "Estimation of shock induced vorticity on irregular gaseous interfaces: A wavelet-based approach," *Shock Waves*, vol. 14, no. 3, pp. 147–160, 2005.

[108] R. Adrian, K. Christensen, and Z.-C. Liu, "Analysis and interpretation of instantaneous turbulent velocity fields," *Experiments in fluids*, vol. 29, no. 3, pp. 275–290, 2000.

[109] M. Melander, N. Zabusky, and J. McWilliams, "Symmetric vortex merger in two dimensions: Causes and conditions," *Journal of Fluid Mechanics*, vol. 195, pp. 303–340, 1988.

[110] P. Meunier, U. Ehrenstein, T. Leweke, and M. Rossi, "A merging criterion for two-dimensional co-rotating vortices," *Physics of Fluids*, vol. 14, no. 8, pp. 2757–2766, 2002.

[111] C Cerretelli and C. Williamson, "The physical mechanism for vortex merging," *Journal of Fluid Mechanics*, vol. 475, pp. 41–77, 2003.

[112] D. G. Dritschel, "A general theory for two-dimensional vortex interactions," *Journal of Fluid Mechanics*, vol. 293, pp. 269–303, 1995.

[113] K. Fine, C. Driscoll, J. Malmberg, and T. Mitchell, "Measurements of symmetric vortex merger," *Physical review letters*, vol. 67, no. 5, p. 588, 1991.

[114] N. J. Zabusky, "Vortex paradigm for accelerated inhomogeneous flows: Visiometrics for the Rayleigh-Taylor and Richtmyer-Meshkov environments," *Annu. Rev. Fluid Mech.*, vol. 31, no. 1, pp. 495–536, 1999.

[115] M. Lombardini, D. I. Pullin, and D. I. Meiron, "Transition to turbulence in shock-driven mixing: A mach number study," *J. Fluid Mech.*, vol. 690, pp. 203–226, 2012.

VITA

John Carter was born in Houston, Texas and raised in Knoxville, Tennessee. John enjoyed Math, Chemistry, and Physics in high school along with orchestra and baseball. John pursued a developing interest in mechanical engineering at Tennessee Technological University in Cookvegas, Tennessee, where he gained further skills in engineering, leadership, service, and ethics as a member of the Baja SAE team and President of the Tennessee Tech chapter of the Pi Tau Sigma Mechanical Engineering Honor Society, and as a member of several other Math and Engineering Societies.

John tutored math at Pellissippi State Community College while in high school, continued tutoring and leading recitations for Calculus at Tennessee Tech. John also completed internships at Altec Industries and Contour Glass. These experiences have balanced John's academic endeavors with increased perspective and application of engineering principles. John decided to take graduate courses during his undergraduate studies. Out of an interest in fluid dynamics, John soon developed an Honors Directed Study performing fluids simulations guided by Professor Jie Cui.

Realizing a desire for more depth of understanding to solve engineering problems and an interest in teaching, John decided to pursue a PhD in Mechanical Engineering, in the area of Fluid Mechanics. This led John to Georgia Institute of Technology to work on the shock tube project in STAM lab under Prof. Devesh Ranjan. During this time John primarily studied the shock-driven instability experimentally, implementing state-of-the-art diagnostics. John was also fortunate to intern at Los Alamos National Laboratory to investigate the instability through simulations using turbulence models developed there. The thing John values most from graduate work is the opportunity to exercise self reliance and resourcefulness to learn completely new things necessary to solve challenges faced.